

EXPERIMENTAL DETERMINATION OF THE DRY OXIDATION
BEHAVIOR OF A COMPOSITIONAL RANGE OF
URANIUM-THORIUM MIXED-OXIDE PELLET FRAGMENTS

By

LISA ARGO

A THESIS PRESENTED TO THE GRADUATE SCHOOL
OF THE UNIVERSITY OF FLORIDA IN PARTIAL FULFILLMENT
OF THE REQUIREMENTS FOR THE DEGREE OF
MASTER OF SCIENCE

UNIVERSITY OF FLORIDA

2003

Copyright 2003

by

Lisa Argo

ACKNOWLEDGMENTS

This work would not have been completed without the support of many. More than anyone else, I thank my advisors (Ronald Baney and James Tulenko) for their wisdom, patience, understanding, and occasional cracking whip. I would like to acknowledge the contribution of Paul Demkowicz for his expertise and meticulous editing; and Noriko Shibuya for her technical support, as we investigated the ins and outs of many synthesis methods. I thank my sister, Irene, for the late night pep talks and advice. I thank my husband, Paul, for pushing me back into and out of school.

This work was funded through a grant from the Nuclear Engineering Research Initiative (NERI) project #99-0153 Advanced Proliferation Resistant, Lower Cost, Uranium-Thorium Dioxide Fuels for Light Water Reactors.

TABLE OF CONTENTS

	<u>page</u>
ACKNOWLEDGMENTS.....	iii
TABLE OF CONTENTS.....	iv
LIST OF TABLES.....	vi
LIST OF FIGURES.....	viii
ABSTRACT.....	xi
CHAPTER	
1 INTRODUCTION.....	1
2 REVIEW OF LITERATURE.....	5
Current Status of UO ₂ and ThO ₂ Research.....	5
Uranium Dioxide.....	5
Thorium Oxide.....	9
Uranium-Thorium Mixed Oxide.....	11
Background of Synthesis Methods.....	14
Kinetic Analysis.....	16
3 MATERIALS AND METHODS.....	20
Material Synthesis.....	20
Oxalate Co-Precipitation.....	20
Ammonium Hydroxide Co-Precipitation.....	26
Co-Milled Mixed Oxides.....	27
Characterization.....	32
X-ray Diffraction (XRD).....	32
Elemental Analysis.....	35
Particle Morphology.....	36
Pellet Density.....	37
Dry Oxidation.....	38
Thermogravimetric Analyzer.....	38
Kinetic Analysis.....	39
4 RESULTS AND DISCUSSION.....	43
Material Synthesis.....	43
Thermogravimetry.....	45

Kinetic Analysis	54
Mixed Oxide ($U_{0.236}Th_{0.764}O_2$).....	55
Mixed Oxide ($U_{0.368}Th_{0.632}O_2$).....	61
Mixed Oxide ($U_{0.50}Th_{0.50}O_2$).....	66
Pure Uranium Dioxide (UO_2).....	71
5 SUMMARY AND CONCLUSIONS	74
APPENDIX	
A ACTIVATION ENERGIES	77
B X-RAY DIFFRACTION PATTERNS.....	80
C SECONDARY ELECTRON IMAGES OF UNIRRADIATED PELLETS	91
REFERENCES	93
BIOGRAPHICAL SKETCH.....	97

LIST OF TABLES

<u>Table</u>	<u>page</u>
2-1. Defect formation energies for UO_2	6
2-2. Oxidation reactions of UO_{2+x}	7
2-3. Material properties of ThO_2 and UO_2	9
2-4. Cation and anion formation and migration energies in ThO_2	10
2-5. Composition dependence on oxygen partial pressure for UO_{2+x} and $(\text{U,Th})\text{O}_{2+x}$	13
2-6. Rate laws for a simple process $\text{A} \rightarrow \text{P}$	18
3-1. Evolution of oxalate-synthesized $(\text{U,Th})\text{O}_2$	23
3-2. 2×2 factorial for 20% UO_2 -80% ThO_2 blended oxide.....	30
3-3. Co-milled $\text{U}_{0.2}\text{Th}_{0.8}\text{O}_2$ pressing conditions 2×2 factorial results.....	30
3-4. Pellet manufacture conditions	31
3-5. Solid state theoretical reaction models.....	41
4-1. Calculated $(\text{U,Th})\text{O}_2$ oxidized lattice parameters by three methods	43
4-2. ICP-AES and LECO carbon analysis results and calculated metal valence.....	45
4-3. Rate coefficients of isothermal $(\text{U}_{0.236}\text{Th}_{0.764})\text{O}_2$ agreement to diffusion models	56
4-4. Kinetic results for nonisothermal $(\text{U}_{0.236}\text{Th}_{0.764})\text{O}_2$ agreement to diffusion models.....	56
4-5. Rate coefficient of isothermal $(\text{U}_{0.368}\text{Th}_{0.632})\text{O}_2$ agreement to 3D diffusion model.....	63
4-6. Kinetic results for nonisothermal $(\text{U}_{0.368}\text{Th}_{0.632})\text{O}_2$ agreement to 3D diffusion model.....	63
4-7. Rate coefficient of isothermal $(\text{U}_{0.50}\text{Th}_{0.50})\text{O}_2$ agreement to 3D diffusion model.....	68
4-8. Kinetic results for nonisothermal $(\text{U}_{0.50}\text{Th}_{0.50})\text{O}_2$ in 3D diffusion and Avrami-Erofe'ev ...	68
5-1. Estimated E and A by model-free and model-fit techniques of $(\text{U,Th})\text{O}_2$ and UO_2	76
A-1. Published estimates of $\text{U}_3\text{O}_7/\text{U}_4\text{O}_9$ activation energy of formation	77

A-2. Published estimates of U_3O_8 formation on UO_2 activation energies.....	77
A-3. Published estimates of UO_2 cation and anion diffusion activation energies.....	78
A-4. Published estimates of ThO_2 cation and anion diffusion activation energies.....	78
A-5. Published estimates of diffusion in $(U,Th)O_2$ activation energies.....	79
A-6. Kinetic parameters of mixed urania-thoria oxides.....	79
B-1. $U_{0.368}Th_{0.632}O_{2+x}$ isothermal 400°C air oxidized compared to JCPDS standards.....	80
B-2. XRD peak intensities for 450°C isotherm of co-milled 23.6% UO_2 fragments.....	81
B-3. XRD peak intensities for 500°C isotherm of co-milled 23.6% UO_2 fragments.....	82
B-4. XRD peak intensities for 550°C isotherm of co-milled 23.6% UO_2 fragments.....	83
B-5. XRD peak intensities for 400°C isotherm of co-milled 36.8% UO_2 fragments.....	84
B-6. XRD peak intensities for 450°C isotherm of co-milled 36.8% UO_2 fragments.....	85
B-7. XRD peak intensities for 500°C isotherm of co-milled 36.8% UO_2 fragments.....	86
B-8. XRD peak intensities for 375°C isotherm of co-milled 50.0% UO_2 fragments.....	87
B-9. XRD peak intensities for 400°C isotherm of co-milled 50.0% UO_2 fragments.....	88
B-10. XRD peak intensities for 425°C isotherm of co-milled 50.0% UO_2 fragments.....	89
B-11. XRD peak intensities for 450°C isotherm of co-milled 50.0% UO_2 fragments.....	90

LIST OF FIGURES

<u>Figure</u>	<u>page</u>
3-1. Oxalate path co-precipitation.....	21
3-2. Optical micrograph of nominal 20% UO ₂ calcined oxalate-synthesized powder	22
3-3. X-Ray Diffraction evolution of U _{0.05} Th _{0.95} O ₂ oxalate synthesized powder	24
3-4. Vulcan Muffle furnace used for drying, decomposition, and calcination	25
3-5. Lindberg high temperature tube furnace	25
3-6. Ammonium hydroxide path co-precipitation.....	26
3-7. Ammonium hydroxide synthesized (U _{0.2} Th _{0.8})O _{2+x} before (l) and after (r) calcinations.....	27
3-8. Optical micrographs of Alfa Aesar UO ₂ (l) and ThO ₂ (r)	28
3-9. 8000M SPEX Certiprep Mixer/Mill (l) and zirconia mill jar (r)	29
3-10. Pellets prepared using 20% U powder synthesized by the oxalate technique	31
3-11. Optical micrographs of nominal U _{0.2} Th _{0.8} O _{2+x}	37
3-12. TA Instruments TGA 2050 thermogravimetric analyzer.....	38
4-1. Lattice parameter evolution with respect to UO ₂ content.....	44
4-2. Nonisothermal (U _{0.236} Th _{0.764})O ₂ oxidation TGA data at heating rates of 1, 3, and 5°C/min. 47	47
4-3. Nonisothermal (U _{0.368} Th _{0.632})O ₂ oxidation TGA data at heating rates of 1, 3, and 5°C/min. 48	48
4-4. Nonisothermal (U _{0.500} Th _{0.500})O ₂ oxidation TGA data at heating rates of 1 and 5°C/min.	48
4-5. Nonisothermal UO ₂ oxidation TGA data at heating rate of 3°C/min.....	49
4-6. Isothermal oxidation TGA data for (U _{0.236} Th _{0.764})O ₂ fragments (90 – 250 μm)	50
4-7. Isothermal oxidation TGA data for (U _{0.368} Th _{0.632})O ₂ fragments (90 – 250 μm)	50
4-8. Isothermal oxidation TGA data for (U _{0.500} Th _{0.500})O ₂ fragments (90 – 250 μm)	51
4-9. Isothermal oxidation TGA data for UO ₂ fragments (90 – 250 μm).....	51

4-10. Mean uranium valence for isothermally oxidized $(U_yTh_{1-y})O_2$ and UO_2	54
4-11. Isotherm at 450°C of $(U_{0.236}Th_{0.764})O_2$ oxidation fit to 2D and 3D Diffusion models.....	57
4-12. Isotherm at 500°C of $(U_{0.236}Th_{0.764})O_2$ oxidation fit to 2D and 3D Diffusion models.....	57
4-13. Isotherm at 550°C of $(U_{0.236}Th_{0.764})O_2$ oxidation fit to 2D and 3D Diffusion models.....	58
4-14. Arrhenius plot of $(U_{0.236}Th_{0.764})O_2$ isotherms fit to 3D Diffusion models	58
4-15. Nonisotherm at 1°C/min $(U_{0.236}Th_{0.764})O_2$ Arrhenius plot fit to 2D and 3D diffusion	59
4-16. Nonisotherm at 3°C/min $(U_{0.236}Th_{0.764})O_2$ Arrhenius plot fit to 2D and 3D diffusion	59
4-17. Nonisotherm at 5°C/min $(U_{0.236}Th_{0.764})O_2$ Arrhenius plot fit to 2D and 3D diffusion	60
4-18. Model free $(U_{0.236}Th_{0.764})O_2$ isotherms plotted at $\alpha = 0.4, 0.5, 0.6$	60
4-19. Isotherm at 450°C for $(U_{0.368}Th_{0.632})O_2$ oxidation fit to 3D Diffusion	63
4-20. Isotherm at 475°C for $(U_{0.368}Th_{0.632})O_2$ oxidation fit to 3D Diffusion	64
4-21. Isotherm at 500°C for $(U_{0.368}Th_{0.632})O_2$ oxidation fit to 3D Diffusion	64
4-22. Arrhenius plot of $(U_{0.368}Th_{0.632})O_2$ isotherms fit to 3D Diffusion	65
4-23. Nonisotherms at 1, 3, and 5°C/min $(U_{0.368}Th_{0.632})O_2$ Arrhenius plot fit	65
4-24. Model free $(U_{0.368}Th_{0.632})O_2$ isotherms plotted at $\alpha = 0.4, 0.5, 0.6$	66
4-25. Isotherm at 375°C for $(U_{0.50}Th_{0.50})O_2$ oxidation in 3D Diffusion and Avrami-Erofe'ev.....	68
4-26. Isotherm at 400°C for $(U_{0.50}Th_{0.50})O_2$ oxidation in 3D Diffusion and Avrami-Erofe'ev.....	69
4-27. Isotherm at 425°C for $(U_{0.50}Th_{0.50})O_2$ oxidation in 3D Diffusion and Avrami-Erofe'ev.....	69
4-28. Isotherm at 450°C for $(U_{0.50}Th_{0.50})O_2$ oxidation in 3D Diffusion and Avrami-Erofe'ev.....	70
4-29. Arrhenius plot of $(U_{0.500}Th_{0.500})O_2$ isotherms in 3D Diffusion reaction model.....	70
4-30. Nonisotherms at 1 and 5°C/min $(U_{0.500}Th_{0.500})O_2$ Arrhenius plot	71
4-31. Model free $(U_{0.500}Th_{0.500})O_2$ isotherms plotted at $\alpha = 0.4, 0.5, 0.6$	71
4-32. Model free UO_2 isotherms plotted at $\alpha = 0.4, 0.5, 0.6$	73
B-1. XRD pattern for 450°C isotherm of co-milled 23.6% UO_2 fragments.....	81
B-2. XRD pattern for 500°C isotherm of co-milled 23.6% UO_2 fragments.....	82
B-3. XRD pattern for 550°C isotherm of co-milled 23.6% UO_2 fragments.....	83

B-4. XRD pattern for 400°C isotherm of co-milled 36.8% UO ₂ fragments	84
B-5. XRD pattern for 450°C isotherm of co-milled 36.8% UO ₂ fragments	85
B-6. XRD pattern for 500°C isotherm of co-milled 36.8% UO ₂ fragments	86
B-7. XRD pattern for 375°C isotherm of co-milled 50.0% UO ₂ fragments	87
B-8. XRD pattern for 400°C isotherm of co-milled 50.0% UO ₂ fragments	88
B-9. XRD pattern for 425°C isotherm of co-milled 50.0% UO ₂ fragments	89
B-10. XRD pattern for 450°C isotherm of co-milled 50.0% UO ₂ fragments	90
C-1. Unpolished U _{0.05} Th _{0.95} O _{2+x} pellet surface. Scale bar is 21 microns	91
C-2. Unpolished U _{0.05} Th _{0.95} O _{2+x} pellet surface. Scale bar is 20 microns	91
C-3. Broken surface of U _{0.2} Th _{0.8} O _{2+x} pellet	92

Abstract of Thesis Presented to the Graduate School
of the University of Florida in Partial Fulfillment of the
Requirements for the Degree of Master of Science

EXPERIMENTAL DETERMINATION OF THE DRY OXIDATION BEHAVIOR OF A
COMPOSITIONAL RANGE OF URANIUM-THORIUM MIXED-OXIDE PELLET
FRAGMENTS

By

Lisa Argo

December 2003

Chair: Ronald H. Baney
Major Department: Materials Science and Engineering

Oxidation of $(U_yTh_{1-y})O_2$ ($y = 0.236, 0.368, 0.500$) solid solutions was investigated using thermal gravimetric analysis and compared with UO_2 . The UO_2 and ThO_2 powders were ground, pressed into pellets, and sintered at $1650^\circ C$ in a reducing atmosphere. Gravimetric oxidation data for all samples, including UO_2 , exhibited single-step behavior. This was interpreted as the effect of the low surface-to-volume ratio of the fragments used (specific surface areas were 0.01 to 0.02 m^2/g) on the relative contributions of surface and bulk oxidation reactions, with bulk reactions dominating in this case compared to powders with higher surface area. Model-fitting kinetic analysis suggested diffusion ($y = 0.236, 0.368$) and possible nucleation and growth ($y = 0.500$) as possible mechanisms. Activation energy, E , for isothermal oxidation calculated by model-fitting increased with uranium content, 62.7 ± 17.9 and 171 ± 8 kJ/mol for $y = 0.236$ and 0.368 , respectively. X-ray diffraction patterns and uranium valence calculations do confirm that the ultimate oxidation is inhibited in the $(U,Th)O_2$ compared to UO_2 . Lattice structure remained cubic fluorite and did not undergo any phase transformation. Cation valencies indicated that

uranium does not proceed to its maximum oxidation state. The absence of quantitative particle and grain size data restricted the models in fully describing system complexity.

CHAPTER 1 INTRODUCTION

The objective of this project was to determine the long-term stability of ThO₂/UO₂ high level waste. Radionuclide leaching from spent UO₂ fuel is a major long-term storage concern for radiological materials. Mixed oxide (U,Th)O₂ fuels were considered an alternative because of the natural abundance of ThO₂, nonproliferation benefits, and potentially improved long-term spent-fuel storage capability. Oxidation behavior of (U,Th)O₂ solid solutions was measured as a function of the oxide composition in order to determine the relative advantage these materials possess over conventional UO₂.

Uranium dioxide oxidizes to a multitude of naturally occurring off-stoichiometric phases, (i.e., U₃O₇, U₄O₉, and U₃O₈). These phase changes induce pellet cracking (due to a 36% volume increase associated with the UO₂ → U₃O₈ transformation) and generally facilitate radionuclide release from the crystal lattice. Additionally, the higher oxidation states, U(V) and U(VI), form water-soluble species. Release of hazardous radionuclides from the spent-fuel into the surrounding environment, therefore, may occur through surface oxidation or catastrophic fracture during long-term storage. Since the life expectancy of uranium and thorium based high-level radioactive waste greatly exceeds any reasonable length of time to obtain experimental data, predictions of waste behavior rely upon accelerated tests and/or models based on an understanding of system behavior. Half-lives reported for uranium-238, -235, and thorium-232 are 4.46×10⁹ years, 7.04×10⁸ years, and 1.4×10¹⁰ years, respectively [Win03].

For instance, after gamma irradiation of CANDU polycrystalline UO₂ pellets in oxygen-rich/-free and moisture-rich/-free atmospheres, Sunder and Miller [Sun96] observed U(VI) by x-ray photoelectron spectroscopy (XPS) and multiple uranium oxide phases (UO₂, U₃O₇, U₃O₈,

U_8O_{19} , UO_3 , $U_{16}O_{37}$, etc.) by x-ray diffraction (XRD). Equivalent to gamma fields associated with 10- to 20-year-old used CANDU fuel [Sun96], irradiated pellets did not reach temperatures in excess of 150°C during Sunder and Miller's 2-day experiments. Uranium oxidation thus was restricted to surface crystalline growth. Catastrophic pellet fracture was not observed. Serrano et al. [Ser01] evaluated oxidized LWR UO_2 spent-fuel pieces in wet leaching experiments. Initial uranium fractional release was clearly related to oxidation level (starting O/M) of the fuel. Fission products identified in the leachate solution were plutonium-239, molybdenum-98, cesium-137, strontium-90, and technetium-99, where all but Pu-239 had release rates greater than for uranium. Serrano et al. [Ser01] attributed the increased fractional release rates to mobility along grain boundaries; and higher solubility of some fission products (like Tc or Cs). Shoemith [Sho00] identified unoxidized UO_2 as a "slow dissolving semiconducting oxide" with the major rate-controlling process as surface ionic species formation by surface charge transfer or alteration. Most (> 90%) fission products and actinides generated in-reactor, in fact, are retained in the UO_2 fuel matrix and expected to be released as the fuel degrades in storage [Sho00]. The sensitivity of UO_2 solubility when oxidized, therefore, makes fuel dissolution and radionuclide release dependent on repository redox conditions (i.e., oxidant supply) [Sho00].

Currently, various waste forms and packages encapsulate, stabilize, shield, and otherwise prevent or minimize high-level radioactive waste release while in storage at geologic repositories or interim sites. Two waste-form systems, borosilicate glass and Synroc, are currently used; although glass is still the preferred method for civil high-level radioactive waste. Both systems immobilize radioactive actinides within a material matrix. The liquid properties of glass permit the glass matrix to accommodate impurities nearly indiscriminately. Synroc, which is in developmental stages in the U.S. for military waste and surplus military plutonium storage, comprises titanate minerals (such as titanium dioxide, hollandite, zirconolite, and perovskite). Synroc, like vitrified glass, is globally recognized for its chemical durability and resistance to leaching at high temperatures.

In the same vein as glass vitrification and Synroc, mixed (U,Th)O₂ oxide solid solutions are pursued in this study as a material “barrier” specifically to uranium release. Thorium oxide, like the actinide oxides used for nuclear-reactor fuels, has a fluorite-type cubic lattice structure. Cations are arranged in a face-centered cubic close-packing sublattice. Anions occupy all tetrahedral interstitial positions, forming a simple cubic sublattice, with cations occupying one half the interstitial sites, and the remainder are vacant. Large octahedral interstitial holes remain where interstitial ions can be introduced to form a hyper-stoichiometric oxide. Diffusion characteristics of the fluorite structure indicate that anionic mobility (diffusion) is greater than cationic and ionic self-diffusion, because both anions and cations are sensitive to deviations from stoichiometry [And83]. Deviations from ThO₂ stoichiometry, however, are hindered. Unlike UO₂, thorium in ThO₂ is present in its maximum stable oxidation state, Th(IV), and cannot both accommodate excess anions and maintain charge neutrality. In fact, ThO₂ oxidation is largely independent of oxygen partial pressure [And76, And79, Haw68]. Additionally, thorium oxide is structurally and atomically similar to uranium oxide, unlike borosilicate glass and titanate minerals.

The stability and physical properties of the thorium oxide matrix present an alternative to pure UO₂ fuel in-reactor and may potentially replace other waste-form systems in minimizing radionuclide release in storage. Because ThO₂ is in its maximum oxidation state, thorium oxide is stronger and more durable than UO₂ in various ways. Solubility of ThO₂ over a wide range of aqueous solutions is extremely low as compared to UO₂ under reducing conditions [Tay96]. The ThO₂ (like UO₂) is not susceptible to radiation-induced phase transformation to an amorphous state [Tay96]. Grain growth, a major cause of fission product release and governed by cation diffusion, is expected to be similar or lower than UO₂. Since thorium oxide is a better thermal conductor, with a higher melting point and slower cation diffusion [And83, Tay96], it is expected to run cooler and undergo less grain growth for a given power rating and fuel geometry [Tay96].

Once a waste-form system has been used, the spent-fuel is further contained and packaged in systems (such as the use of lead canisters and other shielding or absorbent materials immediately surrounding an individual waste container). Despite the development of long-lived nuclear waste containers, the final barrier to radionuclide release is probably the waste-form system. Wet and dry waste vault/repository conditions are expected. For instance, according to the Nuclear Waste Management Organization, Canada initially stores spent nuclear fuel in water-filled pools called Irradiated Fuel Bays; and 7 to 10 years later transfers it to dry storage facilities. Assessing overall repository performance therefore demands an understanding of potential fuel degradation in wet and dry conditions.

The scope of this research consists of the manufacture and dry oxidative behavior of urania-thoria oxide solid solutions under accelerated dry-storage conditions as compared with pure UO_2 . Kinetic analysis is used to assess mixed $(\text{U,Th})\text{O}_2$ oxide behavior versus UO_2 . Various processing methods were considered, and a significant portion of this study was dedicated to evaluating and selecting a synthesis technique that would yield a homogenous product. Our study did not attempt to assess the in-reactor performance of urania-thoria fuels.

CHAPTER 2 REVIEW OF LITERATURE

Current Status of UO₂ and ThO₂ Research

Uranium Dioxide

Natural uranium is primarily composed of two isotopes (U-238 and the fissionable U-235). The fissionable isotope characterizes the economical value of nuclear fuel. The Oakridge National Laboratory Review website [Gab93] reported that nuclear fusion generates approximately 2×10^9 kWh/ton and coal combustion 6150 kWh/ton. From a mass to power-generated standpoint, uranium is undoubtedly superior. In generating this power, however, the radioactive and toxic byproducts generated dictate a complex waste system to prevent harm to the surrounding environment. The final waste form, after mechanical barriers have degraded, will ultimately be a material system that must immobilize mobile species, such as uranium.

Defect structure. Uranium dioxide has a cubic fluorite-type lattice structure, like other actinide oxides such as ThO₂ and PuO₂. In this crystal structure, diffusion characteristics favor anion diffusivity more than cation diffusivity. Point defects considered for diffusion in fluorite-cubic oxides are the oxygen Frenkel pair, cation Frenkel pair, and Schottky trio. Written in Kroger-Vink notation, defect-formation energies for stoichiometric UO₂ are shown in Table 2-1 suggesting that the most dominant defect is the oxygen Frenkel pair [And83].

Ando and Oishi [And83] reported that stoichiometric UO₂ and ThO₂ showed similar diffusion characteristics with activation energies ranging between 200 and 275 kJ/mol, which they interpreted to be intrinsic diffusion. The similarity in stoichiometric UO₂ and ThO₂ would further support that anion diffusivity is closely tied to the simple cubic anion sublattice, almost

regardless of cation species. Uranium self-diffusion in stoichiometric UO_2 , in turn, is closely related to the face-centered cubic cation sublattice.

Table 2-1. Defect formation energies for UO_2

Defect	Kroger-Vink Notation	Energy (kJ/mol)
Oxygen Frenkel pair	$[V_{\text{O}}^{\bullet\bullet}][O_{\text{i}}^{\prime\prime}]$	482
Uranium Frenkel pair	$[V_{\text{U}}^{4\prime}][U_{\text{i}}^{4\bullet}]$	1784
Schottky trio	$[V_{\text{U}}^{4\prime}][V_{\text{O}}^{\bullet\bullet}]^2$	993

Hyperstoichiometry. In the case of hyperstoichiometric uranium dioxide, anion and cation mobility are further enhanced. Qualitatively, it is known that using oxygen-rich materials facilitate sintering of UO_2 , thereby enhancing cation diffusion. Ando and Oishi [And83] reported published activation energies 90 to 100 kJ/mol for oxygen self-diffusion in UO_{2+x} that appeared to be independent of the degree change of x .

Hawkins and Alcock [Haw68] measured cation tracer-concentration depth profiles by alpha-ray spectrometry in single and polycrystalline hyperstoichiometric (UO_{2+x} , $x = 0.01, 0.03, 0.10, 0.15$) uranium oxide. They observed that volume contributions dominated near surface, whereas grain boundary contributions to diffusion in polycrystalline samples were virtually identical to the measured profile at large penetrations. Log plots of U diffusion coefficient as a function of off-stoichiometry revealed orders of magnitude increase in the cation diffusion coefficient with small departures from stoichiometry, regardless of single or polycrystalline sample [Haw68]. Insufficient data prevented Hawkins and Alcock from ascertaining the mechanism of cation diffusion in UO_{2+x} .

Oxidation behavior. The oxidation of UO_2 is commonly observed as a two-step process [Bla58, Ban68, McE97a, McE97b]. Initially, excess oxygen is interstitially accommodated into the cubic fluorite-type UO_2 structure [And83], resulting in an oxygen hyperstoichiometry and ultimately distorting the cubic lattice. Given a sufficient supply of oxygen and thermal energy to the system, the O/U ratio increases until the cubic matrix no longer supports the excess anions. The material then undergoes a phase transformation to $\text{U}_3\text{O}_7/\text{U}_4\text{O}_9$ that Willis [Wil87] denotes as

an ordered superlattice structure, and subsequently transforms to orthorhombic U_3O_8 . Boase and Vandergraaf [Boa77] observed that tetragonal U_3O_7/U_4O_9 remained the stable phase at temperatures below 250°C, whereas U_3O_8 was the stable end product at higher temperatures. Table 2-2 lists the three competing reactions that are suggested as the principal mechanisms that occur for UO_2 oxidation [Boa77].

The transformation of UO_2 to U_3O_7 occurs initially and is a surface reaction that proceeds at the solid/gas interface, with a limiting thickness of ~22 nm. Boase and Vandergraaf [Boa77] reported that the oxidation of U_3O_7 to U_3O_8 at 235°C was significantly slower than the UO_2 to U_3O_8 reaction. The two bulk reactions that form U_3O_8 therefore occur simultaneously and in competition with each other, particularly in high surface area powders.

Blackburn et al. [Bla58] measured the rate of UO_2 oxidation to determine the reaction mechanism. They observed that the weight gain versus time curve for the UO_2 to $UO_{2.33}$ reaction did not indicate any apparent change in mechanism. Below 300°C, a surface layer of single phase γ - U_3O_7 was immediately formed and further oxidation was controlled by oxygen diffusion through this phase, such that the oxidation rate was inversely proportional to oxide thickness. The second oxidation stage, which has been shown to be a nucleation and growth process, [Bla58] exhibited an induction period, a gradually increasing reaction rate, and finally a region in which the rate slows as the final composition approaches $UO_{2.67}$.

Table 2-2. Oxidation reactions of UO_{2+x}

Oxidation reaction	Comments
(1) $6UO_2 + O_2 \rightarrow 2U_3O_7$	Fast; surface only
(2) $2U_3O_7 + O_2 \rightarrow 2U_3O_8$	Slow at temperatures < 250°C; surface only in coarse powders
(3) $3UO_2 + O_2 \rightarrow U_3O_8$	Faster than reaction (2); occurs in the bulk only

Surface area dependence. The individual contributions of these competing reactions (#2 and #3 from Table 2-2) in the UO_2 system are dependent on the specific surface area of the sample, and separating them is often difficult. Because both surface and bulk reactions occur simultaneously, the surface to volume ratio of the sample has a significant bearing on the relative

contributions of the various oxidation mechanisms. In fact, Dobrov et al. [Dob98] cited work that showed the surface oxygen exchange is a relatively slow process and is the rate-limiting step, not solid-state diffusion, of fuel oxidation in thin samples where surface contribution is greater than bulk. Experiments reported using powders with specific surface areas ranging from 0.61 to 19 m²/g [Ban68] indicated a direct relationship between the final O/U ratios of the oxidized materials and the specific surface area of the samples. Taylor et al. [Tay98] studied the rate of U₃O₈ formation as a function of pellet surface roughness at 250°C and noted that reaction times increased by a factor of four with increasing roughness, corresponding to an increase in the nucleation and growth rate constant, κ , by two orders of magnitude. A nonlinear relationship between κ and surface roughness was observed such that κ was independent of surface roughness with very fine (< 1 μm) or coarse (18-100 μm) polishing agent particle size. For 1-18 μm particle size polishing media, κ values increase with media particle size. Taylor et al. attributed this correlation of κ with roughness to a combination of at least three factors: increasing macroscopic surface density of nucleation sites, increasing microscopic surface density of nucleation sites, and preferred oxidation in the <111> direction. The 36% volume expansion is largely accommodated in the <111> UO₂ direction, which becomes the <001> direction (*c* axis) of orthorhombic U₃O₈.

Activation energies. A wide range of experimentally determined activation energy values has been reported for the oxidation of UO₂. The results of previous UO₂ oxidation studies have been summarized in the literature [McE97a-b]. See Appendix A. Activation energies for the formation of U₃O₇/U₄O₉ on unirradiated UO₂ fuel and spent LWR fuel have been reported to range from 90-120 kJ/mol [McE97a]. Values for the oxidation of UO₂ fuel and spent-fuel to U₃O₈, determined with a variety of experimental techniques, exhibit a much larger range, from 48-172 kJ/mol [McE97b]. The broad range in experimental values for UO₂ → U₃O₈ oxidation highlights the complexity of the oxidation process for this material, such as grain boundary diffusion, off-stoichiometry (O/M), oxidizing conditions, and/or in-reactor conditions.

Thorium Oxide

A naturally abundant material, thorium oxide has found use in a variety of products from portable gas mantles to catalyzing petroleum cracking. It is also an identified fertile material used for producing nuclear fuel. Although not fissile, thorium-233, like uranium-238, absorbs slow neutrons to produce fissile uranium-233. The comparison with uranium reveals a host of properties that can be exploited in the waste end of the nuclear fuel cycle.

Thorium oxide possesses a molecular weight, cation radius, and lattice structure similar or identical to UO_2 . Not surprisingly, ThO_2 forms solid solutions with UO_2 at all U/Th ratios.

Table 2-3 summarizes some material properties of ThO_2 and UO_2 .

Table 2-3. Material properties of ThO_2 and UO_2

Material property	ThO_2	UO_2
Metal electron configuration	$[\text{Rn}] 6d^2 7s^2$	$[\text{Rn}] 5f^3 6d^1 7s^2$
Metal atomic number	90	92
Metal atomic weight	238.0289 g/mol	232.0381 g/mol
Metal atomic radius (neutral)	1.8 Å	1.75 Å
Cation radius*	1.18 Å	1.14 Å
Melting point	3390°C	2827°C
Density ⁺	9.986 g/m ³	10.977 g/m ³
Lattice structure ⁺	Fm3m (225)	Fm3m (225)
Lattice parameter ⁺	5.600 Å	5.467 Å
Lattice energy	10397 kJ/mol	10644 kJ/mol
Radioisotope half-life	1.4×10^{10} y (Th^{232})	4.46×10^9 y (U^{238})

* radii for coordination number (CN) = 8 and valence = 4+ [Ric92]

⁺ JCPDS Diffraction data 04-0556 and 41-1422, respectively

Defect structure. Transport phenomena within the thorium oxide lattice are important to predict mobility behavior of inclusions, such as uranium and fission products generated in-reactor. As with other fluorite-structured materials, anion Frenkel defects (oxygen vacancy-interstitial pair) are thought to be the predominant intrinsic disorder, with cation vacancies and holes as minor defects [And76, Col83]. Calculated effective formation and migration energies for intrinsic disorder reported by Colbourn and Mackrodt [Col83] further support thorium oxide stability over uranium dioxide, as summarized in Table 2-4, where cation interstitials appear to be far too energetic to play any significant role in the cation disorder of thorium oxide.

Table 2-4. Cation and anion formation and migration energies in ThO₂

	ThO ₂ (eV)
Effective formation energies for intrinsic disorder	
Anion vacancy	~3.00
Anion interstitial	~3.00
Cation vacancy	5.93
Cation interstitial	13.87
Anion migration	
Vacancy	0.78
Direct exchange	5.80
Direct interstitial	3.27
Interstitialcy mechanism	0.92
Direct interstitial migration of O _i ⁻	4.28
Cation migration	
Vacancy	7.04
Divacancy	5.36
Trivacancy	6.35

Oxidation behavior. Results published by Ando et al. [And76, And79] of single crystal 99.99% purity ThO₂ indicate that oxygen diffusion kinetics are rate limited by surface exchange at temperatures 973°C to 1593°C with respect to time. Concavity was observed at initial and final times when fractional O¹⁸ uptake is plotted as a function of diffusion time. However, oxygen self-diffusion, with respect to temperature dependence, did not appear to be influenced by specimen size and pre-annealing. The temperature dependence of oxygen self-diffusion split into a high (> 1100°C) and low (< 1100°C) region, which Ando et al. [And76] attributed to intrinsic and extrinsic oxygen diffusion, respectively. Further work by Ando and Oishi [And79] show ThO₂ ionic conduction primarily comes from oxygen self-diffusion and is independent of oxygen partial pressure.

Impurities in thoria. Experimental investigations of the presence of impurities in the thorium oxide lattice are largely concerned with electrical conductivity of solid solutions to shed light on the defect structure. Colbourn and Mackrodt [Col83] reported vacancy binding energies for di- and tri-valent cation impurities, including Th³⁺, which give rise to anion vacancies for ionic conduction in the thorium oxide lattice. Di-valent impurities gave rise to greater substitution and vacancy binding energies than tri-valent; and decreased in magnitude with decreasing dopant radii. [Col83] As would be expected, smaller impurities and, particularly,

valency close to 4+ ease inclusions into the lattice. It stands to reason that U^{4+} , with its similar radii to Th^{4+} , and any of the lanthanide or actinide elements, particularly those with 4+ valency, would be energetically favorable impurities accommodated in the thorium oxide lattice.

Uranium-Thorium Mixed Oxide

The oxidation behavior of $(U,Th)O_2$ solid solutions has been studied previously. Within a composition range of 24% to 90% moles of uranium dioxide, $(U,Th)O_2$ phases are always single phase cubic fluorite type when oxidized at temperatures below 200°C [And54]. In high uranium concentration (> 95% mol) unoxidized pellets at room temperature, lattice parameters increased linearly with decreasing uranium content, reflecting Vegard's law that implies atomic volume is conserved regardless of local lattice distortions [Tsu98]. Chandramouli et al. [Cha98] noted the cubic fluorite structure was maintained irrespective of uranium content of unoxidized $(U,Th)O_2$ solid solutions.

Oxidation of compositions containing less than 50% mol UO_2 yielded only fluorite phases under any conditions. Mixed oxides containing greater than 50% mol UO_2 , however, formed second non-cubic phases, hexagonal or orthorhombic U_3O_8 [And54, Cha98]. X-ray diffraction patterns indicated the presence of a U_3O_8 second phase, which disappears upon reduction heating at 1300°C, results in uranium depletion from the solid solution [Cha98]. Anderson et al. [And54] observed that mixed oxides containing less than 78% UO_2 were stable in air up to 1400°C, except for 66% UO_2 which lost its cubic structure in high-pressure oxygen conditions. Otherwise, high uranium compositions, such as $U_{0.9}Th_{0.1}O_2$, evidenced x-ray pattern broadening (indicative of unit cell contraction), breakdown of cubic lattice symmetry when oxidized below 200°C, phase separation above 200°C oxidation, and a final orthorhombic U_3O_8 -like structure at 600°C [And54]. Anderson et al. deduced that for UO_2 concentrations from 15 to 78% mol, excess oxygen entered interstitial sites in the fluorite lattice based on changes in unit-cell density, which increased with oxidation in agreement with theoretical calculations. Unit cell

parameters, however, demonstrated a parabolic relationship with uranium valence, such that a minimum was observed near U valence = 5. Anderson et al. interpreted this behavior as a competition between initial ionic attraction and volumetric accommodation of excess anions.

Aronson and Clayton [Aro60] examined (U,Th)O₂ compositions synthesized by ammonium hydroxide co-precipitation, with UO₂ contents ranging from 30 to 90% mol and x-ray diffraction patterns confirmed a single phase fluorite-type structure present at all compositions. Following controlled oxidation and annealing at 800°C, it was observed that the added oxygen was accommodated without destroying the fluorite structure.

The activation energy of (U,Th)O₂ oxidation has been studied using thermogravimetric techniques [Ant00]. All of the samples studied exhibited single-step weight-gain curves. For low uranium content (U_yTh_{1-y})O₂ powders (y = 0.15 and 0.30), the average activation energy for oxidation was calculated to be 45 kJ/mol. Higher uranium content powders (y = 0.72 and 0.77) had average activation energies of 74 kJ/mol. The higher activation energy for higher uranium content powders was attributed to the phase separation that occurs when these materials are oxidized at high temperatures.

Oxidation potential. Ugajin [Uga82] prepared (U,Th)O₂ samples with 5%, 10%, and 20% mol UO₂ to measure the oxygen potential of non-stoichiometric mixed oxides as compared to UO_{2+x} at 1000°C to 1200°C in CO₂/CO atmosphere. Oxygen potentials of mixed oxides, like UO₂, increased with increasing O/M at all temperatures and compositions. Assuming Th valence is constant at 4+, Ugajin observed oxygen potentials increased with increasing Th content and U valency more so than UO_{2+x} at greater deviations from stoichiometry. Supplemented by Anthonyamy et al. [Ant97] and Arima et al. [Ari00] measurements of 1%, 3%, 5%, 54% and 90% mol UO₂, the compositional range of (U,Th)O_{2+x} oxygen potential data dependence upon uranium valence and the U/(U+Th) ratio was further affirmed.

Matsui and Naito's [Mat85] work with 20% and 40% mol UO_2 at 1000°C to 1100°C in H_2/CO_2 atmosphere further interpreted the differences between $(\text{U,Th})\text{O}_{2+x}$ and UO_{2+x} oxygen potential behavior according to the dependence of x on oxygen partial pressure expressed as $x \propto P(\text{O}_2)^{1/n}$. Assuming a complex defect (2:2:2) model with two different interstitial oxygen types (O_i^a and O_i^b) and one oxygen vacancy (V_O), Matsui and Naito showed UO_{2+x} to have three different dependencies of x upon $P(\text{O}_2)$ and four regions for $(\text{U,Th})\text{O}_{2+x}$ summarized in Table 2-5 [Mat85].

Table 2-5. Composition dependence on oxygen partial pressure for UO_{2+x} and $(\text{U,Th})\text{O}_{2+x}$

Phase	Composition	n for $x \propto P(\text{O}_2)^{1/n}$	Defect Model
UO_{2+x}	$x < 0.003$	2	Neutral defect $\{2\text{O}_i^a\text{O}_i^b2\text{V}_\text{O}\}$
	$0.003 < x < 0.006$	12	$\{2\text{O}_i^a\text{O}_i^b2\text{V}_\text{O}\}^{5'}$
	$x > 0.006$	2	$\{2(\text{O}_i^a\text{O}_i^b2\text{V}_\text{O})\}'$
$(\text{U,Th})\text{O}_{2+x}$	$x < 0.001$	2	Neutral defect $\{2\text{O}_i^a\text{O}_i^b2\text{V}_\text{O}\}$
	$0.001 < x < 0.003$	4	$\{2\text{O}_i^a\text{O}_i^b2\text{V}_\text{O}\}'$
	$0.003 < x < 0.008$	12	$\{2\text{O}_i^a\text{O}_i^b2\text{V}_\text{O}\}''$
	$x > 0.008$	4	$\{2(\text{O}_i^a\text{O}_i^b2\text{V}_\text{O})\}'''$

Polycrystalline diffusion. Furuya [Fur68] measured cation (^{237}U) diffusion in ThO_2 and UO_2 - ThO_2 polycrystalline pellets with average grain sizes over 60 μm over temperatures ranges 1800°C to 2000°C and 1800°C to 2300°C, respectively. As expected, lattice diffusion made a significant contribution near surface, resulting in a non-linear concentration profile. Deeper penetration regions show ^{237}U concentration varied linearly with distance, characteristic of grain boundary diffusion. Excluding the section nearest to the free surface, Furuya [Fur68] calculated lattice and grain-boundary diffusion contributions. Comparison of the associated activation energies showed that lattice diffusion through $(\text{U,Th})\text{O}_2$ (360 kJ/mol) is greater than ThO_2 (320 kJ/mol). Furuya deduced the smaller lattice spacing in $(\text{U,Th})\text{O}_2$ caused the potential barrier at the saddle point to increase compared with ThO_2 . Both values were greater than values reported in nominally stoichiometric UO_2 (304 kJ/mol), with implications of the influence of off-stoichiometry on cation diffusion. Activation energies for grain boundary diffusion (269 and 201

kJ/mol), as expected, were significantly lower than lattice diffusion and also saw the same relationship between (U,Th)O₂ and ThO₂, respectively.

Ando et al. [And85] measured uranium oxide evaporation mechanism and rate-controlling step for polycrystalline Th_{0.90}U_{0.10}O_{2.05} and Th_{0.75}U_{0.25}O_{2.13} after heating at 1650°C in flowing air for 32 h. UO₂ and ThO₂ concentrations varied to a depth of approximately 20 μm and 80 μm from the surface in the 10% UO₂ and 25% UO₂ samples, respectively. The concentration profiles showed that uranium oxide preferentially vaporizes. Pores and cracks were also observed after evaporation annealing, with the cracks and voids decreasing with increasing depth. Cation diffusion, further enhanced by grain boundaries, was identified as the rate-controlling mechanism.

Background of Synthesis Methods

The powder-pellet route involves generation and handling of fine powder or particles (<1μm) and is hence associated with the problem of radiotoxic dust hazard and fire hazard (applicable for carbide and nitride powders). Further, the fine powders are not free flowing and pose problems in remote and automated fabrication. Microhomogeneity of fissile species in mixed oxide is not fully obtained since the oxide powders are mechanically mixed. The alternative sol-gel type processes use dust-free, free-flowing and coarse (100 to 2000μm) particles as starting materials for pellet making.

The choice of uranium oxide as a nuclear fuel is because of its high melting point (2828 ± 20°C), corrosion resistance to radiation damage, and irradiation stability. The physico-chemical characteristics of UO₂, such as density, surface area, pore structure, grain size, crystallite size, sphericity, and oxygen to uranium ratio, depend mainly on the preparation method [Abd90]. Sol-gel “wet” methods are typically preferred over traditional dry powder milling for producing spherical particles. The sol-gel processes have been developed and applied at Oak Ridge National Laboratory (USA), AERE (United Kingdom), KEMA (Netherlands), CNEN (Italy),

KFA Julich (FRG), and Tokai, Japan for high density thorium oxide and/or uranium oxide microspheres [Abd90].

The oxalate precipitation method is the primary process for commercially produced thorium oxide. White et al. [Whi81] investigated precipitation temperature, agitation method, and digestion time to refine powder sinterability and density without milling for ThO₂ and 25% UO₂-ThO₂. A 10°C temperature, mechanical stirring, and 15 min digestion yielded the most sinterable powder with 96% theoretical densities (TD) without milling. Temperature was identified to have the most effect upon particle morphology, surface area, crystallite size, and sinterability. The lower (10°C) digestion temperature, however, yielded cubic particles less than 1 μm in size. At 70°C, the particles were square platelets varying in size from 1 to 3 μm along the square edge. Longer digestion times rounded off the edges and generally produced more uniform particle sizes

Ganguly et al. [Gan86] examined thorium oxide and uranium oxide microspheres by well-established Societa Nazionale Matanodoti (SNA) and Kernforschungsanlage Julich (KFA) external gelation and KFA and Keuring Electrotechnische Materialen Arnkem (KEMA) internal gelation processes. Pellets made by each of the processes, however, presented relatively poor densities and general behavior. Particle size, density, and crushing strength influenced pressing characteristics. Specific surface area, crystallite size and additives determined sintering behavior. Ganguly et al. noted that adding a sintering aid (CaO) and pore forming additive (carbon black) improved pelletization and sintering ($\geq 94\%$ TD).

Chandramouli et al. [Cha98] observed that surface area of mixed oxide powders were influenced by composition and calcinations method. As U content increased, surface area of conventionally calcined powders decreased. Microwave heating also resulted in low surface area powders with large crystallite sizes. Solid solutions with 15% mol U content calcined by a graphite coupling agent yielded surface areas nearly twice that of conventional furnace calcined

powders. Residual carbon content, also, was greater in microwave-calcined powders than those heated by conventional furnace.

Kinetic Analysis

The Arrhenius approach is used to interpret the rate dependence of thermal decomposition of solids on temperature. Predicting how quickly the solid state (U,Th)O₂ system approaches equilibrium does not necessarily require full understanding of the complicating features of real systems. Simple approximate theoretical kinetic models can be used to interpret experimental data and make predictions of (U,Th)O₂ behavior at the end of the nuclear fuel cycle. Additionally, knowledge of UO₂ and ThO₂ defect structures and oxidation mechanisms can lay the groundwork for fully revealing the mechanisms that predominate (U,Th)O₂ oxidation (i.e., diffusion and/or nucleation and growth).

Kinetic reaction models. Basic solid state reaction models, $f(\alpha)$, are largely based on simplified geometrical assumptions for reaction particles, such as geometry of reaction interface. Contracting area and volume models assume its basis in the reaction interface and corresponding spatial movement. The Johnson-Mehl-Avrami-Erofe'ev-Kolmogorov and Prout-Tompkins kinetic reaction models describe nucleation and growth processes. Diffusion controlled reaction models, which have largely been developed from gas-solid interactions, assume simplified geometry such as spherical or cylindrical particle shapes and ball-and-stick lattice structures.

Arrhenius equation. Generally, homogeneous kinetics is assumed to behave according to the simple differential kinetic rate and Arrhenius Equations 2-1 and 2-2, respectively. The activation energy, E , is the energy barrier or threshold that must be overcome to enable the bond redistribution steps required to convert reactants into products. The pre-exponential term, or frequency factor, A , is a measure of the frequency of occurrence of the homogeneous reaction situation. This is typically envisioned as including the vibration frequency in the reaction coordinate. From a reaction dynamics treatment [Gal02], the activation energy is identified as the difference between the energy of the molecules undergoing reaction and the overall average

energy. Degree of conversion or fraction reacted, rate coefficient, and kinetic model are expressed as α (where $0 \leq \alpha \leq 1$), $k(T)$, and $f(\alpha)$, respectively.

$$(2-1) \quad \frac{d\alpha}{dt} = k(T) \cdot f(\alpha)$$

$$(2-2) \quad k(T) = A \exp\left[-\frac{E}{RT}\right]$$

The hypothesis is that the reaction involves only an “active part” of all reactant molecules that, according to the Maxwell-Boltzmann distribution law, is an exponential function of temperature [Lvo01]. Galwey and Brown [Gal02] expressed that the Maxwell-Boltzmann equation, which is applicable to homogeneous gaseous systems and a starting point for theoretical explanation of Arrhenius behavior in homogeneous reactions, does not adequately represent the energy distribution of the immobilized reactants of solid-state processes. Mechanisms, such as three-body collisions or linked sequence of steps, which are unique to the constrained mobility of solid-state systems, oppose a single contributing step during the entire reaction as a realistic predictor of decomposition behavior. Additionally, reactant energies in liquid or solution are associated with individual molecules, whereas band theory describes the energy distribution within crystals. Garn [Lvo01] noted that no discrete activated states can exist during the decomposition of a solid. Subsequently, the Arrhenius kinetic parameters (A and E) have lost their physical meaning. Because of the spatial constraints of solid-state processes, there are no collisions of freely moving reactant molecules as defined by the frequency factor for homogeneous reactions. Energy transfer through vibrational interactions within the crystal, also, occurs so fast that no substantial deviations from the average energy can take place [Lvo01].

Limitations. The assumption that kinetic parameters are intrinsic constants, which uniquely characterize a given solid-state process, however, is rather controversial and often leads to misunderstandings since solid-state processes typically exhibit complex kinetics [Mal01]. Although mathematical descriptions can be determined for most solid-state processes to optimize

desired variables, the underlying mechanism is not necessarily easily obtained [Mal01]. Unlike liquid and gaseous systems, reactants in solid-state processes are spatially constrained and place additional complications on the system. Further difficulties that add to the complexity of solid-state processes are inhomogeneous reactant distribution irregular shapes, polydispersity, shielding and overlapping of reacting particles, or preferred orientations [Mal01]. Empirical rate laws developed to address the anomalous reaction orders (kinetic exponents) in the rate law as a result of these complexities are shown in Table 2-6.

Table 2-6. Rate laws for a simple process $A \rightarrow P$

Reaction in solids	
$\frac{d\alpha}{dt} = k \cdot (1 - \alpha)$	1 st order
$\frac{d\alpha}{dt} = k \cdot \alpha(1 - \alpha)$	with autocatalysis
Empirical rate laws	
$\frac{d\alpha}{dt} = k \cdot (1 - \alpha)^n$	1 st order
$\frac{d\alpha}{dt} = k \cdot \alpha^M (1 - \alpha)^N$	with autocatalysis
Fractional conversion α ($0 \leq \alpha \leq 1$), such that $[A] = 1 - \alpha$ and $[P] = \alpha$.	

Solid-state decomposition reaction rates are influenced by numerous factors that could inhibit determination of kinetic parameters. Although it is typically assumed that sample temperature is equal to that of the furnace, [Lvo01] Smith and Topley's work where single crystals in vacuum measured temperatures 4 to 8 K lower than the furnace. L'vov also previously developed a program that theoretically computed the layer-by-layer temperature distribution in powder samples decomposing in vacuum and foreign gases. Depending upon the total number of layers, n , temperature deviations can differ significantly for powders and single crystals. For instance, the temperature of the central layer of a $Mg(OH)_2$ sample with $n = 1000$, 10,000 and furnace temperature of 500 K or 600 K is actually 427 and 387 K, respectively [Lvo01]. Single crystal $Mg(OH)_2$ in vacuum with temperatures 550, 600, and 663 K is expected to have surface temperatures of 549.6, 593 and 628 K, respectively [Lvo01]. Correcting kinetic parameters for

this self-cooling effect is naturally simpler for single crystals. This effect and number of layers, otherwise, must be determined through measurement of grain size, grain number, powder mass, crucible geometry, environmental conditions, and heating rate. With these corrections, it is possible to explain the differences between kinetic parameters obtained under different conditions. Other than the self-cooling effect, other reasons for scatter of reported values of A and E may be differences between mathematical models by different authors and difference in the kinetic parameters for the nucleation and steady-state stages of decomposition [Lvo01].

L'vov [Lvo01] reviewed a "physical" approach for interpreting thermal decomposition of solids that is based on the Hertz-Langmuir prediction of proportional dependence of the evaporation rate on the equilibrium partial pressure of the vapor which, in its turn, depends exponentially on temperature. Most solid-state decomposition reactions proceed under conditions far from equilibrium. The traditional "chemical" approach tackles this deviation from equilibrium by connecting it to the theoretically unpredicted energy barrier, activation energy. In other words, "non-equilibrium decomposition into equilibrium products" [Lvo01]. The "physical" approach, however, contends that the reason for the deviation lies in the decomposition of the reactant into primary non-equilibrium gaseous species different from those at equilibrium. L'vov [Lvo01] asserts this approach permits quantitative interpretation of the mechanism of nucleation and the energy source supporting decomposition, retardation in the presence of gaseous products, low vaporization coefficients, thermal stability, effect of self-cooling, the Topley-Smith effect, and kinetic compensation effect.

CHAPTER 3 MATERIALS AND METHODS

Material Synthesis

Three methods of powder fabrication were used, two of which employed sol-gel type approaches for obtaining a solid solution. The sol-gel type processes yield a co-precipitate from an aqueous solution of uranium and thorium nitrate salts followed by complexation with either an oxalate or hydroxide group. The final method engaged in this study adhered to traditional co-milled powder techniques.

Wet chemistry methods of material synthesis were initially pursued for its known homogeneity advantages over powder-mixing techniques and minimization of dust hazard. Both uranium and thorium are alpha emitters. The hazard, therefore, to be considered for workers are dust particulates becoming airborne and entering the human body. Safety gear, such as protective gloves, eyewear, and clothing, are necessary. Wet synthesis methods, however, present a reduced hazard since the process is largely contained in liquid form prior to heat treatment. Additionally, particle morphology of sol-gel type synthesis is largely spherical; presenting a free-flowing powder that is ideal when filling dies for pellet making. In contrast, mixing by traditional powder co-milling methods occurs entirely in powder form and generates platelet-like particles with less desirable flow characteristics. The details of each material fabrication techniques are presented in the ensuing sections

Oxalate Co-Precipitation

Since UO_2 and ThO_2 are iso-structural, both have face-centered cubic CaF_2 -type lattices, and have similar thermodynamic properties. Their fabrication processes therefore are nearly identical. Aqueous oxalic acid is utilized as the complexation agent to form the mixed oxide. A

flow chart schematic in Figure 3-1 provides a brief synopsis of the steps entailed.

Uranium oxynitrate hexahydrate ($\text{UO}_2(\text{NO}_3)_2 \cdot 6\text{H}_2\text{O}$) and thorium nitrate hydrate ($\text{Th}(\text{NO}_3)_4 \cdot x\text{H}_2\text{O}$) are supplied by Alfa Aesar. Analytical grade oxalic acid ($(\text{COOH})_2 \cdot 2\text{H}_2\text{O}$) and sodium formaldehyde sulfoxylate dihydrate ($\text{HOCH}_2\text{SO}_2\text{Na} \cdot 2\text{H}_2\text{O}$), also purchased from Alfa Aesar, are the complexing and reducing agents, respectively. A 115-volt motorized three-blade stirrer supplied the agitation for the co-precipitation step.

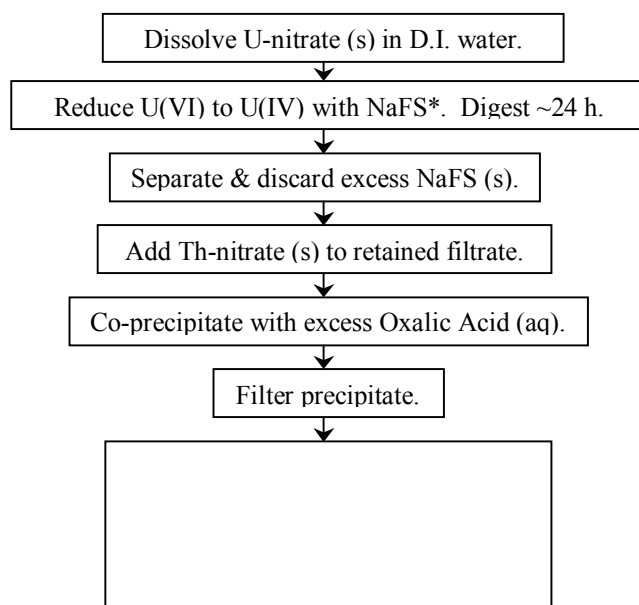


Figure 3-1. Oxalate path co-precipitation. *NaFS is sodium formaldehyde sulfoxalate.

The desired molar ratio of uranium to thorium determines the starting quantities of solid nitrate salts. Uranium (IV) nitrate solution is prepared by dissolving uranium (VI) oxynitrate hexahydrate in a sufficient volume of demineralized water to yield an approximately 1M concentration. Since thorium (IV) nitrate is later added in solid form, additional water is added to the solution to achieve a thorium concentration of 1M. The nitrate solution is then reduced via addition of a six-fold excess of the reducing agent at room temperature and covered for 24 h. The solution changes colors from yellow to orange to dark green. After digestion, the excess reducing agent solid is removed by vacuum-assisted filtration with Whatman #42 ashless filter paper and thorium nitrate hydrate is dissolved into the nitrate solution.

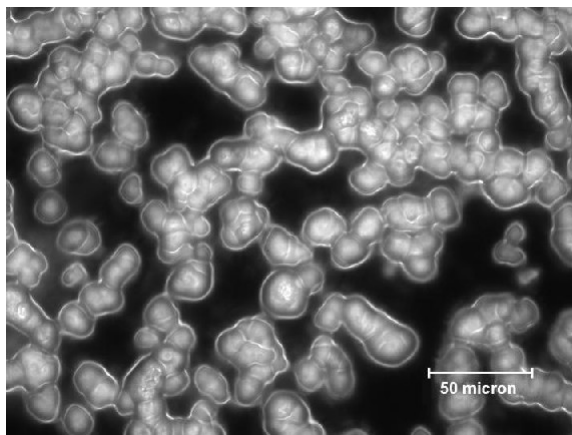


Figure 3-2. Optical micrograph of nominal 20% UO_2 calcined oxalate-synthesized powder mounted with a collodion/amyl acetate solution at 50x magnification

To form the co-precipitate, a six-fold excess of the oxalic acid complexing agent, dissolved in demineralized water to a 1M concentration, is added via one of two dropwise methods to the nitrate solution under ~ 600 rpm mechanical agitation. The two assemblies, buret and dropping funnel, were employed for oxalic acid addition to yield a fine particle size and spherical morphology. The buret formed a somewhat finer particle size than the dropping funnel due to the smaller aperture of a buret, which produced a smaller drop size. Because the agitation speed was held constant, drop size was the primary means of controlling particle size. A coarser powder, however, was desired to reduce airborne dust hazard and assist sieve particle size classification. Powders fabricated by either method demonstrated the desired free-flowing characteristics for pellet making. An optical micrograph (Figure 3-2) of nominal 20% UO_2 – 80% ThO_2 calcined powder demonstrates the spherical morphology observed with this method.

Following the complexation of U and Th to the oxalate group, the precipitate is separated by vacuum-assisted filtration through #42 Whatman paper and dried in air at room temperature until it releases easily from the paper. The filtrate liquid is clear, an indicator that most of the uranium did not remain in solution. X-Ray Fluorescence performed by co-researcher Shibuya of the liquid filtrate confirmed this assertion. The precipitate cake, which is white-colored, is

transferred to a glazed ceramic crucible. Eliminating the residual moisture and undesired organics (i.e., carbon) subsequently requires a series of drying, decomposition, and calcination steps carried out in air, followed by a final reduction heating in flowing 5% H_2 -Ar. Powder color following reduction that was performed in a tube furnace on an Alumina boat varied from tan to dark orange. Because of the multiple oxidation states available to uranium, which readily oxidizes, the final reduction step is needed to return it to U(IV) and face-centered cubic lattice structure. Since the powder will later be formed into pellet geometry and sintered, reduction is carried out at 800C to prevent particles from sintering. The molecular evolution of the co-precipitate is depicted in Table 3-1 where U/Th is 1 and X-Ray Diffraction pattern in Figure 3-3 for nominal U/Th = 5/95.

Table 3-1. Evolution of oxalate-synthesized (U,Th) O_2 .

	Gas	T(°C)	Equation
Filter	air	25	$\text{U}(\text{NO}_3)_4\text{-Th}(\text{NO}_3)_4 + 4\text{H}_2\text{C}_2\text{O}_4 \rightarrow [\text{U}(\text{C}_2\text{O}_4)_2\text{-Th}(\text{C}_2\text{O}_4)_2] \cdot n\text{H}_2\text{O} + 8\text{HNO}_3$
Dry	air	120	$[\text{U}(\text{C}_2\text{O}_4)_2\text{-Th}(\text{C}_2\text{O}_4)_2] \cdot x\text{H}_2\text{O} \rightarrow [\text{U}(\text{C}_2\text{O}_4)_2\text{-Th}(\text{C}_2\text{O}_4)_2] + n\text{H}_2\text{O}$
Decompose	air	350	$[\text{U}(\text{C}_2\text{O}_4)_2\text{-Th}(\text{C}_2\text{O}_4)_2] \rightarrow \text{U}(\text{CO}_3)_2\text{-Th}(\text{CO}_3)_2 + 4\text{CO}$
Calcine	air	900	$\text{U}(\text{CO}_3)_2\text{-Th}(\text{CO}_3)_2 \rightarrow \text{UO}_{2+x}\text{-ThO}_2 + 4\text{CO}_2$
Reduce	5%H-Ar	800	$\text{UO}_{2+x}\text{-ThO}_2 + n\text{H}_2 \rightarrow \text{UO}_2\text{-ThO}_2 + n\text{H}_2\text{O}$

Drying steps carried out in air were performed in a Vulcan 3-550 Muffle Furnace. The final reduction drying at 800C took place in either a CM Rapid Temp or Lindberg/Blue 54434C tube furnace with Mullite and, later, 99.8% Alumina open-ended tubes supplied by Coors. Two sets of custom-made stainless steel caps were installed to control gas atmosphere during firing. The initial design was suspected of not maintaining an appropriate seal between the steel and ceramic, presenting carbon content issues for preliminary synthesis attempts. The latter design incorporated a high temperature Viton polymer gasket situated between the stainless steel cap and ceramic tube. Additionally, a vacuum set-up was assembled whereby the tube atmosphere could be evacuated and backfilled with the desired gas, thereby preventing the material from encountering an oxidative atmosphere. The tube atmosphere is evacuated and backfilled with 5%H-Ar three times before initiating the desired firing regime. Figures 3-4 and 3-5 show each furnace.

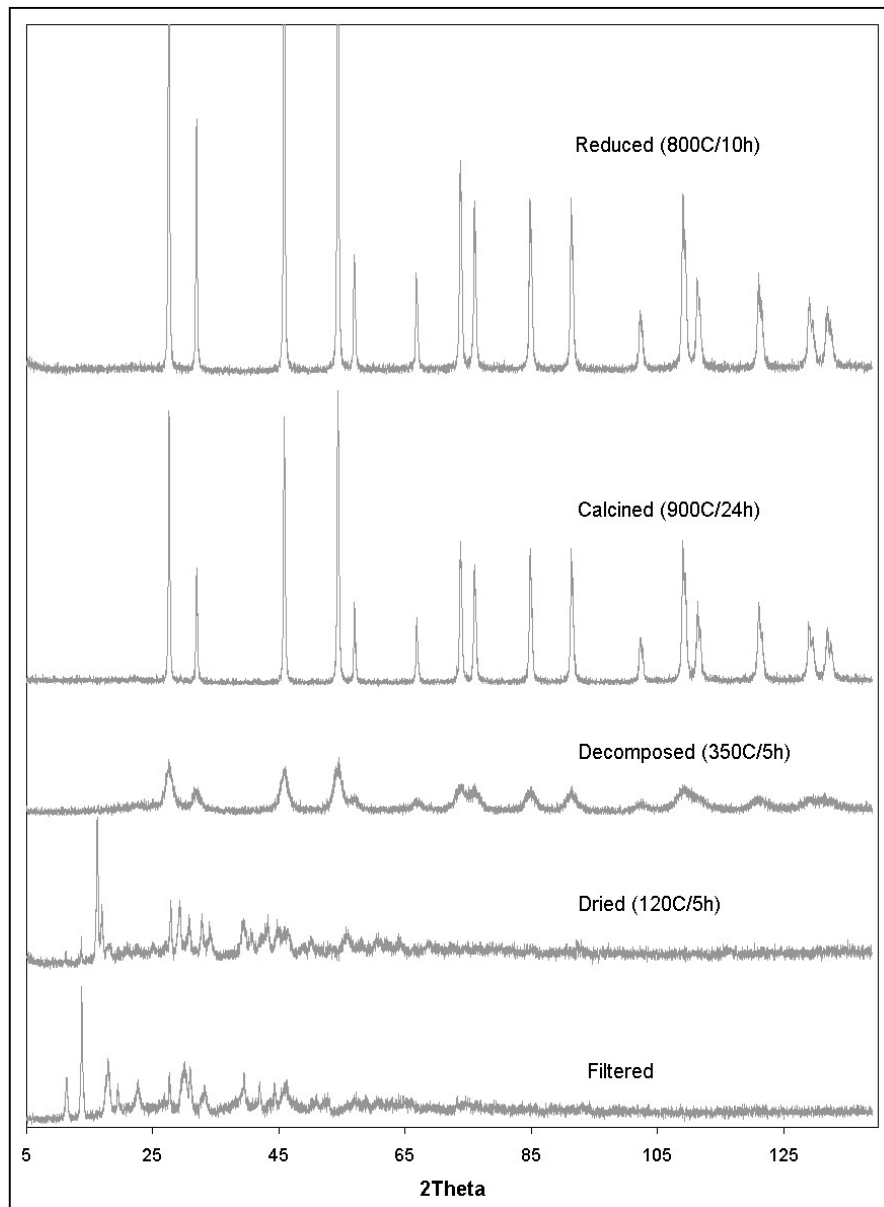


Figure 3-3. X-Ray Diffraction evolution of $U_{0.05}Th_{0.95}O_2$ oxalate synthesized powder.



Figure 3-4. Vulcan Muffle furnace used for drying, decomposition, and calcination

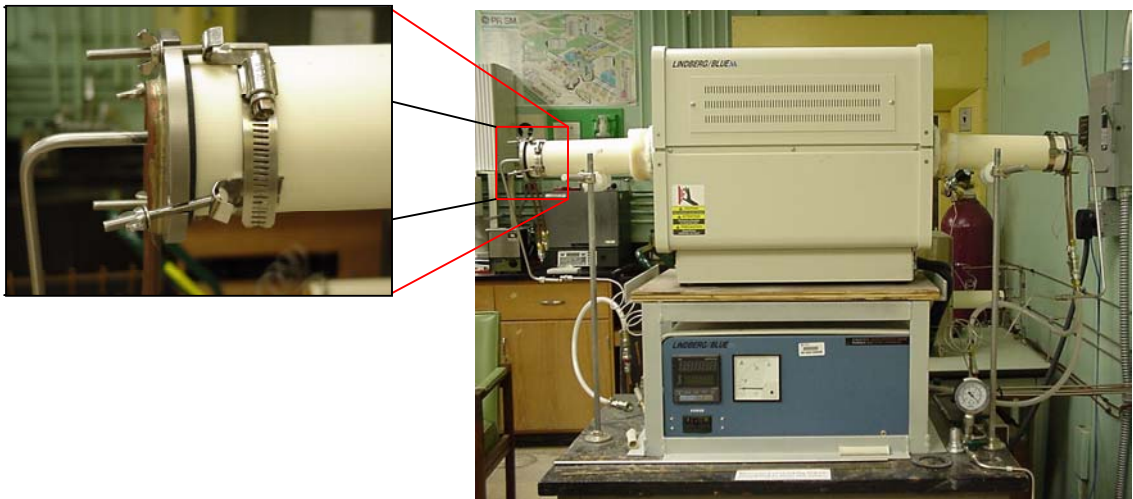


Figure 3-5. Lindberg high temperature tube furnace (right) with alumina tube and stainless steel cap (above)

Ammonium Hydroxide Co-Precipitation

Another synthesis path used was derived from a modification of the well-documented Ammonium Diuranate (ADU) process, which is used in commercial processing of UO_2 fuel. The purposes of attempting this synthesis path did not extend beyond establishing a preliminary qualitative comparison with the oxalate path and traditional blending. Consequently, only a nominal 20% UO_2 composition of moderate quantity (5 grams) was processed. The quantities and specifications of the subsequent procedure were adapted from parameters made available by Dr. E. Lahoda of Westinghouse, Inc. A brief schematic of the procedure follows in Figure 3-6.

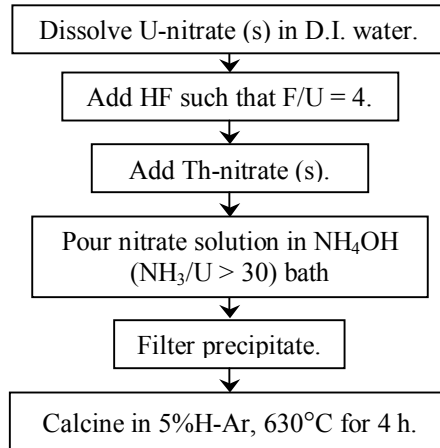


Figure 3-6. Ammonium hydroxide path co-precipitation

Starting constituents were uranium oxynitrate hexahydrate ($\text{UO}_2(\text{NO}_3)_2 \cdot 6\text{H}_2\text{O}$) and thorium nitrate hydrate ($\text{Th}(\text{NO}_3)_4 \cdot x\text{H}_2\text{O}$) supplied by Alfa Aesar, and 49% diluted hydrofluoric acid (HF) and 29% diluted ammonium hydroxide (NH_4OH). Desired molar quantities of uranium (IV) and thorium (IV) nitrate were determined. In demineralized water, uranium (IV) nitrate was dissolved to yield a 0.19 M solution. A molar excess of hydrofluoric acid was added to the uranium (IV) nitrate solution by pipette to raise the molar ratio F/U to 4. No color change or other apparent reaction observed. At this stage, thorium (IV) nitrate was stirred into the solution until dissolved. The solution took on a transparent green-yellow hue. A 30-fold molar excess of ammonium hydroxide aqueous bath was prepared separately. Without agitation, the nitrate salt

solution was poured directly into the ammonium hydroxide bath. A bright yellow colored precipitate immediately formed. The precipitate was removed from the liquid by vacuum-assisted filtration through a Whatman #42 ashless paper and rinsed with demineralized water. The precipitate had an “orange juice” pulp-like appearance, as shown in Figure 3-7 at left, which was starkly different from the white oxalate precipitate. Additionally, the volume of material for this 5-gram batch appeared more voluminous than oxalate-synthesized batches. Following filtration, the yellow cake was air dried until it easily released from the filter paper.



Figure 3-7. Ammonium hydroxide synthesized $(U_{0.2}Th_{0.8})O_{2+x}$ before (l) and after (r) calcinations

Since the hydroxide path did not introduce organic substituents, the heat treatment scheme was decidedly simpler than for the oxalate path. In a flowing 5%H-Ar reduction atmosphere, the yellow cake was calcined at 630C for 4 hours. A significant volume reduction and color change from yellow to nearly black occurred during calcinations as shown in Figure 3-7 at right. X-ray diffraction patterns, taken prior to and following calcinations, revealed the cubic fluorite structure. Silicon was used as an external standard for XRD measurements of hydroxide-synthesized material before and after calcinations.

Co-Milled Mixed Oxides

Uranium dioxide and $(U_yTh_{1-y})O_2$ solid solutions with $y = 0.236, 0.368,$ and 0.500 were prepared by mixing appropriate amounts of UO_2 and ThO_2 powders supplied by Siemens (SM) and Alfa Aesar (AA), respectively. Thorium and uranium oxide powders supplied by Alfa Aesar are manufactured to a below 325 mesh ($< 45\mu m$) and 50 mesh ($< 300\mu m$) particle size

distributions, respectively. Optical micrographs of these powders affixed with a 1:7 collodion and amyl acetate solution are shown in Figure 3-8. From the micrographs, it is apparent that the ThO_2 agglomerates easily, forming large clumps, suggesting a platelet-like morphology. Uranium (IV) oxide particles from AA, on the other hand, presented spherical morphology and demonstrated good flow.

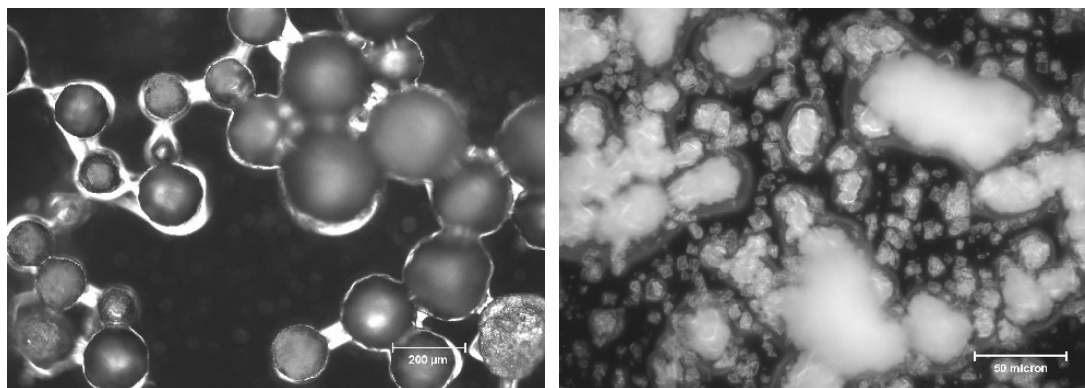


Figure 3-8. Optical micrographs of Alfa Aesar UO_2 (l) and ThO_2 (r)

Co-milling. Preliminary co-milling trials were conducted with high-density polyethylene (HDPE) jars, zirconia ball media, and a laboratory roller mill assembly. Milled powder became imbedded in the HDPE jar walls and clung to ball media. Cleaning jars and media was tedious and difficult. The material lost in the cleaning process, also, directly has an effect on the final U/Th composition. This set-up, therefore, was abandoned in favor of a small batch high impact mixer.

Powders were weighed and batch milled for 60 minutes in a zirconium oxide jar with two 10-mm yttria-stabilized zirconia (YSZ) milling media using a high energy 8000M SPEX Certiprep Mixer/Mill. The mixer employs a torsional “figure eight” motion for pulverizing and mixing. Zirconia ceramic vial, cap, and ball media, as supplied by the vendor, accommodates loads up to 20 mL for mixing. No zirconia contamination from the container or milling media was found in the milled powders. To prevent cross contamination, grinding vials were cleaned

with dilute nitric acid between each batch. Figure 3-9 displays the mixer and mill jar used in this study.

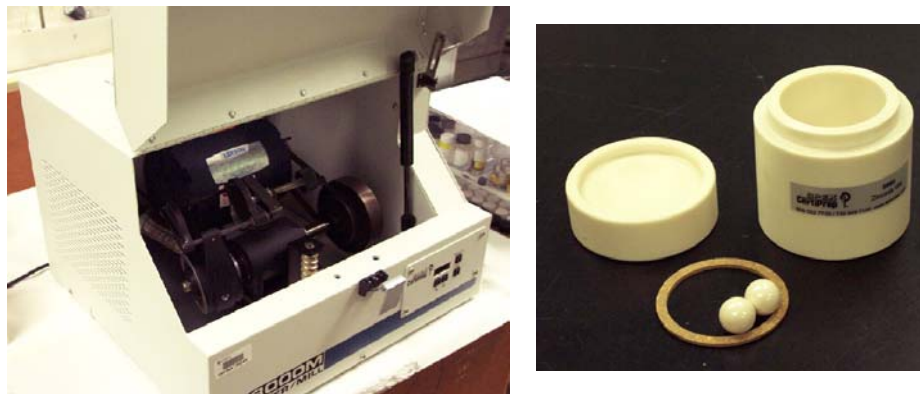


Figure 3-9. 8000M SPEX Certiprep Mixer/Mill (l) and zirconia mill jar (r)

Preliminary runs showed that the high impact velocity of the grinding balls caused powder to pack onto the vial walls. It was necessary, therefore, to mill in 15-minute intervals, scraping vial walls between each interval. After observing this, there was concern the particle size difference between starting powders inhibited effective blending if finer particles tended to pack more easily than coarse particles along vial walls. Because of the particle size and morphology difference between Alfa Aesar UO_2 and ThO_2 , a 2×2 factorial experiment was initially performed to determine effect of fine ($< 63 \mu\text{m}$) versus unsieved milled UO_2 and high (100 MPa) versus low (50 MPa) compaction pressure on sintered pellet density. Pre-milling as-received UO_2 (AA) spherical particles resulted in a platelet-like morphology similar to as-received ThO_2 (AA). A 30-gram batch of UO_2 (AA) was milled four 15-minute consecutive intervals before sieving through a 230 mesh ($63 \mu\text{m}$) to achieve a fine powder batch. It was observed that powder packing along vial walls became progressively hard-packed with each successive milling/blending intervals. Four 15-gram batches of 20% UO_2 – 80% ThO_2 blended for 60 minutes were processed according to the parameters of the experimental matrix shows in Table 3-2. Each batch yielded similar (within 2%) green and sinter densities, indicating little

difference between using fine or coarse UO_2 (AA) and 50 MPa or 1000 MPa uniaxial compaction pressure.

Table 3-2. 2×2 factorial for 20% UO_2 -80% ThO_2 blended oxide

	50 MPa	100 MPa
Unsieved UO_2	×	×
< 63 μm UO_2	×	×

Green and sintered densities were measured three times each with calipers to determine volume. The pellets were sintered at 1650°C in a flowing 5% H_2 -Ar atmosphere. Pellet densities were measured after 5 and 15 hour dwells at 1650°C. Those results are summarized in Table 3-3.

Table 3-3. Co-milled $\text{U}_{0.2}\text{Th}_{0.8}\text{O}_2$ pressing conditions 2×2 factorial results

Pellet Description	Green Density	Sintered Density (5 h)	Sintered Density (15 h)
Unsieved 50 MPa	60.2%	85.8%	97.2%
Unsieved 100 MPa	61.7%	85.7%	98.7%
Sieved 50MPa	61.2%	87.8%	98.1%
Sieved 100 MPa	63.8%	86.7%	98.7%

From the above results, the pressing parameters (100 MPa, sieved) were selected to make pellets for dry oxidation study. P. Demkowicz confirmed by the water immersion technique that sintered densities for the dry oxidation pellets > 98% theoretical density. Those pellets, subsequently, were fragmented by mortar and pestle and classified by ASTM sieves. The 90 to 250 μm particle size range was selected. Demkowicz measured specific surface area of fragments in the 90 to 250 μm range using the multi-point Brunauer-Emmett-Teller (BET) method in a Quantachrome Autosorb 1, with krypton as the adsorbate gas, and found all batches to be within 0.01 – 0.02 m^2/g . Sample quantities were between 2 and 10-g, dried under vacuum at 120°C for approximately 12 hours prior to analysis.

Pellet pressing. The milled ThO_2 - UO_2 powders were initially sieved through 100-mesh (< 149 μm) to remove coarse particles before compaction. The powders were compacted into pellets in a 13-mm diameter stainless steel die using a single action laboratory press at 100 MPa. Pure UO_2 pellets were pressed using pressures of 200 MPa. Stearic acid was used as a lubricant on the die, anvil, and punch sidewalls. The dimensions of the pressed pellets were measured with

calipers and the green densities, obtained by geometrical calculations, were 56% to 64% theoretical density (%TD). Pellets were arranged on a powder mound of matching composition to minimize any possible reactivity with the ceramic setter. The pressed co-milled pellets (Figure 3-10 shows oxalate synthesized pellets) were sintered at 1650°C for 20 hours in a 5% H_2 -Ar gas mixture using a tube furnace fitted with stainless steel end caps. Sintered densities were obtained by immersion methods in deionized water and were between 95% to 98% theoretical density. Those conditions are summarized in Table 3-4.

Table 3-4. Pellet manufacture conditions

Pellet Description	Pressure (MPa)	Green Density (%TD)	Sinter Density (%TD)
23.6% UO_2 – 76.4% ThO_2	100	63.5 ± 0.2	96.8 ± 0.4
36.8% UO_2 – 63.2% ThO_2	100	62.6 ± 0.2	96.2 ± 0.2
50.0% UO_2 – 50.0% ThO_2	100	61.4 ± 0.1	95.3 ± 0.3
100% UO_2	200	49	96.7



Figure 3-10. Pellets prepared using 20% U powder synthesized by the oxalate technique. Powders compacted at 200MPa (left) and 300MPa (right) and sintered at 1600°C for 5 hours in Ar-5% H_2 atmosphere

Pellets were manually crushed in a zirconium container with an alumina pestle.

Fragments were sieved using 60-mesh (250 μm) and 170-mesh (90 μm) ASTM screens.

Generally, about 51% to 61% of the powder was retained on the 170-mesh sieve and about 35% to 42% was collected below 170-mesh. The portions of the crushed pellets below 170-mesh (< 90 μm) were analyzed using x-ray diffraction. The XRD patterns indicated that the samples were

complete solid solutions, with no evidence of secondary phases. The powder distribution retained on the 170 mesh and 60 mesh were not measured by XRD to confirm lattice structure or composition. For materials with significantly different hardness, fragmentation may inadvertently separate the “hard” and “soft” materials. More brittle materials may fragment into smaller particles whereas the harder materials remain large, altering the powder composition. Brinell and Vickers hardness reported for uranium (2400 MN/m² and 1960 MN/m²) and thorium (400 MN/m² and 350 MN/m²) by webelements.com indicate that U is the “tougher” material. It is likely the fine particle distributions may have a lower U/Th ratio than coarser distributions. Again, only the powder retained below 60-mesh/above 170-mesh further characterized. It is unknown whether the fragmentation process may have yielded a high U and low U powder composition.

The specific surface area of the crushed pellets was measured using the Brunauer-Emmett-Teller (BET) method with krypton as the adsorbate gas. The 90 to 250 μm powder samples for surface area analysis were rinsed in demineralized water and dried in a vacuum prior to BET analysis to remove all fine particulates. Measured surface areas for all 90 to 250 μm pellet fragments at all compositions were 0.01 to 0.02 m²/g.

Characterization

X-ray Diffraction (XRD)

Crystal structure indexing, chemical analysis, and lattice parameter calculations were determined from continuous x-ray diffraction scans on a XRD Philips APD 3720 Diffractometer with a Cu anode target, where $K\alpha_1$ wavelength is 1.54056 Å. Generator voltage and current were 40 kV and 20 mA, respectively. With a step size of 0.02°, a range from 10° to 139° was scanned for each sample, with an external Si standard. Lattice parameters were calculated by a graphical and numerical least squares methods and angular separation reported by Popovic [Pop73, Pop85].

Popovic method. Unit cell dimensions were calculated from the angular separation between two Bragg reflections on the basis that shifts occur in the same direction from resultant systematic aberrations. The separation ($\delta = \theta_2 - \theta_1$), therefore, includes the difference between systematic aberrations at the two positions, which is generally smaller than the resultant aberration at either position and removes the necessity of absolute measurements. For a cubic structure, lattice parameter a derived from the separation δ between two diffraction lines, θ_1 and θ_2 , is given by Equations 3-1 through 3-5.

$$(3-1) \quad a^2 = \frac{B_1 - B_2 \cos \delta}{4 \sin^2 \delta}, \text{ where}$$

$$(3-2, 3-3) \quad \begin{aligned} B_1 &= N_1 \lambda_1^2 + N_2 \lambda_2^2 \\ B_2 &= 2 \lambda_1 \lambda_2 \sqrt{N_1 N_2} \end{aligned} \quad \text{and} \quad (3-4, 3-5) \quad \begin{aligned} N_i &= h_i^2 + k_i^2 + l_i^2 \\ i &= 1, 2 \end{aligned}$$

To avoid temperature variations, the second reflection should be chosen within 10° to 20° from the first reflection [Pop73]. The highest possible diffraction angles are used because of the sine nature of Bragg law, $\lambda = 2d \sin \theta$, where θ values near 90° change slowly and, therefore, yield greater accuracy. The sensitivity of this method is reported as

$$(3-6) \quad \frac{\Delta a}{a} = \frac{\Delta \delta \cos \theta_1 \cos \theta_2}{\sin \delta}$$

Method of least squares. The lattice parameter, a , of a cubic structure is directly proportional to the d -spacing according to the relationship

$$(3-7) \quad a = d \sqrt{h^2 + k^2 + l^2}$$

where h, k, l are the miller indices defining any particular set of planes. From measurement of the Bragg angle, θ , interplanar d -spacing can be determined according to Bragg law, $\lambda = 2d \sin \theta$, and a calculated. Since the term $\sin \theta$ appears in Bragg law, precision in d or a depends on precision in $\sin \theta$, not the measured θ . Because of the nature of $\sin \theta$, values of $\sin \theta$ change slowly with θ near 90° . A very accurate $\sin \theta$ value, therefore, can be obtained from a measurement of θ

that may not be particularly precise, provided that θ is near 90° . In other words, the diffracted beam angle is more sensitive to changes in plane spacing when θ is large.

Obtaining measurements near $2\theta = 180^\circ$ are impossible. Since the calculated lattice parameter values approach the true value as 2θ nears 180° , the true value for a can be obtained by extrapolating a plot of measured values against 2θ to 180° . The $\sin\theta$ function, however, yields a nonlinear curve, which is difficult to accurately extrapolate. Depending upon the kind of camera employed, θ can be inserted into certain functions that present linear curves for extrapolation of lattice parameter. For a diffractometer, that function is either $\cos^2\theta$ or $\cos^2\theta/\sin\theta$ depending upon the predominant source or error [Cul78, p.360]. Systematic errors from using a flat, instead of curved, specimen and absorption in the specimen are attributed to the $\cos^2\theta$ function. Displacement from the diffractometer axis, which is typically the largest single source of error, is attributed to $\cos^2\theta/\sin\theta$. A lattice parameter value is then obtained by linear graphic extrapolation of the a vs. $\cos^2\theta$ or $\cos^2\theta/\sin\theta$ plot such that $\theta = 90^\circ$.

Cohen's method. Similar to the least squares method, Cohen's method [Cul78, p.363] applies the least squares technique to the observed $\sin^2\theta$ values directly, instead of to a vs. $\cos^2\theta$ or $\cos^2\theta/\sin\theta$ plots. Squaring, taking the logarithm, and differentiating the Bragg law yield the relationship below.

$$(3-8) \quad \frac{\Delta \sin^2 \theta}{\sin^2 \theta} = -2 \frac{\Delta d}{d}$$

The $\Delta d/d$ term is replaced with an extrapolation function $(-D/R)(\cos^2\theta/\sin\theta)$, where D is specimen displacement and R diffractometer radius, to account for diffractometer error [Cul78, p.359]. The difference, $\Delta \sin^2\theta$, between the true, as defined by unit cell geometry, and observed $\sin^2\theta$ values is set equal to the above equation. Simultaneously solving Equation 3-9 for the set of Bragg lines yields the true lattice parameter, a_0 , at some constant wavelength λ . For ease in calculation, the terms are separated into Equations 3-10 through 3-13.

$$(3-9) \quad \sin^2 \theta(\text{obs}) - \frac{\lambda^2}{4a_o^2}(h^2 + k^2 + l^2) = \Delta \sin^2 \theta = \frac{2D}{R} \cos^2 \theta \sin \theta$$

$$(3-10) \quad C = \frac{\lambda^2}{4a_o^2}$$

$$(3-11) \quad \alpha = h^2 + k^2 + l^2$$

$$(3-12) \quad A = \frac{2D}{R} \frac{1}{10}$$

$$(3-13) \quad \delta = 10 \cos^2 \theta \sin \theta$$

The experimental values of $\sin^2\theta(\text{obs})$, α and δ for each back-reflection inserted into the appropriate terms leave only C and A to be solved. Employing the numeric method of least squares detailed by Cullity [Cul78, p.364], normal Equations 3-14 and 3-15 for cubic systems are simultaneously solved to obtain C and A.

$$(3-14, 3-15) \quad \begin{aligned} \sum \alpha \sin^2 \theta &= C \sum \alpha^2 + A \sum \alpha \delta \\ \sum \delta \sin^2 \theta &= C \sum \alpha \delta + A \sum \delta^2 \end{aligned}$$

Elemental Analysis

Inductively coupled plasma Auger electron spectrometry (ICP-AES). Measurements obtained from ICP-AES were not performed by the author, but by James Jerden, Ph.D. at Argonne National Laboratory. The general technique and results obtained from Dr. Jerden are reported because of their importance in determining the synthesis process of samples to undergo thermogravimetric analysis.

ICP-AES measures the mass spectrum of a sample, typically, from lithium ($Z = 3$) to uranium ($Z = 92$), yielding semi-quantitative, quantitative, elemental and isotopic information for each element. It is a destructive technique where the aqueous sample is nebulized into an aerosol and swept into the ionizing plasma, a high-temperature, atmospheric pressure, and partially ionized gas. The ions generated are carried into a detector for analysis by Auger electron spectrometry. Detection limits are typically in the sub-ppb range for most elements.

Carbon analysis. The LECO WC-200 Carbon Analyzer is a unit specifically designed for tungsten carbide application that provides high precision measurement of carbon content in metals, ceramics, and other inorganic materials. A high frequency induction furnace combusts samples, with accelerators (~ 1 gram each of iron and copper chips) in a quartz crucible, in a pure oxygen environment. The carbon-bearing elements are reduced, releasing the carbon, which immediately binds with the oxygen to form CO and CO₂. These gases are then carried into a molecular trap and then released into infrared (IR) cells. As CO₂ passes through the IR cell, it absorbs IR energy at a precise wavelength within the IR spectrum, preventing it from reaching the IR detector. After passing all IR energy through a narrow bandpass filter to ensure the signal can only be attributed to CO₂, the concentration is detected as a reduction in the energy level at the detector. A five-place balance and burned-off crucibles and lids were handled only with clean tongs to minimize additive error contributions.

Particle Morphology

An exhaustive classification of particle size demands complex sampling and numerous optical micrographs to yield a statistically significant portrayal of size and distribution. Light optic techniques were used to present a qualitative comparison of particle size and morphology processed via co-precipitation, blending, and commercial methods shown in Figure 3-11.

The spherical particles of oxalate synthesized and commercial UO₂ aided pellet making in terms of flowing material into the die and during pressing. Particles did not stick to die walls, unlike the blended (U,Th)O₂ and commercial ThO₂ powders. Since wet synthesized (U,Th)O₂ powders were abandoned for dry oxidation study, this sticking behavior was addressed by using a lubricant, stearic acid, to aid pellet release from the die. These were not necessary to form successful pellets with the oxalate synthesized powders.

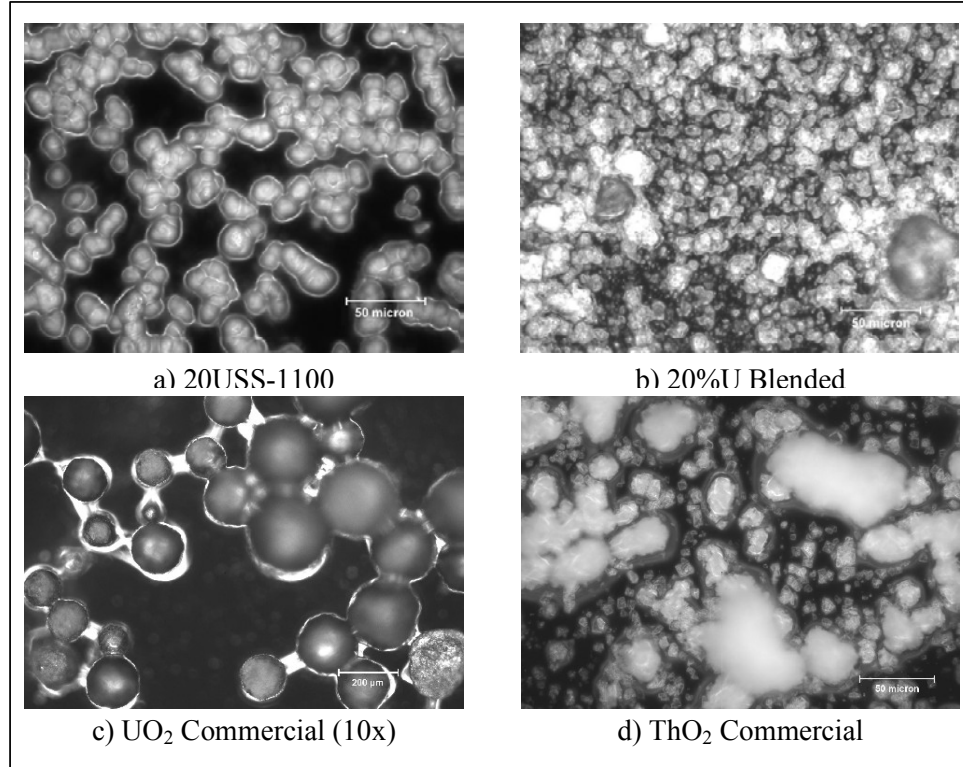


Figure 3-11. Optical micrographs of nominal $U_{0.2}Th_{0.8}O_{2+x}$ made by oxalate synthesis (a), blended (b), and commercial UO_2 (c) and ThO_2 (d) powders

Pellet Density

Green pellet densities were measured with a Mettler AB-104S balance and calipers. Volumes were calculated under the assumption that pellets formed perfect cylinders. Densities of sintered pellets, however, were measured by immersion in water. First, a dry weight (A) was taken. Then, the pellet is immersed in water and the difference between the weight wet and immersed pellet is the buoyancy (P). The density is calculated based on Equation 3-16.

$$(3-16) \quad \rho = \frac{A}{|P|} \cdot \rho_{water}$$

Dry Oxidation

Thermogravimetric Analyzer

Nonisothermal and isothermal dry oxidation experiments were conducted on the crushed pellets (90 to 250 μm powder) in a TA Instruments TGA 2050 thermal gravimetric analyzer, as shown in Figure 3-12, with air flowing at 90 cm^3/min through the sample chamber. Approximately 8 to 20 mg of the 90 to 250 μm pellet fragments were heated to 900°C at rates of 1, 3, and 5°C/min while monitoring the weight changes. The 90 to 250 μm fragments were used in order to provide a narrow particle size distribution. Restricting samples to the same size distribution was a means to maintain relatively similar surface to volume ratios, normalizing its effect upon oxide decomposition.

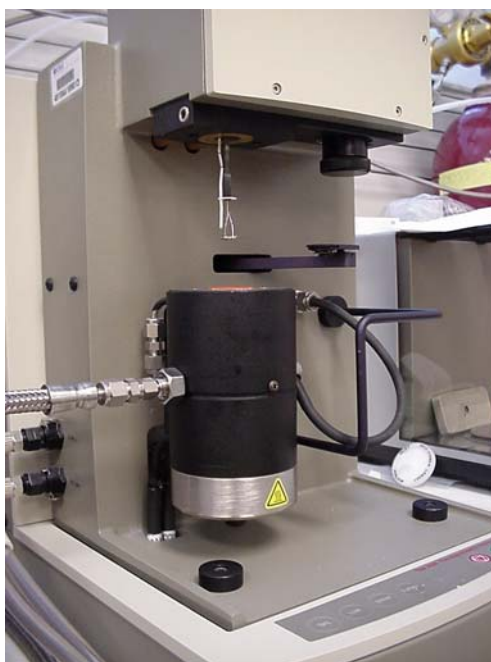


Figure 3-12. TA Instruments TGA 2050 thermogravimetric analyzer.

The appropriate temperatures for isothermal experiments were chosen based on the results from the nonisothermal gravitational analysis for each composition. The isothermal runs were performed using the same gas flow used for the nonisothermal experiments. The length of the isothermal experiments varied for each composition and temperature, as measurements were

terminated after the sample exhibited no further weight change. The ramp-up time (t_0) to reach the designated temperature was between 8 and 15 minutes for all experiments. This period is neglected in the presentation of figures and all calculations. The measured weight gain data are converted to fraction reacted, α , versus time plots for purposes of calculating kinetic parameters. Isotherms for $(U_{0.368}Th_{0.632})O_{2+x}$ were repeated in triplicate to determine the statistical significance of measured data.

Samples were also characterized with x-ray diffraction after oxidation. All $(U,Th)O_{2+x}$ samples were found to be the cubic fluorite structure, demonstrating that there were no bulk phase changes during oxidation for any of the solid solution compositions.

Kinetic Analysis

The measured data from nonisothermal and isothermal dry oxidation of mixed oxides were subjected to standard model-fitting techniques and a model-free method reported by Vyazovkin and Wight [Vya99]. Standard methods estimate kinetic parameters and reaction mechanisms based on theoretical reaction models. Arrhenius parameters from isothermal and nonisothermal data, however, often disagree because of the differing nature of a constant versus variable heating profile. Calculations derived from isothermal data, therefore, are traditionally considered more reliable because the temperature variable is held constant, reducing the number of parameters simultaneously determined by fitting the data using a particular reaction model. Consequently, the macroscopic nature of thermoanalytical techniques does not always elucidate system complexity, such as overlapping mechanism. Additionally, measured data may fit more than one hypothetical reaction model, demonstrating the danger of force-fitting data to inadequate models.

The model-free technique, on the other hand, bypasses assumptions of a specific reaction model. Activation energies instead are determined as a function of the degree of conversion (α) and/or temperature. Instead of yielding a global composite activation energy for the system, the

activation energy dependence on α is capable of revealing process complexities. Vyazovkin and Wight [Vya99] reported the model-free method capable of producing consistent kinetic information from both isothermal and nonisothermal data

Model-fitting method. Traditional kinetic analysis of isothermal data entails a comparison of measured values with theoretical reaction models. These models are derived based on the geometry of interface initiation and advance and/or diffusion processes occurring in the solid. Natural limitations are inherent in translating experimental data into pertinent kinetic parameters based on the models. It is often the case that factors important to yielding an important conclusion regarding kinetic processes may not be experimentally accessible. Because of restrictions experienced in quantitatively characterizing particle morphology in this study and the assumption that pellet fragments were not spherical, developing a particle size dependent term was hindered. It was anticipated that restricting the particle size and, consequently, surface area to a common range in this study would normalize the surface area influence and allow for comparisons between U/Th compositions in this study.

Solid-state decomposition kinetic analysis is based on general kinetic Equation 3-17 and previously mentioned Arrhenius Equation 2-2, where α is the fraction reacted, $f(\alpha)$ is the reaction model, $k(T)$ is the rate coefficient (also denoted k), t is time, A is the frequency factor, E is the activation energy, R is the gas constant, and T is the temperature.

$$(3-17) \quad f(\alpha) = k(T) \cdot t$$

$$(2-2) \quad k(T) = A \exp \left[-\frac{E}{RT} \right]$$

Theoretical relationships, $f(\alpha)$, that have found the greatest application in solid state kinetic analysis are summarized in Table 3-5 [Bam80]. If experimental data is plotted as $f(\alpha)$ vs. t , the linearity of the plot is an indication of how well the data agrees with a particular reaction model. Care must be taken in accurately defining the final yield, $\alpha = 1.0$, to prevent distorting the

α vs. t curve. Rate coefficients, subsequently, are obtained from the linear slope of the $f(\alpha)$ vs. t plot.

Table 3-5. Solid state theoretical reaction models

Reaction model	$f(\alpha)$	Reaction model	$f(\alpha)$
<i>Acceleratory rate equation</i>		<i>Deceleratory rate equations</i>	
Power law	$\alpha^{1/n}$	<i>(Based on diffusion mechanisms)</i>	
Exponential law	$\ln(\alpha)$	One-dimensional diffusion	α^2
<i>Sigmoid rate equations</i>		Two-dimensional diffusion	$(1-\alpha)\ln(1-\alpha) + \alpha$
Avrami-Erofe'ev	$[-\ln(1-\alpha)]^{1/2}$	Three-dimensional diffusion	$[1 - (1-\alpha)^{1/3}]^2$
	$[-\ln(1-\alpha)]^{1/3}$	Ginstling-Brounshtein	$[1 - (2\alpha/3)] - (1-\alpha)^{2/3}$
	$[-\ln(1-\alpha)]^{1/4}$	<i>(Based on geometric models)</i>	
Prout-Tompkins	$\ln[\alpha/(1-\alpha)]$	Contracting area	$1 - (1-\alpha)^{1/2}$
		Contracting volume	$1 - (1-\alpha)^{1/3}$
		<i>(Based on order with respect to α)</i>	
		First order	$-\ln(1-\alpha)$
		Second order	$(1-\alpha)^{-1}$
		Third order	$(1-\alpha)^{-2}$

The equation below is obtained by taking the natural logarithm of the Arrhenius relationship [Ban68]. From Equation 3-18, it is clear that a plot of $\ln[k(T)]$ vs. $1/T$ will give a straight line with slope equal to $-E/R$ and an intercept equal to $\ln A$.

$$(3-18) \quad \ln k(T) = \left[-\frac{E}{R} \right] \left[\frac{1}{T} \right] + \ln A$$

Model-free method. The model-free method was applied solely to isothermal rate data in this study. Under isothermal conditions, the reaction model is assumed to be independent of the heating rate. By rearranging Equation 3-17, substituting into Equation 2-2, and taking the natural logarithm, Equation 3-19 is obtained, where $t_{\alpha,i}$ is the reaction time for a selected fraction reacted, α , for a given isotherm, i .

$$(3-19) \quad -\ln t_{\alpha,i} = -\left[\frac{E}{RT} \right] + \ln \left[\frac{A}{f(\alpha)} \right]$$

A $-\ln(t)$ vs. $1/T$ plot at a particular α value is constructed from the isothermal oxidation data obtained at several temperatures. The linear slope of the $-\ln(t)$ vs. $1/T$ plot yields the value $-E/R$, at the fraction reacted, α , without making any assumptions about the reaction model, $f(\alpha)$.

Because the intercept term in Equation 3-19 is a function of both A and $f(\alpha)$, the frequency factor (A) cannot be determined by this method without identifying $f(\alpha)$. The benefits of this method, however, are such that reaction complexities may be revealed by a dependence of E on α , instead of simply yielding an overall value for the reaction. Consequently, there is a heavy reliance upon meaningful definition of final yield where $\alpha = 1.0$.

CHAPTER 4 RESULTS AND DISCUSSION

Material Synthesis

X-ray diffraction. Bulk homogeneity of the mixed oxides was confirmed by XRD to be cubic fluorite in structure at all U/Th compositions before and after air oxidation. A Philips APD 3720 Diffractometer measured pellet fragments with silicon as a standard. Measured diffraction powder patterns were compared with JCPDS standards to qualitatively confirm Bragg angles (2θ) and identify corresponding miller indices. See Appendix B for details of the diffraction pattern measured for $U_{0.368}Th_{0.632}O_{2+x}$ pellet fragments isothermally oxidized at 400°C in flowing air. All U/Th compositions qualitatively presented the same cubic fluorite diffraction pattern.

Three methods of calculating unit cell parameters were used: method of least squares (LSQ), Cohen's method [Cul78], and Popovic's method [Pop73, Pop85]. Starting compositions of all unoxidized material batches are assumed stoichiometric. Unit cell volume or lattice parameter decreases with respect to increasing percent UO_2 , which is consistent with published findings as presented in Figure 4-1. Table 4-1 summarizes the lattice parameters as calculated by the three methods for isothermally oxidized (U,Th) O_2 pellet fragments. As more of the smaller uranium cation is introduced into the thorium oxide matrix, it is apparent that the lattice shrinks to accommodate without changing the cubic fluorite structure.

Table 4-1. Calculated (U,Th) O_2 oxidized lattice parameters by three methods

Description	LSQ ($\cos^2\theta$)	LSQ ($\cos^2\theta/\sin\theta$)	Cohen's	Popovic
$U_{0.236}Th_{0.764}O_2$	5.568 ± 0.003	5.564 ± 0.002	5.563 ± 0.001	5.564 ± 0.005
$U_{0.368}Th_{0.632}O_2$	5.542 ± 0.002	5.543 ± 0.001	5.543 ± 0.001	5.541 ± 0.003
$U_{0.500}Th_{0.500}O_2$	5.523 ± 0.004	5.522 ± 0.003	5.523 ± 0.002	5.525 ± 0.002

LSQ: least squares method uses two functions for diffractometer measured patterns.

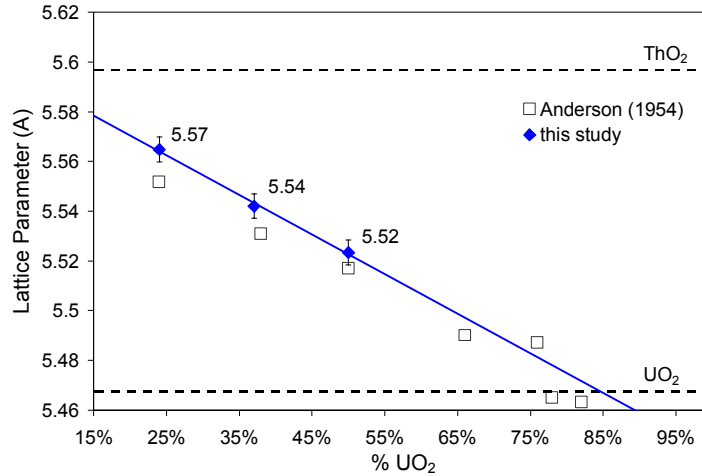


Figure 4-1. Lattice parameter evolution with respect to UO_2 content. Dashed lines indicate the lattice parameters for reference oxides ThO_2 and UO_2 . Linear trendline show that results from this study are in agreement with Anderson et al. (1954)

Inductively coupled plasma Auger electron spectrometer. Samples of $(\text{U,Th})\text{O}_2$ synthesized by the oxalate and ammonium hydroxide pathways were measured by James Jerden, Ph.D. at Argonne National Laboratory to obtain weight percent uranium and thorium. Assuming whatever remained was oxygen, those results, as summarized in Table 4-2 as weight percent, it was apparent something other than oxygen was also present. As a consequence, carbon analysis was pursued to determine whether the excess could be attributed to residual carbon from the synthesis process.

Carbon analyzer. A tungsten carbide standard (0.26 ± 0.02 g) was measured five times with a standard deviation of 0.03% by weight carbon. An empty crucible established a blank measured carbon concentration of 0.00385% by weight. Absolute and relative uncertainty were calculated to be $\{(0.03)^2 + (0.03)^2\} = 0.04$ and $(0.04/\text{measurement} \times 100\%)$, respectively [Har91]. Oxalate and ADU synthesized $(\text{U,Th})\text{O}_2$ samples with nominal percent U content of 20%, 35%, and 50% measured results are summarized in Table 4-2 as weight percent. Since it was supposed the excess identified by ICP-MS was residual carbon from the oxalate process, the ADU synthesized nominal 20% UO_2 sample was not measured by this instrument.

From the above results, it is apparent the elemental analysis techniques used were unable to fully identify the chemical composition of wet synthesized (U,Th)O₂ materials. Ando et al. [And76, And84] also noted the presence of impurities for ThO₂ synthesis by sol-gel and arc fusion techniques. Without a full chemical identification, the possible influence of unknown impurities could possibly inhibit evaluation of the thorium oxide matrix effect upon uranium oxidation. As a consequence, wet chemistry synthesis techniques were abandoned in favor of traditional powder process methods to avoid introduction of impurities associated with the synthesis path.

Table 4-2. ICP-AES and LECO carbon analysis results and calculated metal valence of wet synthesized (U_yTh_{1-y})O_{2+x} indicate impurities must be present.

Sample (Nominal composition)	U wt %	Th wt %	C wt %	Balance*	y	x*	V _M *
ADU (U _{0.20} Th _{0.80})O _{2+x}	15.8	66.6	--	17.6	0.192	1.11	6.22
Oxalate (U _{0.20} Th _{0.80})O _{2+x}	11.6	70.9	0.01	17.5	0.141	1.09	6.18
Oxalate (U _{0.35} Th _{0.65})O _{2+x}	21.3	54.1	0.17	24.4	0.283	2.72	9.44
Oxalate (U _{0.50} Th _{0.50})O _{2+x}	32.7	38.0	0.19	29.1	0.463	4.03	12.06

*Assumes balance is only oxygen. Metal valences (V_M) calculated from x are impossible; knowing that V_{Th} maximum is +4 and V_U is 6.

Thermogravimetry

Nonisothermal. Thermal gravimetric analysis curves for air oxidation of UO₂ and (U,Th)O₂ samples under nonisothermal conditions are shown in Figures 4-2 through 4-5 as percent weight gain vs. temperature. All of the data exhibited single-step behavior, including the data for UO₂ (Figure 4-5). This is consistent with observations of air oxidation of (U_yTh_{1-y})O₂ materials (y = 0.15, 0.30, 0.72, 0.77) performed by Anthonysamy et al. [Ant00] While gravimetric oxidation curves for UO₂ often exhibit a two-step behavior corresponding to oxidation from UO₂ to U₃O₇ to U₃O₈, the absence of a well defined two-step curve for UO₂ in this study is most likely the result of the low specific surface area of the samples (0.01 to 0.02 m²/g). With the lower surface area of coarser particle size distributions, the fast surface transformation of UO₂ to U₃O₇ contributes less to the overall weight gain because the reaction interface decreases. The first “step”, therefore, diminishes with decreasing surface area. The slower bulk

transformations of UO_2 to U_3O_8 and U_3O_7 to U_3O_8 , however, are less dependent upon surface area. The second “step” remains despite particle size distribution. Thermogravimetric measurements of higher surface area UO_2 powders (1 to 3 m^2/g) resulted in the expected two-step weight gain curve. Thus, the low surface to volume ratio of the 90 to 250 mm pellet fragments impacted the results such that bulk reactions had a much larger effect on the overall oxidation process than the contributions from surface reactions. Figures 4-2 to 4-4 show the mixed (U,Th) O_2 oxides and Figure 4-5 UO_2 fragments under nonisothermal air oxidation at heating rates of 1, 3, 5°C/min as indicated.

A weight decrease of (U,Th) O_2 samples at higher temperatures (Figures 4-2 to 4-4) was observed. The UO_2 isothermal sample, Figure 4-5, however, did not present this same behavior. The mixed (U,Th) O_2 oxide weight loss at the higher temperature region was constant and sustained for > 20 minutes. Since the TGA was located on an isolation table and weight loss was not sudden, it was not supposed that fragments were somehow ejected from the pan from an external source. To eliminate the presence of an unknown gas, the pellet fragments, furnace chamber, and gas lines were vacuum purged and backfilled with high purity Argon gas three times at room temperature. A final vacuum purge was backfilled with air prior to beginning each run. These same measures were taken with the nonisothermal oxidation of UO_2 pellet fragments. Those results are presented in Figures 4-2 to 4-5. For the UO_2 sample, the absence of a steady weight decrease following initial weight gain further suggests an external source is unlikely. Further, without measurements beyond 900°C, it is unknown whether the mixed oxide weight would eventually reach a steady state.

Knowing the lattice structure evolution from start to finish may confirm what mechanisms influence oxidation. Though not accomplished in this study, XRD measurements of (U,Th) O_2 fragments at various stages of nonisothermal oxidation, particularly at the peak maximum and $T = 900^\circ\text{C}$, may suggest a possible explanation. Possibly, the thoria lattice

initially accommodates excess anions in the large octahedral interstitial sites, with charge neutrality maintained by increasing U valency. Successively more anions, noting peak weight gains of $U_{0.236}Th_{0.464}O_2$ (0.76% – 0.77%), $U_{0.368}Th_{0.632}O_2$ (1.16 – 1.26%), and $U_{0.500}Th_{0.500}O_2$ (1.59 – 1.65%), are accommodated with increasing U content. Eventually, the lattice may become “supersaturated”, holding the maximum number of anions with U at its highest valency, yielding a peak maximum. Perhaps, with increasing thermal energy, the structural and energetic strain of maintaining this “supersaturated” lattice causes the steady ejection of excess anions until a stable, unstrained configuration is achieved. This may account for the decreasing weight.

Nonisothermal measurements of finer particle size distributions may also yield surface area dependent or other mechanisms that would clarify the peak maximum and subsequent decreasing weight in the (U,Th) O_2 systems. Like UO_2 , there may be “fast” and “slow” competing mechanisms. A “fast” mechanism may dominate the weight gain at lower temperatures. At the higher temperatures, this “fast” mechanism may have reached completion and the “slow” mechanism becomes the rate-limiting step.

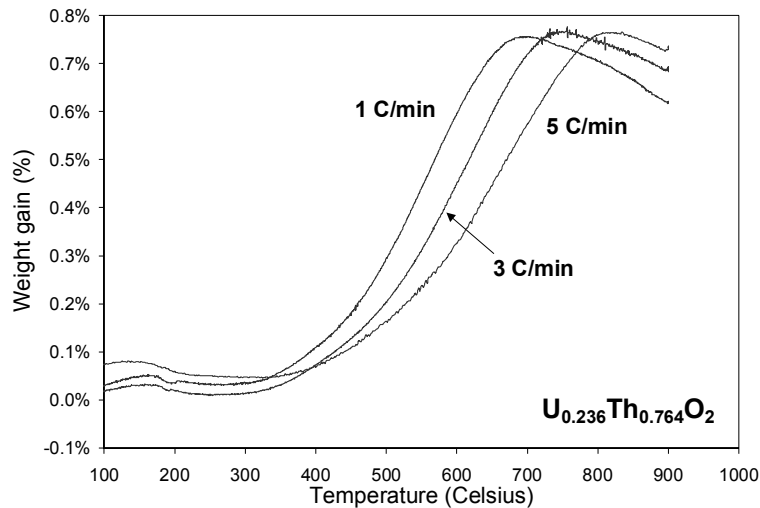


Figure 4-2. Nonisothermal ($U_{0.236}Th_{0.764}$) O_2 oxidation TGA data at heating rates of 1, 3, and 5°C/min.

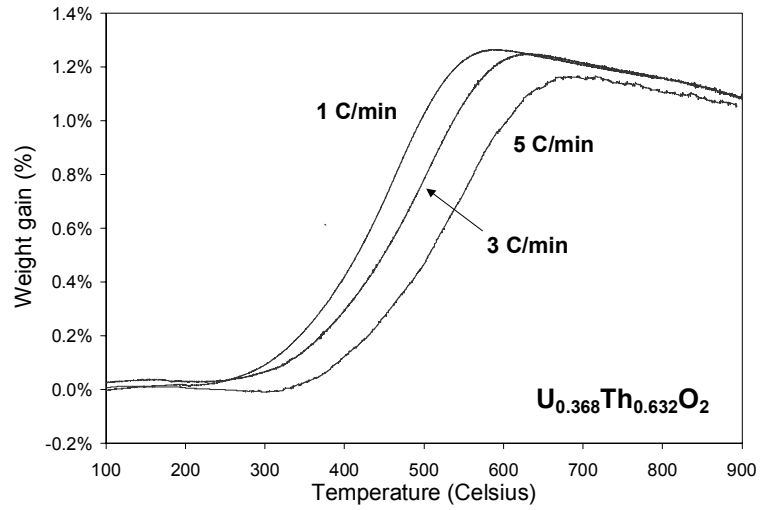


Figure 4-3. Nonisothermal ($U_{0.368}Th_{0.632}$) O_2 oxidation TGA data at heating rates of 1, 3, and 5°C/min.

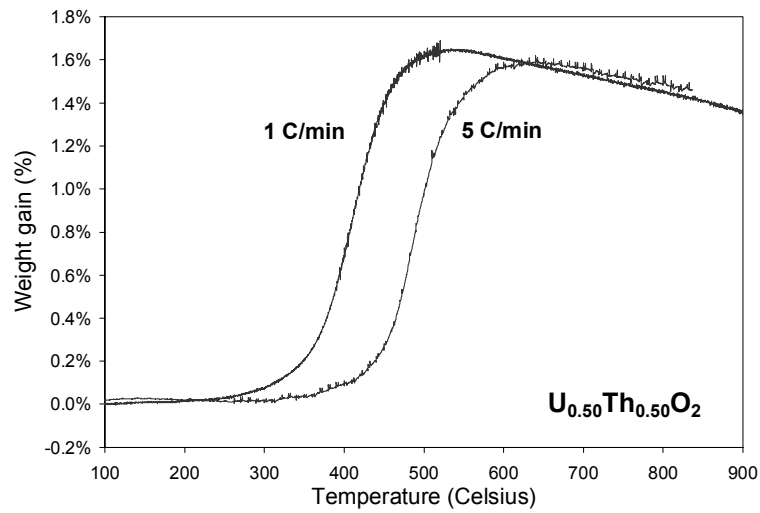


Figure 4-4. Nonisothermal ($U_{0.50}Th_{0.50}$) O_2 oxidation TGA data at heating rates of 1 and 5°C/min.

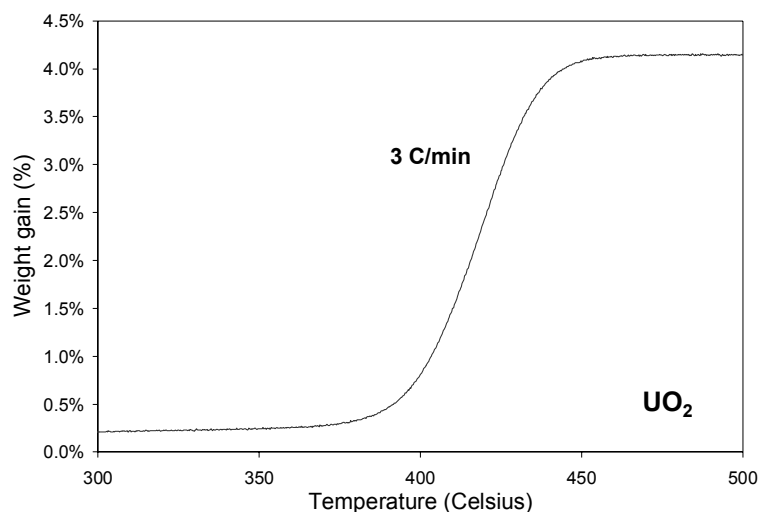


Figure 4-5. Nonisothermal UO_2 oxidation TGA data at heating rate of $3^\circ\text{C}/\text{min}$.

Isothermal. The appropriate temperatures for isothermal gravitational analysis experiments were chosen based on the nonisothermal results in Figures 4-2 to 4-5. Generally, temperatures were chosen to encompass the region of the curves where the majority of the weight gain occurred. The results from isothermal gravitational analysis at the selected temperatures is presented as fraction reacted, α , versus time, $t - t_0$, (Figures 4-6 to 4-9) where t_0 is the time required to reach the desired isothermal temperature (between 8–15 minutes). Some oxidative weight gain did occur during this ramp-up period. Because the time required to achieve complete reaction for the (U,Th) O_2 samples was large (usually more than 1000 minutes), the weight gain during the same ramp-up period was negligible compared to the overall weight gain. Isothermal oxidation of the UO_2 samples, however, was completed in 20 to 120 minutes, depending on the temperature. Contributions to overall weight gain during the ramp period for UO_2 , therefore, were often significant and resulted in errors in the calculation of the true degree of completion, α . This, in turn, affected the α vs. $t - t_0$ curve shapes in Figures 4-6 to 4-9. Consequently, the curve distortion hindered reaction model identification by model-fitting methods as well as accurate measurement by the α -dependent model-free method.

At successively higher isothermal temperatures, (U,Th)O₂ rate of oxidation was expected to increase, such that the slope systematically became steeper before reaching steady state. This did not occur in U_{0.5}Th_{0.5}O₂ (Figure 4-8) and UO₂ (Figure 4-9). Additionally, the instrument was jarred during the 375°C run of UO₂, which accounts for the discontinuity at 60 minutes in Figure 4-9. With the exception of U_{0.368}Th_{0.632}O₂ (Figure 4-7), which was measured in triplicate, only single runs at all isotherms were performed. Slope irregularities, therefore, may be a consequence of experimental scatter.

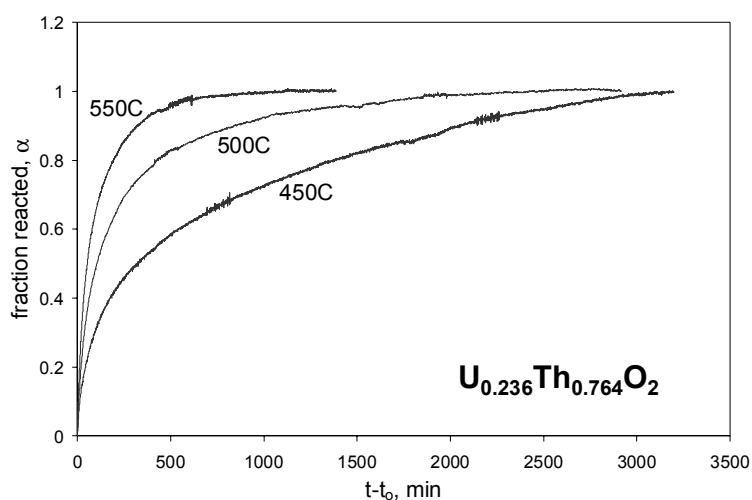


Figure 4-6. Isothermal oxidation TGA data for (U_{0.236}Th_{0.764})O₂ fragments (90 – 250 μm). Percent weight gain data is converted to fraction reacted, α .

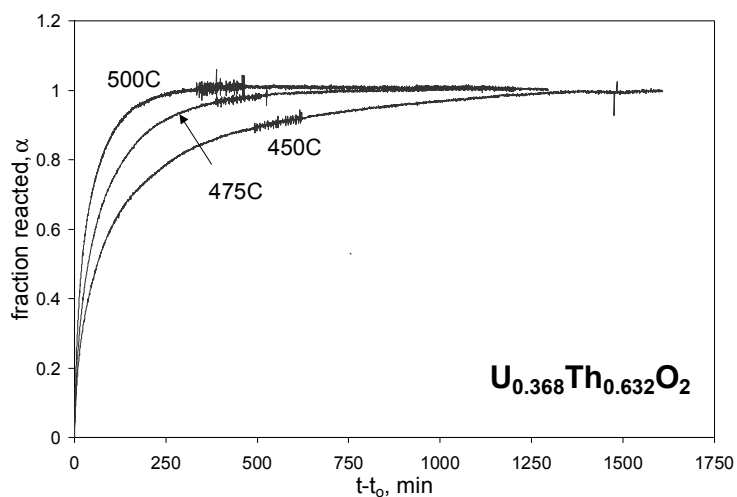


Figure 4-7. Isothermal oxidation TGA data for (U_{0.368}Th_{0.632})O₂ fragments (90 – 250 μm). Percent weight gain data is converted to fraction reacted, α .

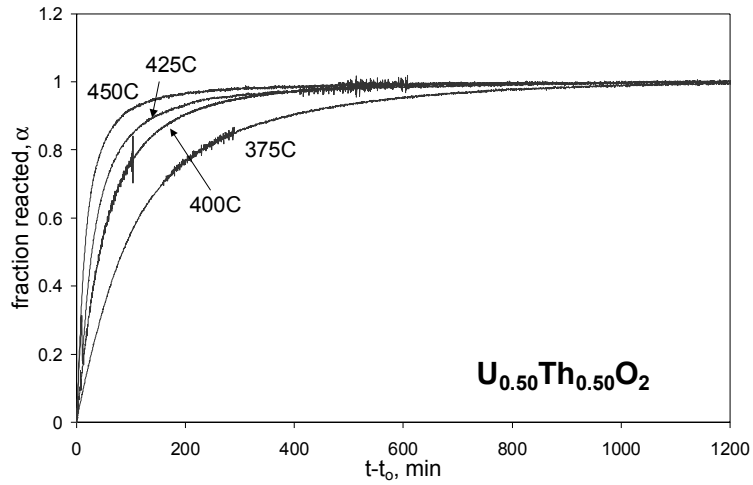


Figure 4-8. Isothermal oxidation TGA data for $(U_{0.50}Th_{0.50})O_2$ fragments (90 – 250 μm). Percent weight gain data is converted to fraction reacted, α .

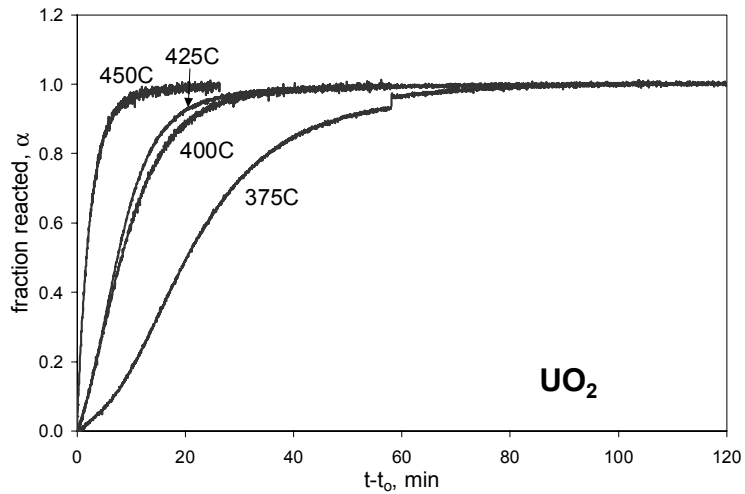


Figure 4-9. Isothermal oxidation TGA data for UO_2 fragments (90 – 250 μm). Percent weight gain data converted to fraction reacted, α .

Cation valence. Based on the final weight gain of each sample after isothermal air oxidation, the mean uranium valence was calculated. For the calculation, thorium is assumed to maintain a valence of +4. The weight gain is entirely attributed to excess oxygen, which is used to determine the valence of uranium cations. The initial O/U ratio of the samples was assumed to be 2. The mean uranium valence (V_U) was calculated from the weight gain data using Equations 4-1 and 4-2, where the variable x and y are taken from the formula $(U_yTh_{1-y})O_{2+x}$, m_1 is the initial mass of the sample, Δm is the weight change after oxidation, and the value in parentheses in Equation 4-2 is the formula weight of the starting material, $((U_yTh_{1-y})O_{2+x})$.

$$(4-1) \quad V_U = 4 + \frac{2x}{y}$$

$$(4-2) \quad x = \frac{\Delta m}{m_1} \left[\frac{(264.04 + 5.99y)}{16} \right]$$

Results are plotted in Figure 4-10. Dashed lines indicate the mean uranium valence for the reference oxides U_3O_7 and U_3O_8 . As indicated in the figure, none of the mixed oxides reached the same degree of oxidation as UO_2 , based on the mean uranium valence calculations. Knowing the oxidized lattices are still cubic fluorite and uranium valences are increasing, it stands to reason that the lattices are accommodating sufficient excess oxygen anions to maintain charge neutrality with the U cations. So, instead of a phase transformation, anions may be packed into interstitial sites near uranium cations, since thorium valency is a constant +4. Assuming a homogeneous distribution of U and Th cations, oxygen accommodation may be a predominantly bulk mechanism. Without confirmation of the surface composition, a surface-dependent reaction cannot be rejected.

This would support the view that ThO_2 inhibits uranium from oxidizing further by inhibiting the supply of oxygen with the decreased anion mobility in the thorium matrix. Published activation energies (Appendix A) of intrinsic oxygen anion diffusion in ThO_2 (209 to 275 kJ/mol) and UO_2 (237 to 273 kJ/mol) indicate that stoichiometric UO_2 values are comparable

to those for ThO_2 . Uranium dioxide, however, is typically hyper-stoichiometric because of the ease in which it incorporates excess oxygen into the lattice structure. Activation energies reported for UO_{2+x} are 87 to 124 kJ/mol, which is significantly lower than both stoichiometric ThO_2 and UO_2 , indicating the greater ease in which O diffuses into the lattice. The broad range and variety of sample preparation and measurement conditions may account for the breadth of published values reported. It stands to reason that activation energies calculated for mixed (U,Th) O_2 oxides would fall between those reported for stoichiometric ThO_2 and hyperstoichiometric UO_{2+x} . The presence of U cations in the ThO_2 is expected to lower the threshold for oxygen anion mobility and accommodation in the lattice. It is anticipated the ThO_2 matrix, on the other hand, will limit the anion supply such that cations are unable to attain U maximum valence state.

Secondary electron microscope images taken of pellet surfaces by J. Jerden at ANL (Appendix C) confirmed the pellets are polycrystalline. Jerden reported grain sizes ranging from 4 to 20 μm on unbroken surfaces of 5% UO_2 and 20% UO_2 co-milled pellets. An image of the broken surface of a 20% UO_2 co-milled pellet shows curious “gas bubble” features. No images were obtained of pellet fragments. Despite no images of the pellet fragments, it is obvious that grain boundaries are present and would have an extrinsic effect upon oxygen mobility. In fact, anions may assemble more easily in the grain boundaries than interstitial sites. Anion migration along grain boundaries, consequently, may yield lower oxidation activation energies than for single crystal systems. Undoubtedly, activation energies calculated for this polycrystalline system would encompass intrinsic and extrinsic mechanisms. Without quantitative measurements of pellet fragment grain sizes and boundaries, an extrinsic term cannot be developed for the model-fitting kinetic analysis. The “gas bubble” features, also, indicate other extrinsic processes may also be at work. Consequently, the models used in this research are limited without more complete characterization of the pellet fragments to account for the intrinsic and extrinsic contributions.

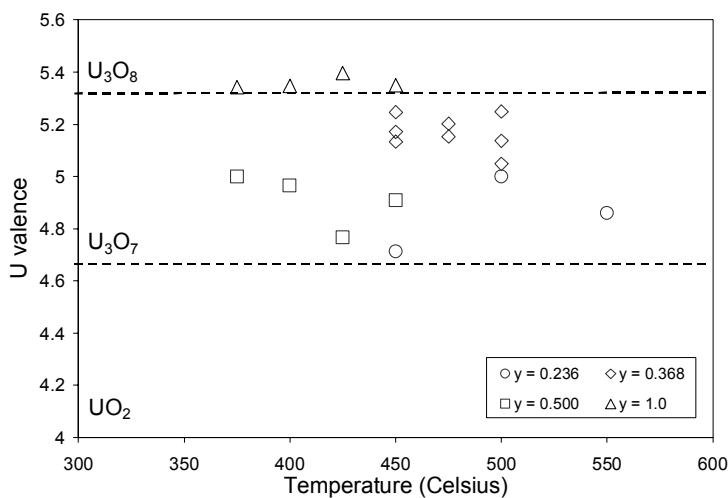


Figure 4-10. Mean uranium valence for isothermally oxidized $(U_yTh_{1-y})O_2$ and UO_2 . Dashed lines indicate the mean uranium valence for the reference oxides U_3O_8 , U_3O_7 , and UO_2 .

Kinetic Analysis

Isothermal rate data were inserted into the reaction models, $f(\alpha)$, from Table 3-5. Linear behavior of $f(\alpha)$ -time plots would suggest overall agreement with the theoretical model. Although model fitting is the conventional technique for kinetic analysis, the published theoretical reaction models do not necessarily account for all variables that may have influence on the proposed mechanisms. For instance, systems that exhibit a surface-dependent reaction, such as the $UO_2 \rightarrow U_3O_7$ “fast” transformation, require an additional term to allow for particle size and shape variations. It has already been noted that surface area has an impact on the measured signal for UO_2 oxidation. The $(U,Th)O_2$ mixed oxide compositions may likely demonstrate a similar consequence. The reaction models used in this study, however, do not take into account particle size distribution (i.e., surface area). Considering the absence of particle morphology data to develop a particle geometry and/or surface area term, conclusions drawn from the reaction models in agreement with the measured data are restricted.

Since the temperature is held constant for the isothermal runs, time is the only dependent variable. Isothermal data, therefore, are typically assumed more reliable for calculating kinetic

parameters than nonisothermal data, where time and temperature vary simultaneously. In the subsequent figures, linear agreement to 2D diffusion, 3D diffusion, and/or Avrami-Erofe'ev reaction models is shown for isothermal data. Rate coefficients (k) are obtained from the slopes of the best-fit linear trendlines.

Mixed Oxide ($U_{0.236}Th_{0.764}O_2$)

Transformed into degree of conversion, α , measured isothermal rate data of ($U_{0.236}Th_{0.764}O_2$) were inserted into reaction models, $f(\alpha)$, summarized in Table 3-5. The two-dimensional and three-dimensional diffusion models, where $f(\alpha) = (1-\alpha)\ln(1-\alpha) + \alpha$ and $f(\alpha) = [1 - (1-\alpha)^{1/3}]^2$, respectively, displayed agreement. Reaction models were plotted against $t-t_0$, which truncates the initial t_0 ramp-up stage.

Model-fitting suggests two dimensional diffusion $\leq 450^\circ\text{C}$ (Figure 4-11), followed by a shift to three dimensional diffusion at temperatures greater than 500°C (Figures 4-12 through 4-13). Table 4-3 summarizes the rate coefficients and linear fit of both 2D and 3D diffusion reaction models, which were used to construct an Arrhenius plot (Figure 4-27) with E and $\ln(A)$ calculated to be 62.1 ± 17.9 kJ/mol and 1.71 ± 2.87 , respectively.

Linear agreement of nonisothermal rate data was also tested with the diffusion reaction models identified by isothermal data. Measured data were converted to rate coefficient (k) by the relation $k = f(\alpha)/t$, according to Equations 2-2, 3-17, and 3-18. Arrhenius $\log(k)$ vs $1/T$ plots were constructed with $f(\alpha)$ for 2D and 3D diffusion models shown in Figures 4-15 to 4-17 for heating rates 1, 3, and $5^\circ\text{C}/\text{min}$ to 900°C . Both reaction models displayed linear behavior with high correlation values in the region of interest. It was not discernable which diffusion model would be appropriate. Like the isothermal data, slopes and intercepts from linear fit yield corresponding E and A values shown in Table 4-4.

The model-free technique was used to compare with values calculated by model-fitting, particularly since there is poor agreement between isothermal ($E = 62.1$ kJ/mol) and

nonisothermal ($E = 92$ to 94 kJ/mol) results. The model-free method was applied solely to the isothermal rate data in this study, as shown in Figure 4-18. Reaction times at selected α ($= 0.4, 0.5, 0.6$) were arranged into a $-\ln(t)$ vs. $1/T$ plot based on the relationship described in Equation 3-19. Frequency factors cannot be determined by this method without identifying $f(\alpha)$. Since neither the 2D or 3D diffusion reaction models could be discerned by isothermal and nonisothermal model fitting, frequency factor calculations were not performed by the model-free method.

Activation energies calculated from the slope yield values of 79.2 ± 6.9 kJ/mol, 87.6 ± 7.6 kJ/mol, and 94.1 ± 7.7 kJ/mol for fraction reacted 0.4, 0.5, and 0.6 respectively. These values are more in agreement with those obtained by nonisothermal model-fitting, supporting diffusion as the primary mechanism of oxidation.

Table 4-3. Rate coefficients of isothermal ($U_{0.236}Th_{0.764}$)O₂ agreement to diffusion models

Isothermal temperature	2D Diffusion		3D Diffusion	
	k (min ⁻¹)	R ²	k (min ⁻¹)	R ²
450°C	3×10^{-4}	0.9969	2.0×10^{-4}	0.9330
500°C	3×10^{-4}	0.8823	2.9×10^{-4}	0.9871
550°C	8×10^{-4}	0.8365	7.1×10^{-4}	0.9807

Table 4-4. Kinetic results for nonisothermal ($U_{0.236}Th_{0.764}$)O₂ agreement to diffusion models

Nonisothermal	ln(A) (min ⁻¹)	2D Diffusion		3D Diffusion		
		E (kJ/mol)	R ²	ln(A) (min ⁻¹)	E (kJ/mol)	R ²
1°C/min	4.63	81.2	0.9888	5.48	94.4	0.9978
3°C/min	4.36	77.7	0.9946	5.27	92.2	0.9982
5°C/min	4.83	81.6	0.9953	5.06	92.2	0.9971

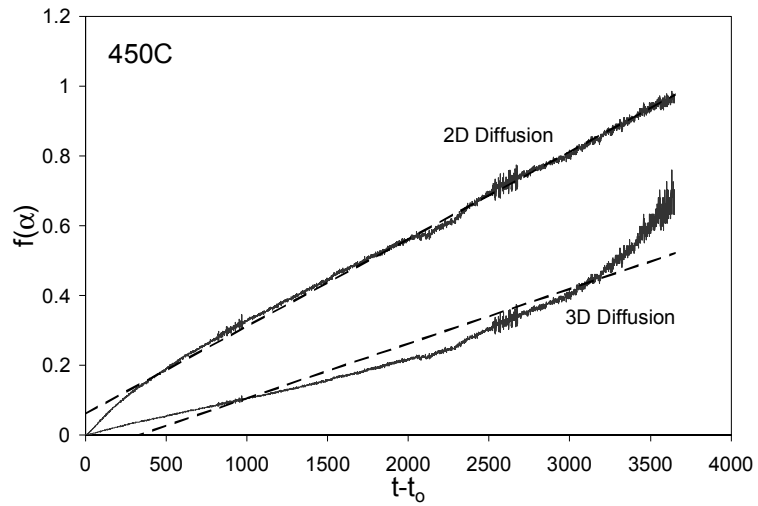


Figure 4-11. Isotherm at 450°C of $(U_{0.236}Th_{0.764})O_2$ oxidation fit to 2D and 3D Diffusion models. Linear correlation values (R^2) are 0.9969 and 0.933, respectively

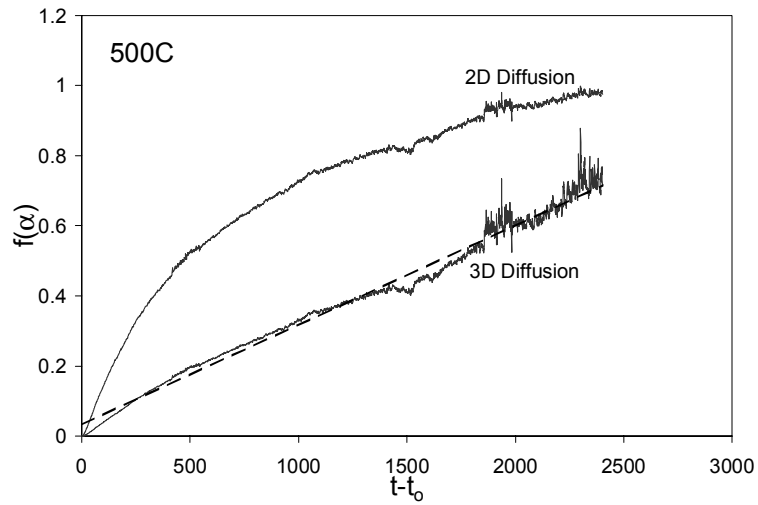


Figure 4-12. Isotherm at 500°C of $(U_{0.236}Th_{0.764})O_2$ oxidation fit to 2D and 3D Diffusion models. Linear correlation values (R^2) are 0.8823 and 0.9871, respectively.

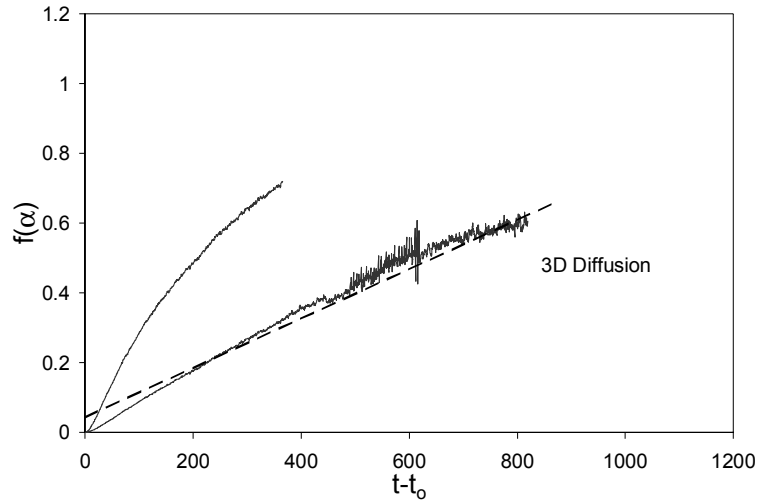


Figure 4-13. Isotherm at 550°C of $(U_{0.236}Th_{0.764})O_2$ oxidation fit to 2D and 3D Diffusion models. Linear correlation values (R^2) are 0.8365 and 0.9807, respectively.

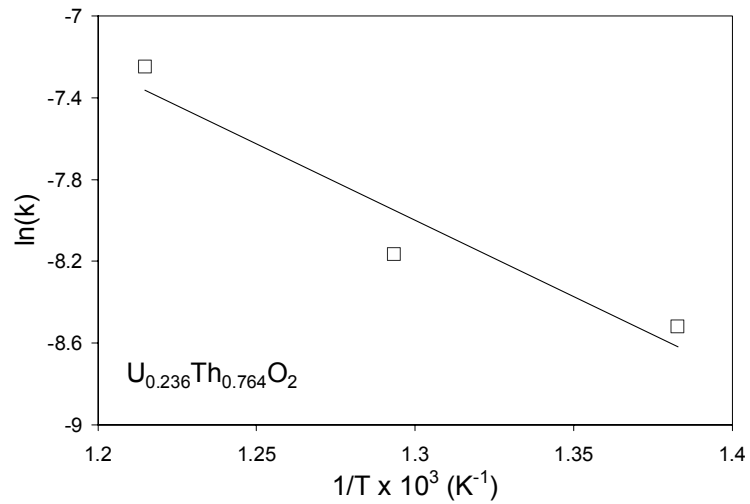


Figure 4-14. Arrhenius plot of $(U_{0.236}Th_{0.764})O_2$ isotherms fit to 3D Diffusion models. Rate constants (k) were determined by fitting gravimetric oxidation data with the 3D diffusion reaction model

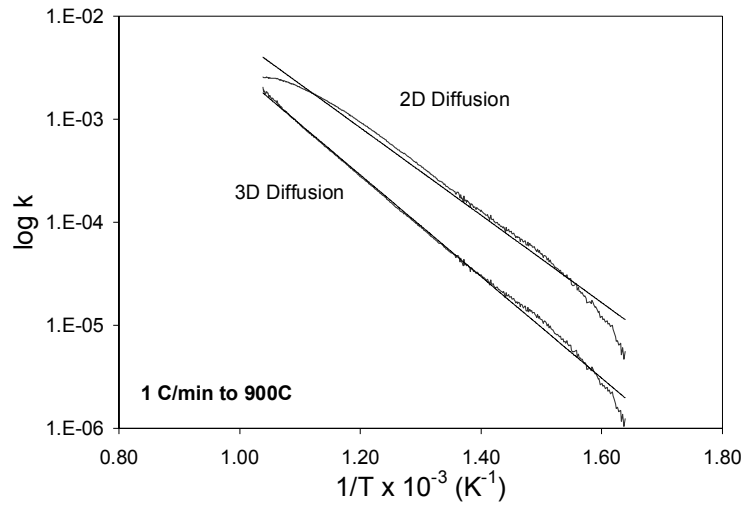


Figure 4-15. Nonisotherm at $1^\circ\text{C}/\text{min}$ ($\text{U}_{0.236}\text{Th}_{0.764}\text{O}_2$) Arrhenius plot fit to 2D and 3D diffusion models. Linear trendlines shown.

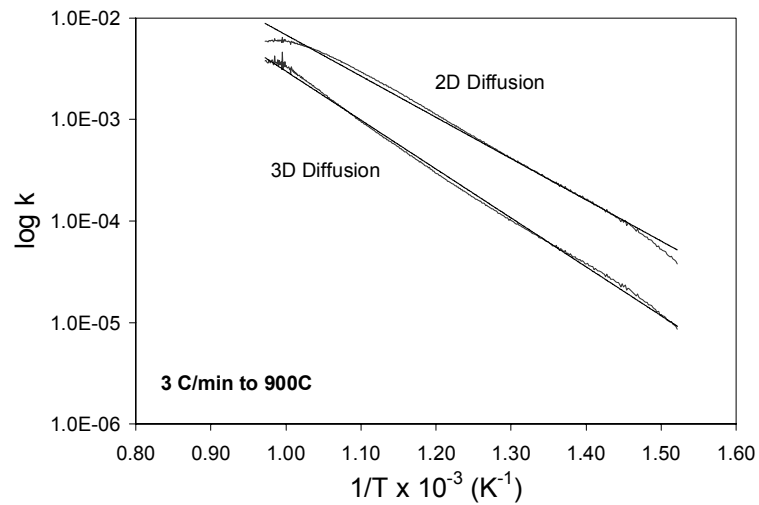


Figure 4-16. Nonisotherm at $3^\circ\text{C}/\text{min}$ ($\text{U}_{0.236}\text{Th}_{0.764}\text{O}_2$) Arrhenius plot fit to 2D and 3D diffusion models. Linear trendlines shown.

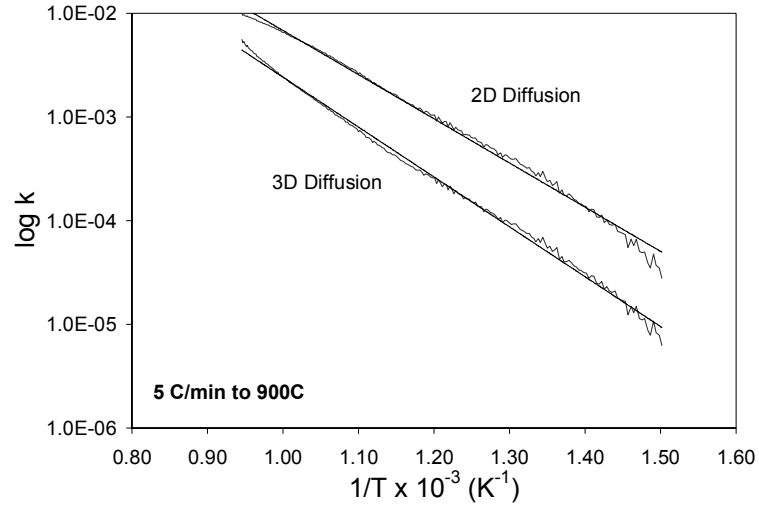


Figure 4-17. Nonisotherm at $5^\circ\text{C}/\text{min}$ ($\text{U}_{0.236}\text{Th}_{0.764}\text{O}_2$) Arrhenius plot fit to 2D and 3D diffusion models. Linear trendlines shown.

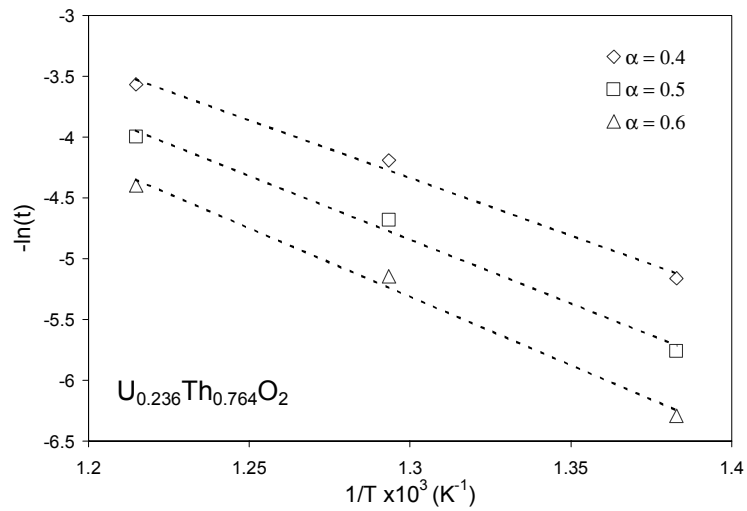


Figure 4-18. Model free ($\text{U}_{0.236}\text{Th}_{0.764}\text{O}_2$) isotherms plotted at $\alpha = 0.4, 0.5, 0.6$. Slope of the linear trendlines gives $-E/R$.

Mixed Oxide ($U_{0.368}Th_{0.632}O_2$)

The same protocol as described in the previous section was applied to ($U_{0.368}Th_{0.632}O_2$), which was isothermally measured in triplicate at 450°C, 475°C, and 500°C. Unlike the other (U,Th) O_2 mixed oxides and UO_2 , ($U_{0.368}Th_{0.632}O_2$) isothermal runs were done in triplicate to establish statistical significance and error analysis for the calculated kinetic parameters. Isothermal rate data were inserted into reaction models from Table 3-5. Those that showed nonlinear behavior were rejected, leaving only the 3D diffusion model. Figures 4-19 to 4-21 show the three sets of isothermal rate data per temperature fit to the 3D diffusion reaction model and the associated linear trendlines. Rate coefficients (k) obtained from the slopes of the $f(\alpha)$ vs. time plots are compiled into a $\ln(k)$ vs. $1/T$ Arrhenius curve. Activation energy and frequency factor are calculated. One 475°C isothermal run (labeled “iso475” in Figure 4-20), however, was discarded because, after reaching a maximum weight gain, the sample began to inexplicably lose weight. Although this run is included in Figure 4-20, it is not incorporated into any kinetic analysis methods. Additionally, scatter was observed in the measured signal at increasingly long dwell times (i.e., greater than 1000 min).

The rate coefficients obtained from the linear slope are detailed in Table 4-5 and assembled into an Arrhenius $\ln(k)$ vs. $1/T$ plot (Figure 4-22) to determine the activation energy and frequency factor for isothermal data. The slope of the linear trendline yielded activation energy and frequency factor of 171 ± 8 kJ/mol and 20.8 ± 1.3 , respectively. These values are significantly greater than those determined for isothermal model-fit ($U_{0.236}Th_{0.764}O_2$). This would seem to indicate that increasing U content results in an increased threshold to oxidation. The higher frequency factor also suggests there are more events occurring in the higher U content mixed oxide. This, however, is contradictory to the premise that increasingly uranium-rich oxides more readily oxidize than thorium-rich compositions. That ($U_{0.236}Th_{0.764}O_2$) isothermal data agreed with 2D and 3D diffusion models, whereas only 3D diffusion was identified for

$(U_{0.368}Th_{0.632})O_2$, may allude to a possible explanation. If diffusion occurs at the surface (2D) and bulk (3D), it is possible that one takes place more readily than the other. Without a particle and/or grain size term included in the reaction model, the plots generated in this study cannot verify whether activation energies calculated reflect whether either system is dominated by surface or bulk reactions or by temperature. The sensitivity to changes in solid-gas and/or grain-grain surfaces is also unknown without an interface-dependent term in the reaction model.

Linear agreement of nonisothermal rate data to the 3D diffusion reaction model is shown in Figure 4-23. Activation energy and frequency factor were calculated from the slopes and intercepts of linear trendlines. They are summarized in Table 4-6. As with $(U_{0.236}Th_{0.764})O_2$, nonisothermal results are significantly different from those for isothermal runs. Nonisothermal and isothermal data appear to support 3D diffusion as the most likely mechanism of oxidation. Values obtained are similar to those for $(U_{0.236}Th_{0.764})O_2$. Again, the absence of terms to account for particle size and grain sizes casts a shadow on these results. The addition of time as a variable brings more complexity to the calculated results than the solely temperature-dependent isothermal measurements.

Model-free plots of $(U_{0.368}Th_{0.632})O_2$ isotherms yielded linear behavior within the investigated temperature range. There was no indication either by model-fitting or model-free methods of a multi-step process. This, of course, does not eliminate the possibility of overlapping mechanisms, but is not suggested in these findings. Figure 4-24 summarizes the model-free results.

Activation energies calculated from the slopes yield values of 103 ± 20 kJ/mol, 105 ± 17 kJ/mol, and 111 ± 16 kJ/mol for degree of conversion 0.4, 0.5, and 0.6 respectively. Unlike $(U_{0.236}Th_{0.764})O_2$, nonisothermal model-fit and model-free calculated activation energies are similar. The isothermally model-fit values, however, are significantly higher. This, again,

appears to be the nature associated with model-fitting isothermal versus nonisothermal rate data.

Both techniques, however, do not disclose a multi-step process.

Table 4-5. Rate coefficient of isothermal ($U_{0.368}Th_{0.632}$)O₂ agreement to 3D diffusion model

Isothermal temperature	k (min ⁻¹)	R ²
450°C	3.90×10 ⁻⁴	0.894
	4.83×10 ⁻⁴	0.932
	4.27×10 ⁻⁴	0.984
475°C	1.17×10 ⁻³	0.965
	9.35×10 ⁻⁴	0.974
500°C	2.72×10 ⁻³	0.989
	2.98×10 ⁻³	0.989
	2.53×10 ⁻³	0.983

Table 4-6. Kinetic results for nonisothermal ($U_{0.368}Th_{0.632}$)O₂ agreement to 3D diffusion model

Nonisothermal	ln(A) (min ⁻¹)	3D Diffusion	
		E (kJ/mol)	R ²
1°C/min	6.48	92.3	0.999
3°C/min	6.80	92.5	0.999
5°C/min	8.63	108.2	0.999

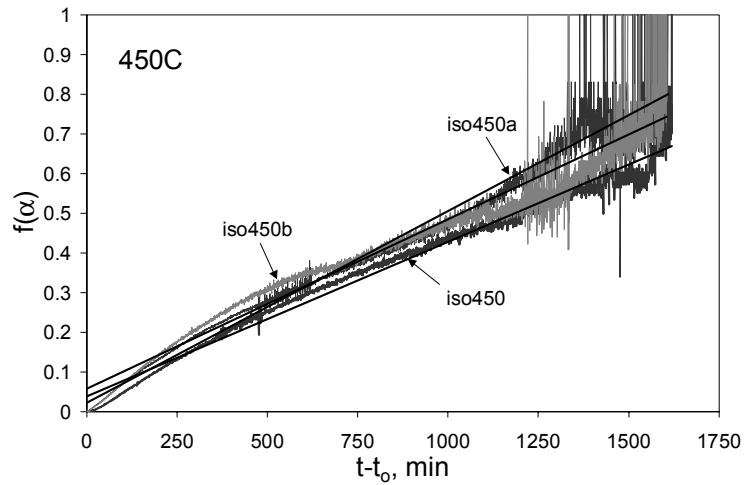


Figure 4-19. Isotherm at 450°C for ($U_{0.368}Th_{0.632}$)O₂ oxidation fit to 3D Diffusion reaction model. Three runs measured.

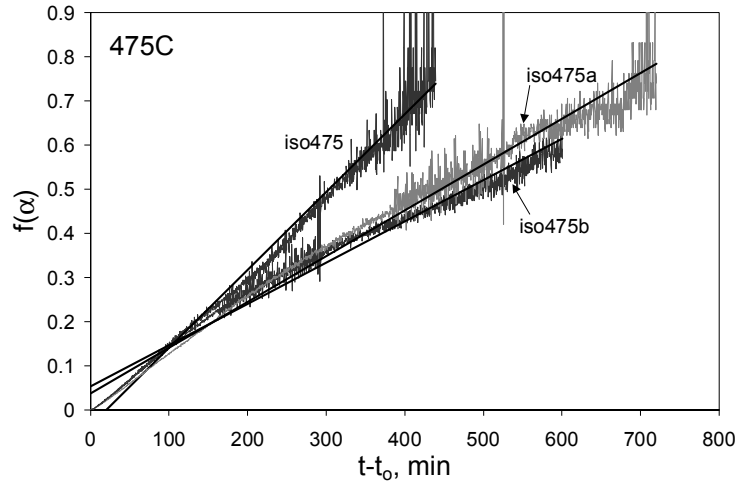


Figure 4-20. Isotherm at 475°C for $(U_{0.368}Th_{0.632})O_2$ oxidation fit to 3D Diffusion reaction model. Run labeled “iso475” is later discarded.

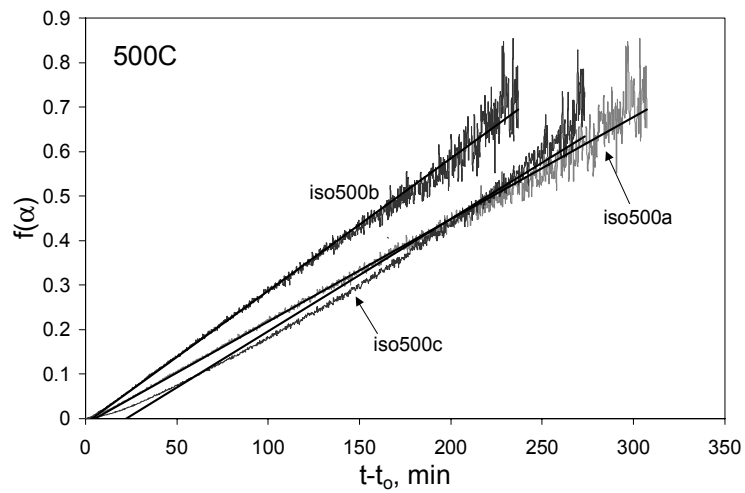


Figure 4-21. Isotherm at 500°C for $(U_{0.368}Th_{0.632})O_2$ oxidation fit to 3D Diffusion reaction model. Three runs measured

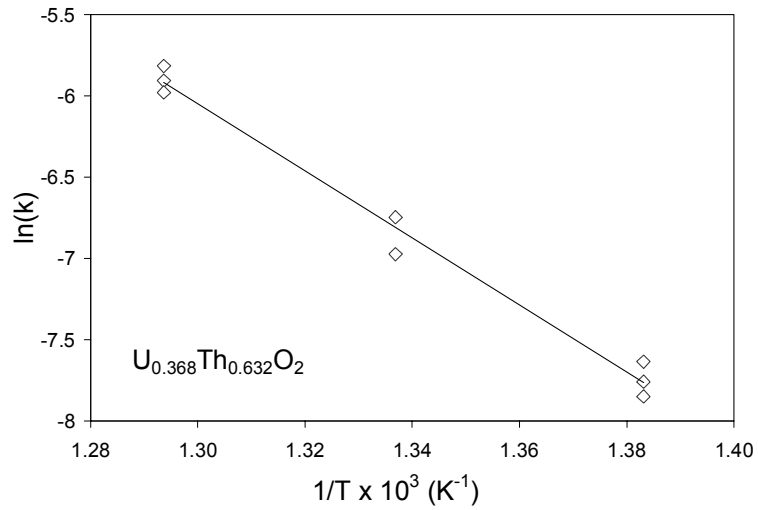


Figure 4-22. Arrhenius plot of $(\text{U}_{0.368}\text{Th}_{0.632})\text{O}_2$ isotherms fit to 3D Diffusion reaction model. Rate constants (k) were determined by fitting gravimetric oxidation data with the 3D diffusion reaction model

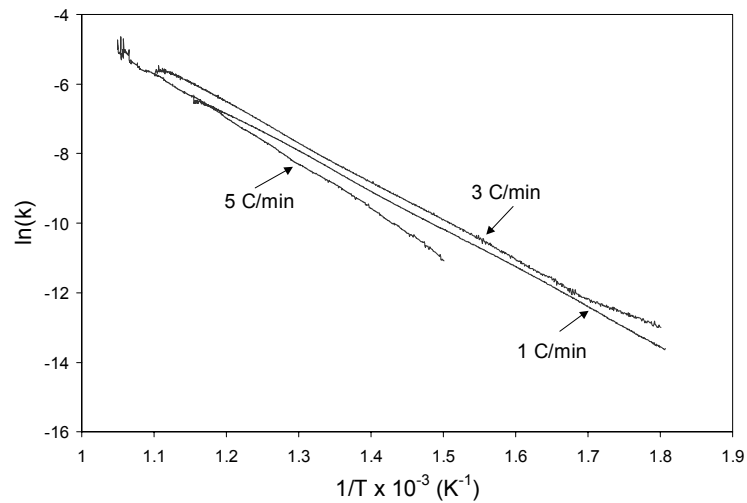


Figure 4-23. Nonisotherms at 1, 3, and 5°C/min $(\text{U}_{0.368}\text{Th}_{0.632})\text{O}_2$ Arrhenius plot fit to 3D diffusion model.

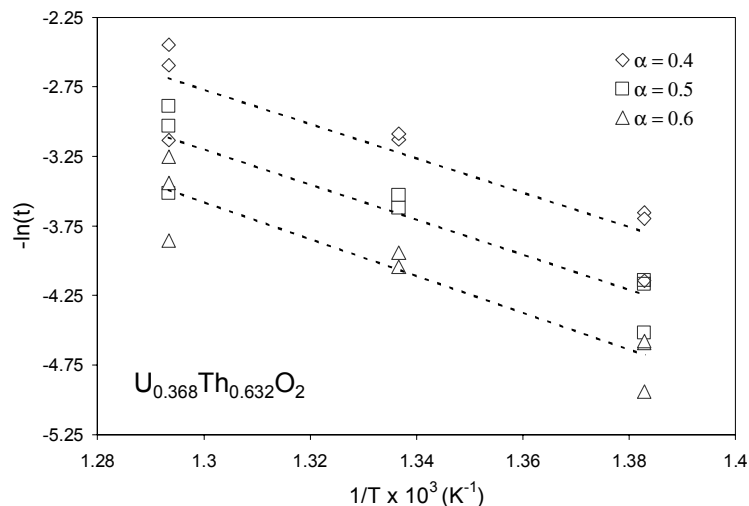


Figure 4-24. Model free ($U_{0.368}Th_{0.632}O_2$) isotherms plotted at $\alpha = 0.4, 0.5, 0.6$. Slope of the linear trendlines gives $-E/R$.

Mixed Oxide ($U_{0.50}Th_{0.50}O_2$)

Model-fitting of ($U_{0.500}Th_{0.500}O_2$) air oxidized pellet fragments introduces another reaction model possibility, Avrami-Erofe'ev. With regard to the raw isothermal data (Figure 4-8), oxidation is more than 50% complete within the first 500 minutes, which may contribute to nonlinear behavior at dwell times < 200 min. However, linear agreement is observed at times greater than 200 min at all isotherms. The validity of using either the reaction model to determine k , E , and A kinetic parameters for the overall process becomes questionable as to its usefulness. Selecting an appropriate model by global linear fit yields little insight into the oxidative mechanism when the bulk of the process is complete in the ill-fit region. Figures 4-25 to 4-28 present the linear fit of isothermal measurements to both Avrami-Erofe'ev and 3D Diffusion models. Figure 4-29 summarizes the rate coefficients according to the 3D diffusion reaction model in an Arrhenius plot of $\ln(k)$ vs $1/T$. When compared to Arrhenius plots of ($U_{0.236}Th_{0.764}O_2$) and ($U_{0.368}Th_{0.632}O_2$), the behavior of ($U_{0.500}Th_{0.500}O_2$) fit to the 3D diffusion reaction model is inconsistent with the lower U content mixed oxides. Table 4-7 lists the rate coefficients and linear correlation to the 3D diffusion model.

Although the lower temperatures exhibit a high degree of linearity, both models fall apart at higher temperatures. This is particularly apparent in the Arrhenius $\ln(k)$ vs. $1/T$ plot, Figure 4-29, of the 3D diffusion reaction model. The plot, in fact, yields a poorly fit linear trendline with a positive slope. Calculating activation energy and frequency would, undoubtedly, be meaningless for model fit isothermal rate data.

Attempts to fit nonisothermal data to a known reaction model also met with similarly inconclusive results as shown in Figure 4-30. At the slower heating rate of $1^\circ\text{C}/\text{min}$, linear agreement was observed in both the Avrami-Erofe'ev and 3D Diffusion models within the temperature range of interest. The higher heating rate, $5^\circ\text{C}/\text{min}$, on the other hand, did not demonstrate linear behavior. This incongruity may be a result of a lag between reaction rate and heating rate, where the temperature rises faster than the material is able to react. Table 4-8 summarizes kinetic parameters calculated from nonisothermal model fitting of rate data to the 3D diffusion and Avrami-Erofe'ev models.

The inability to discern whether $(\text{U}_{0.500}\text{Th}_{0.500})\text{O}_2$ isothermal and nonisothermal rate data conform to known reaction models presented the model-free technique as a desirable method for calculating activation energies. A plot of the isothermal rate data by the model-free method is shown in Figure 4-31. Again, degree of fraction reacted are selected at $\alpha = 0.4, 0.5,$ and 0.6 . Similar to the $(\text{U}_{0.236}\text{Th}_{0.764})\text{O}_2$ and $(\text{U}_{0.368}\text{Th}_{0.632})\text{O}_2$ model-free Arrhenius plots, there is no suggestion of multiple step behavior. Considering the UO_2 system is well known for being a complex multiple step oxidation process, the simple linear behavior would suggest the thorium oxide matrix as a stabilizing influence upon UO_2 oxidation.

Activation energies calculated from the slopes yield values of 85.2 ± 6.5 kJ/mol, 85.6 ± 5.4 kJ/mol, and 86.2 ± 5.4 kJ/mol for degree of conversion 0.4, 0.5, and 0.6 respectively.

Considering that isothermal and nonisothermal model-fitting techniques did not yield a

conclusive reaction model, it is not surprising that model-free activation energies are not in agreement with model-fit results.

Table 4-7. Rate coefficient of isothermal ($U_{0.50}Th_{0.50}$)O₂ agreement to 3D diffusion model

Isothermal temperature	3D diffusion		Avrami-Erofe'ev	
	k (min ⁻¹)	R ²	k (min ⁻¹)	R ²
375°C	6×10^{-4}	0.9858	1×10^{-3}	0.9821
400°C	1×10^{-3}	0.9581	3.3×10^{-3}	0.9648
425°C	6×10^{-4}	0.8528	2×10^{-3}	0.7495
450°C	6×10^{-4}	0.7843	2.2×10^{-3}	0.7763

Table 4-8. Kinetic results for nonisothermal ($U_{0.500}Th_{0.500}$)O₂ in 3D diffusion and Avrami-Erofe'ev models

Nonisothermal	3D Diffusion			Avrami-Erofe'ev		
	ln(A) (min ⁻¹)	E (kJ/mol)	R ²	ln(A) (min ⁻¹)	E (kJ/mol)	R ²
1°C/min	20.12	166.7	0.9894	8.16	90.3	0.9951
5°C/min	8.26	99.7	0.8722	11.91	116.2	0.9735

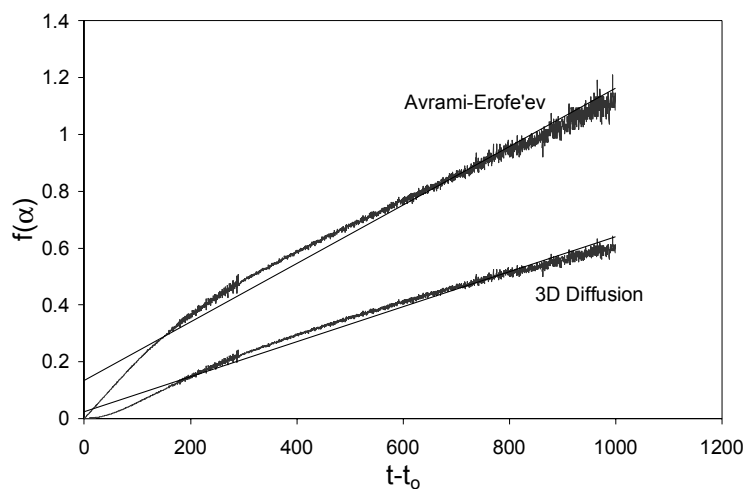


Figure 4-25. Isotherm at 375°C for ($U_{0.50}Th_{0.50}$)O₂ oxidation in 3D Diffusion and Avrami-Erofe'ev models. Linear trendline for both models are shown.

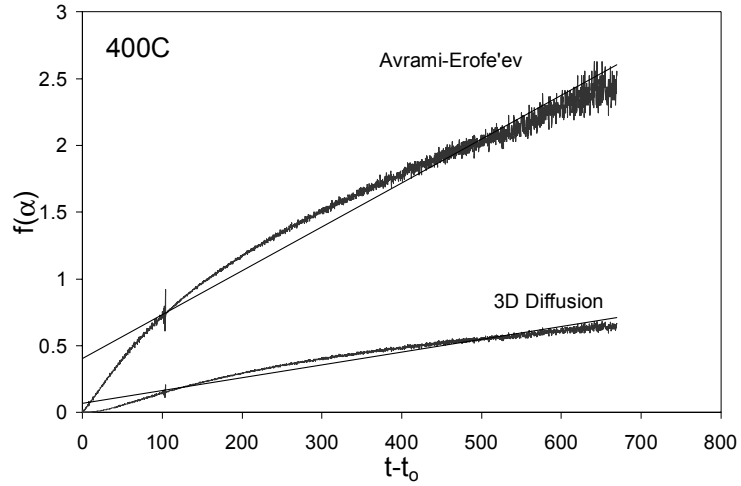


Figure 4-26. Isotherm at 400°C for $(U_{0.50}Th_{0.50})O_2$ oxidation in 3D Diffusion and Avrami-Erofe'ev models. Linear trendline for both models are shown.

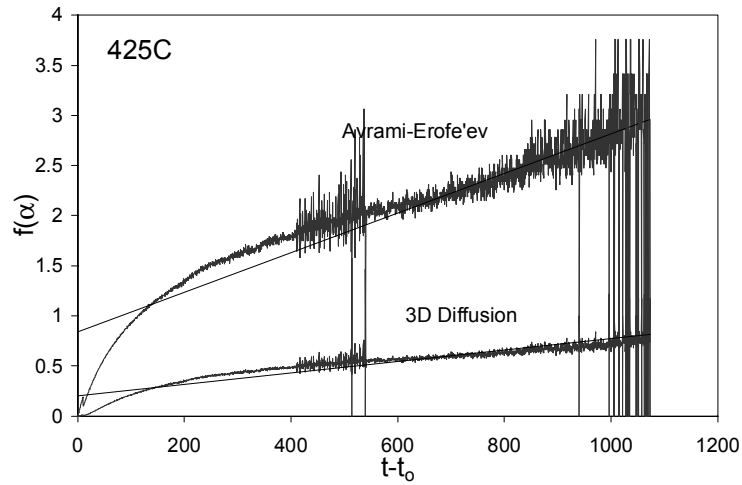


Figure 4-27. Isotherm at 425°C for $(U_{0.50}Th_{0.50})O_2$ oxidation in 3D Diffusion and Avrami-Erofe'ev models. Linear trendline for both models are shown.

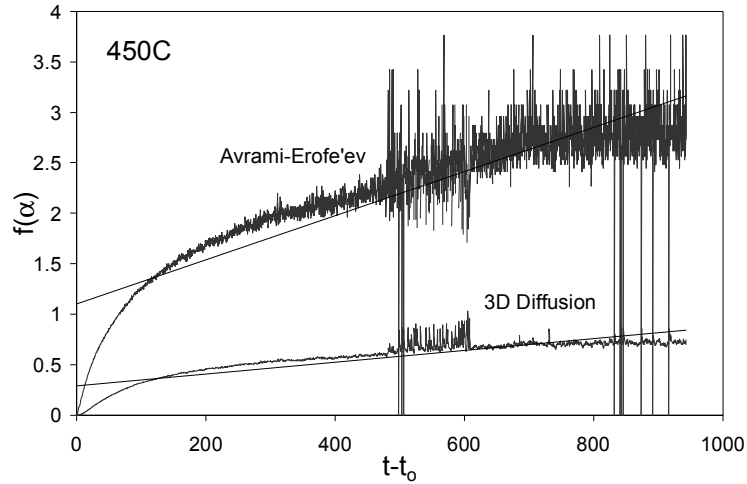


Figure 4-28 Isotherm at 450°C for $(U_{0.50}Th_{0.50})O_2$ oxidation in 3D Diffusion and Avrami-Erofe'ev models. Linear trendline for both models are shown.

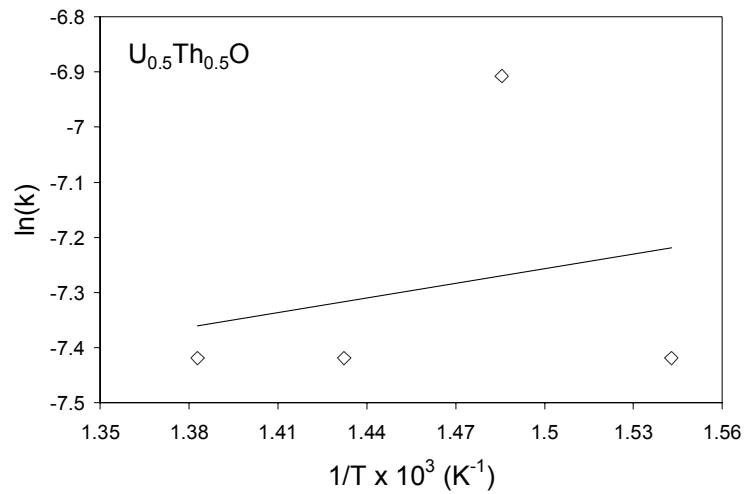


Figure 4-29. Arrhenius plot of $(U_{0.500}Th_{0.500})O_2$ isotherms in 3D Diffusion reaction model. Rate constants (k) were determined by fitting gravimetric oxidation data with the 3D diffusion reaction model

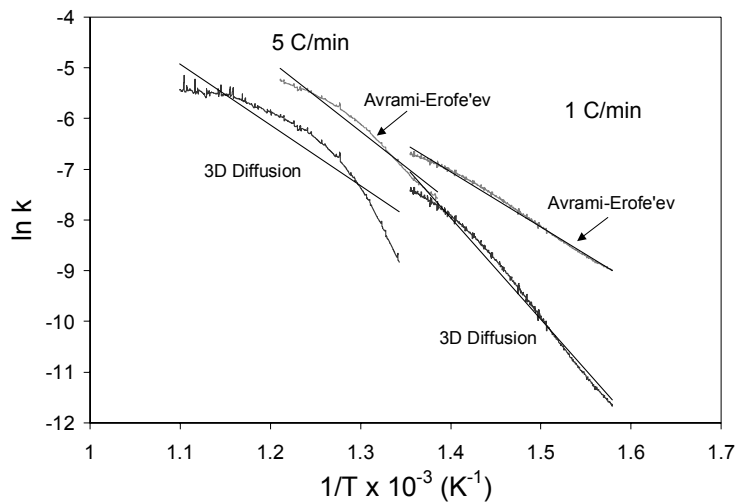
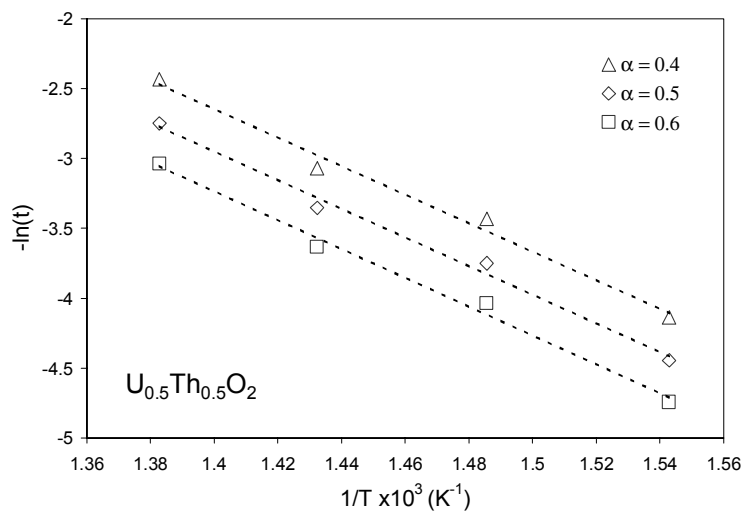


Figure 4-30. Nonisotherms at 1 and 5°C/min ($U_{0.500}Th_{0.500}O_2$) Arrhenius plot fit to Avrami-Erofe'ev and 3D diffusion models. Linear trendlines shown.

Figure 4-31. Model free ($U_{0.500}Th_{0.500}O_2$) isotherms plotted at $\alpha = 0.4, 0.5, 0.6$. Slope of the



linear trendlines gives $-E/R$.

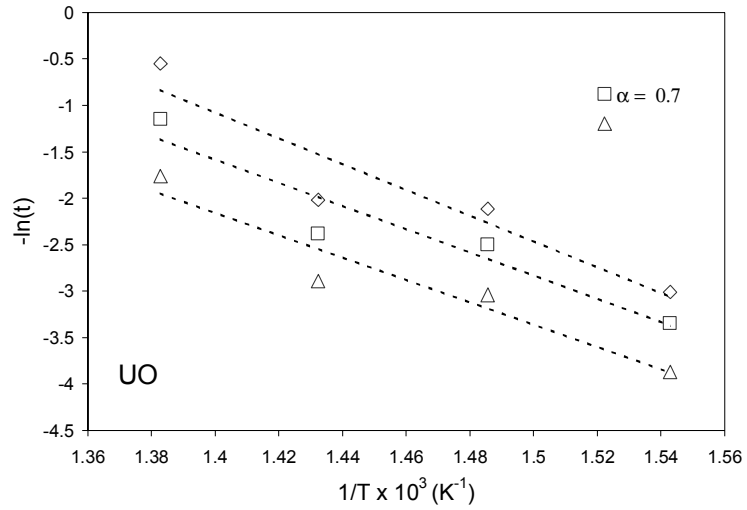
Pure Uranium Dioxide (UO_2)

Kinetic analysis of UO_2 pellet fragments encountered similar results to $(\text{U}_{0.500}\text{Th}_{0.500})\text{O}_2$ material. Linear agreement to the various reaction models was not observed for isothermal and nonisothermal data. Considering UO_2 is known to have a multi-step oxidation, this is not unexpected. As McEachern [McE97a] reported, UO_2 powders oxidize by parabolic kinetics, which indicate the reaction is diffusion controlled, to form U_3O_7 at low temperatures. Diffusion through a discrete layer of the product oxide is the limiting reaction. Two mechanisms, concentration-gradient and discrete-layer, are generally accepted as consistent with the diffusion-controlled kinetics for UO_2 powder oxidation to U_3O_7 . Literature yields activation energy estimates of the U_3O_7 formation on UO_2 powders to be 96 kJ/mol [McE97a].

In terms of U_3O_8 formation, McEachern et al. [McE97b] reported that nucleation and growth mechanisms have been consistently applied to this step. Again, two models are commonly applied in literature, Johnson-Mehl and Avrami-Erofe'ev equations. Also, it has been proven correct that there are at least two different activation energies (at different temperature ranges) for U_3O_8 formation, with a change in oxidation behavior around 300 – 350°C [McE97b]. It is not unlikely, therefore, to expect that same degree of complexity at temperatures greater than 350°C, as examined in this study. Considering the nucleation and growth complexity of U_3O_8 formation, weight gain data is susceptible to interference from $\text{U}_3\text{O}_7/\text{U}_4\text{O}_9$ formation and linear growth rates are not necessarily applicable. McEachern et al. [McE97b] developed a two-dimensional nucleation and growth model for the specific case of U_3O_8 formation on UO_2 pellets, analogous to three-dimensional nucleation and growth models, resulting in a calculated activation energy of 146 ± 10 kJ/mol.

Since oxidation of UO_2 was pursued as a control for comparison purposes, not necessarily identifying oxidation mechanisms, the model-free method was used to determine E. However, knowing the UO_2 fragments have a low surface-to-bulk ratio, it is likely the plot mainly reflects the bulk contribution to oxidation and not U_3O_7 formation.

Activation energies calculated for $\alpha = 0.5, 0.7, \text{ and } 0.9$ across the $375 - 450^\circ\text{C}$ temperature range are $116 \pm 29 \text{ kJ/mol}$, $104 \pm 23 \text{ kJ/mol}$, and $100 \pm 20 \text{ kJ/mol}$ respectively.



These are within the range of values reported in literature for pellet fragments. See Appendix A.

Figure 4-32. Model free UO_2 isotherms plotted at $\alpha = 0.4, 0.5, 0.6$. The slope of the linear trendlines gives $-E/R$.

CHAPTER 5 SUMMARY AND CONCLUSIONS

Two of the compositions analyzed ($(U_{0.236}Th_{0.764})O_2$ and $(U_{0.368}Th_{0.632})O_2$) exhibited satisfactory agreement to any of the basic theoretical reaction models, absent any additional terms to account for particle size or grain size. As a consequence, results calculated with these basic models restrict conclusions that can be drawn (i.e., surface or bulk-dependence). The $(U_{0.500}Th_{0.500})O_2$ and UO_2 compositions did not demonstrate agreement with any of the basic theoretical reaction models. Knowing the two-step nature of UO_2 , the absence of a particle size dependent term prohibited the identification of an appropriate reaction model. Nonisothermal calculations, additionally, were further hindered by the simultaneous time and temperature dependence of measurement. Further quantifying particle characteristics would be necessary to render more precise kinetic parameters.

For the low U compositions, the 3D Diffusion model provided the best fit for isothermal rate data. $(U_{0.236}Th_{0.764})O_2$ fragments, however, did present agreement to 2D diffusion at 450°C. Activation energy values of isothermal rate data calculated using the 3D diffusion reaction model were 62.1 ± 17.9 kJ/mol and 171 ± 8 kJ/mol, for the $(U_{0.236}Th_{0.764})O_2$ and $(U_{0.368}Th_{0.632})O_2$ samples, respectively. Frequency factors ($\ln A$) were 1.71 ± 2.87 min⁻¹ and 20.8 ± 1.3 min⁻¹ for increasing U content, respectively. These values are contrary to the hypothesis that uranium-rich compositions would more readily oxidize than thorium-rich ones. Based on the known cubic fluorite structure, it seems likely that the lattice at interstitial sites accommodates the excess anions without having to undergo phase transformations. Additionally, assuming pellet fragments are polycrystalline, excess anions may also accumulate or migrate along grain

boundaries. This incongruity is likely a result of the limitations attributed to the missing particle size and/or grain size terms. Without fully characterizing the pellet fragments, the basic reaction model can not adequately account for possible complexities, such as multiple mechanisms, simultaneous mechanism, surface-dependency, grain boundary migration. The kinetic analysis in this study does preliminarily suggest that (U,Th)O₂ oxidation occurs by diffusion. X-ray diffraction and uranium valence calculations additionally assert that thorium oxide inhibits uranium from reaching its highest valence state.

The higher uranium (U_{0.500}Th_{0.500})O₂ fragments did not indicate agreement with diffusion-controlled models. In fact, the nucleation and growth Avrami-Erofe'ev reaction model appeared to fit (U_{0.500}Th_{0.500})O₂ rate data better than 3D diffusion in nonisothermally measured fragments. Considering the reaction model agreement alternated between 3D diffusion and Avrami-Erofe'ev, there is likely more than one mechanism in simultaneous action.

In general, nonisothermal rate data, particularly (U_{0.236}Th_{0.764})O₂ and (U_{0.368}Th_{0.632})O₂, did not discriminately identify one model over another, despite exhibiting linear agreement with models identified isothermally. Consequently, little meaning could be drawn from nonisothermal data in this study. Like the nonisothermal data, the relatively untried model-free method reported in 1999 by Vyazovkin and Wight was tentatively used for comparison. There was no correlation noted between (U,Th)O₂ composition and model-free calculated activation energy. Table 20 summarizes values obtained by all three methods.

Gravimetric analysis of UO₂ was also subjected to the same limitations that befell mixed (U,Th)O₂ oxides. Single-step nonisothermal gravitational analysis curves were observed for UO₂ and all (U,Th)O₂ samples. The absence of two-step curves in the case of UO₂ is attributed to the large pellet fragments (90 – 250 μm) used, which have a low surface-to-volume ratio compared with much finer powders. It is unclear from this study whether the single-step behavior observed for the solid solutions was also due to the size of the fragments used, or if such behavior is characteristic of (U,Th)O₂ materials, regardless of the particle size.

The results of this study highlight the complexities in the UO_2 and $(\text{U,Th})\text{O}_2$ oxidation processes, as well as difficulties in performing kinetic analyses of this nature. None of the $(\text{U,Th})\text{O}_2$ samples reached the same degree of uranium oxidation as pure UO_2 , indicating a stabilizing effect by thorium in the solid solution. It is clear that diffusion is the primary mechanism of oxidation with possible nucleation and growth mechanisms observed at increasingly greater uranium content. This, perhaps, may explain the incongruity between activation energies and uranium content. At the lower uranium concentrations where diffusion dominates, activation energy increases with increasing U/Th. At U/Th = 0.5, however, it is no longer clear that diffusion is the primary mechanism of oxidation. There is a suggestion that nucleation and growth mechanisms are beginning to play a significant role in the uranium oxidation. Activation energies calculated, subsequently, do not reveal the system complexity suggested by the model-fit method. Again, further investigation of mid- to high U content mixed oxides may reveal the cause behind the lowered activation energy as compared to lower U/Th oxides.

This study, however, does put forward suggestions as to possible mechanisms for mixed $(\text{U,Th})\text{O}_2$ dry oxidation. X-ray diffraction confirmed that mixed oxide lattice structures remain cubic fluorite during oxidation. Assuming weight gain is solely a result of excess oxygen anions, uranium valency does not proceed to the same extent as oxidation of pure UO_2 . Also, much like UO_2 , excess anions are likely accommodated at interstitial sites and vacancies in the thorium-rich lattice.

Table 5-1. Estimated E and A by model-free and model-fit techniques of $(\text{U,Th})\text{O}_2$ and UO_2

Composition	Model free		Isothermal Model Fit	Nonisothermal Model fit	
	E (kJ/mol)	E (kJ/mol)	ln(A) (min ⁻¹)	E (kJ/mol)	ln(A) (min ⁻¹)
$(\text{U}_{0.236}\text{Th}_{0.764})\text{O}_2$	87 ± 8	62.7 ± 17.9	1.71 ± 2.87	92.9 ± 1.3	5.3 ± 0.2
$(\text{U}_{0.368}\text{Th}_{0.632})\text{O}_2$	106 ± 31	171 ± 8	20.8 ± 1.3	97.7 ± 9.1	7.3 ± 1.2
$(\text{U}_{0.500}\text{Th}_{0.500})\text{O}_2$	86 ± 6	--	--	103 ± 18*	10 ± 3*
UO_2	107 ± 42	--	--	--	--

*Avrami-Erofe'ev model, otherwise 3D diffusion

APPENDIX A
ACTIVATION ENERGIES

Table A-1. Published estimates of U_3O_7/U_4O_9 activation energy of formation

E_{act} (kJ/mol)	Sample	T (°C)	Ref.
104*	UO ₂ powder	131 – 164.5	Anderson et al. (1955)
102*	UO ₂ powder	161 – 350	Aronson et al. (1957)
90.8	UO ₂ powder and pellets	125 – 280	[Bla58]
120 ± 8	UO ₂ powder	143 – 211	Walker (1965)
100	Spent LWR fuel	175 – 195	Einzig et al. (1992)
113 ± 17	Spent LWR fuel	175 – 225	Woodley et al. (1988, 1989)

* Activation energy re-calculated from investigators original data using the discrete-layer kinetic model (rather than the concentration-gradient model) [McE97a].

Table A-2. Published estimates of U_3O_8 formation on UO₂ activation energies

E_{act} (kJ/mol)	Sample	T (°C)	Method	Cited Ref.
146	UO ₂ powder	278-325	Gravimetric	Aronson (1961)
127.6	UO ₂ powder	315-360	Gravimetric	Saito (1975)
~100*	UO ₂ microspheres	300-450	Gravimetric	Ohashi (1987)
161.5	UO ₂ powder	365-400	DTA	Landspersky (1966)
134.7	UO ₂ powder	312-352	Gravimetric	Walker (1965)
110.5	UO ₂ pellets	279-361	Gravimetric	Walker (1965)
170.2	AGR pellet fragments	200-300	Gravimetric	Tucker (1987)
48	AGR pellet fragments	300-550	Gravimetric	Tucker (1987)
124-139	CANDU pellets	200-300	XRD	Taylor (1992)
102 ⁺	LWR Pellets	200-250	Gravimetric	White (1983)
163	UO ₂ powder	200-350	Gravimetric	[Boa77]
170	CANDU pellets	330-350	Gravimetric	[Boa77]
67	CANDU pellets	350-450	Gravimetric	[Boa77]
172	CANDU fuel element	250-300	Progression of oxidation front	[Boa77]
63	CANDU fuel element	300-350	Progression of oxidation front	[Boa77]
143	UO ₂ pellet fragments	250-350	Gravimetric	You (1992)
109	UO ₂ pellet fragments	350-400	Gravimetric	You (1992)
94.5	used LWR fuel	300-400	Gravimetric	You (1992)
140	Unirradiated CANDU fragments	175-400	Gravimetric	Hastings (1986)
120	Used CANDU fragments	175-400	Gravimetric	Hastings (1986)
194	Used LWR fragments	250-360	Visual examination	Einzig (1984)

* Activation energy was observed to vary as a function of oxygen pressure.

⁺ The value of 120 kJ/mol corresponds to the oxidation prior to powder formation. The post-spallation period displayed an activation energy of 160 kJ/mol [McE97b].

Table A-3. Published estimates of UO₂ cation and anion diffusion activation energies

E _{act} (kJ/mol)	Sample	T(°C)	Method	Ref
Cation Diffusion				
372	U in UO _{2.01}	1400 – 1650	α-energy spectrometry	[Haw68]
398	U in UO _{2.03}	1400 – 1600	α-energy spectrometry	[Haw68]
439	U in UO _{2.1}	1400 – 1650	α-energy spectrometry	[Haw68]
339	U in UO _{2.15}	1350 – 1450	α-energy spectrometry	[Haw68]
304	²³⁷ U in UO _{2+x}		Lattice diffusion contribution	[Fur68]
438	²³⁷ U in UO ₂	1300 – 1600	Cited Lindner and Schmitz	[Fur68]
411	U in (S) UO ₂		Cited Reimann & Lundy	[And83]
Anion Diffusion				
273	O in UO ₂	550 – 780	Cited Auskern and Belle	[And83]
237	O in UO ₂	600 – 1500	Cited Belle	[And83]
248	O in UO ₂	780 – 1250	Cited Marin & Contamin	[And83]
124	O in UO _{2.004}		Cited Auskern & Belle	[And83]
124	O in UO _{2.063}		Cited Auskern & Belle	[And83]
89	O in UO _{2.006}		Cited Contamin et al.	[And83]
89	O in UO _{2.020}		Cited Contamin et al.	[And83]
90	O in UO _{2.10}		Cited Contamin et al.	[And83]
92	O in UO _{2.12}		Cited Contamin et al.	[And83]
92	O in UO _{2.16}		Cited Contamin et al.	[And83]
97	O in UO _{2.08}		Cited Murch et al.	[And83]
99.6	O in UO _{2+x}		Self diffusion, cited Breitung (1978)	[Ari00]
100.1 - 103.5	O in UO _{2+x}		Chemical diffusion, cited Breitung (1978)	[Ari00]
119.2	O in UO _{2+x}		Chemical diffusion, cited Lay (1970)	[Ari00]
86.6	O in UO _{2+x}		Chemical diffusion, cited Bayoglu (1984)	[Ari00]
96.7	O in UO _{2+x}		Self diffusion, cited Murch (1975)	[Ari00]

(P) polycrystalline; (S) single crystal

Table A-4. Published estimates of ThO₂ cation and anion diffusion activation energies

E _{act} (kJ/mol)	Sample	T(°C)	Method	Ref
Cation Diffusion				
247	Th in (P) ThO ₂	1600 – 2100	α-energy spectrometry	[Haw68]
626	Th in (S) ThO ₂	1846 – 2045	Cited King	[And83]
628	²³⁸ Th in (S) ThO ₂		Cited Matzke	[And83]
320	²³⁷ U in (P) ThO ₂	1800 – 2000	Lattice diffusion contribution	[Fur68]
201	²³⁷ U in (P) ThO ₂	1800 – 2000	Grain boundary diffusion contribution	[Fur68]
Anion Diffusion				
219	¹⁸ O in (P) ThO ₂	1099 – 1644	mass spectrometry	[And84]
209	¹⁸ O in (S) ThO ₂	1099 – 1644	mass spectrometry	[And84]
209	¹⁸ O in (S) ThO ₂	845 – 1646	gas-solid isotope exchange (intrinsic contribution)	[And76]
73.6	¹⁸ O in (S) ThO ₂	845 – 1646	gas-solid isotope exchange (extrinsic contribution)	[And76]
275	O in ThO ₂	900 – 1500	Cited Edwards et al.	[And83]
238	O in ThO ₂	2100 - 2800	Cited Lam	[Fre80]

(P) polycrystalline; (S) single crystal

Table A-5. Published estimates of diffusion in (U,Th)O₂ activation energies

E _{act} (kJ/mol)	Sample	T(°C)	Method	Ref
360	²³⁷ U in (P) UO ₂ -ThO ₂	1800 – 2300	Lattice diffusion contribution	[Fur68]
269	²³⁷ U in (P) UO ₂ -ThO ₂	1800 – 2300	Grain boundary diffusion contribution	[Fur68]
99.6	O in U _{0.01} Th _{0.99} O _{2+x}	940 – 1040	Chemical diffusion	[Ari00]
88.3	O in U _{0.03} Th _{0.97} O _{2+x}	940 – 1040	Chemical diffusion	[Ari00]
71.0	O in U _{0.05} Th _{0.95} O _{2+x}	940 – 1040	Chemical diffusion	[Ari00]
66.8	O in U _{0.20} Th _{0.80} O _{2+x}	1009 – 1100	Chemical diffusion, cited Matsui (1985)	[Ari00]
107.1	O in U _{0.30} Th _{0.70} O _{2+x}	245 – 455	Chemical diffusion, cited Furuya (1990)	[Ari00]
93.1	O in U _{0.40} Th _{0.50} O _{2+x}	1009 – 1100	Chemical diffusion, cited Matsui (1985)	[Ari00]
112.1	O in U _{0.50} Th _{0.50} O _{2+x}	245 – 455	Chemical diffusion, cited Furuya (1990)	[Ari00]
108.0	O in U _{0.70} Th _{0.30} O _{2+x}	245 – 455	Chemical diffusion, cited Furuya (1990)	[Ari00]

Table A-6. Kinetic parameters of mixed urania-thoria oxides

Sample	Heating rate (K/min)	Activation energy (kJ/mol)	Pre-exponential factor (log A) (/min)
(U _{0.15} Th _{0.85})O ₂	0.5	45 ± 0.3	0.747 ± 0.006
	1	42 ± 0.3	0.693 ± 0.004
	5	31 ± 0.2	0.471 ± 0.002
	Isotherms	51 ± 1	2.6 ± 0.4
(U _{0.30} Th _{0.70})O ₂	0.5	51 ± 0.6	1.820 ± 0.095
	1	49 ± 0.5	1.800 ± 0.090
	5	49 ± 0.4	1.350 ± 0.073
	Isotherms	45 ± 1	2.9 ± 0.3
(U _{0.72} Th _{0.28})O ₂	0.5	81 ± 0.4	5.860 ± 0.910
	1	70 ± 0.6	4.750 ± 0.760
	2	70 ± 0.6	1.890 ± 0.035
	5	46 ± 0.4	0.728 ± 0.012
	Isotherms	91 ± 1	6.5 ± 0.6
(U _{0.77} Th _{0.23})O ₂	0.5	90 ± 0.6	7.250 ± 0.140
	1	79 ± 0.4	5.860 ± 0.160
	2	67 ± 0.8	4.760 ± 0.190
	5	66 ± 0.8	4.600 ± 0.160
	Isotherms	82 ± 1	7.2 ± 1.4

[Ant00]

APPENDIX B
X-RAY DIFFRACTION PATTERNS

Table B-1. $U_{0.368}Th_{0.632}O_{2+x}$ isothermal 400°C air oxidized compared to JCPDS standards

$2\theta_{meas}$	Int*	hkl	$2\theta_{25U}$	Int	hkl	$2\theta_{ThO_2}$	Int	hkl	$2\theta_{UO_2}$	Int	hkl
27.830	51(100)	111	27.791	100	111	27.581	100	111	28.281	100	111
32.245	16(31)	200	32.186	40	200	31.962	35	200	32.741	50	200
46.270	21(41)	220	46.172	60	220	45.827	58	220	49.968	50	220
54.870	23(45)	311	54.769	55	311	54.312	64	311	55.754	45	311
57.525	5(10)	222	57.411	12	222	56.984	11	222	58.428	8	222
67.510	3(6)	400	67.366	8	400	66.821	8	400	68.594	10	400
74.555	9(18)	331	74.403	18	331	73.794	26	331	75.775	20	331
76.815	6(12)	420	76.659	14	420	76.010	17	420	78.121	15	420
85.820	5(10)	422	85.562	14	422	84.804	20	422	87.314	15	422
92.465	6(12)	511	92.185	14	511	91.316	19	511			
103.650	1(2)	440				102.279	6	440			
110.600	4(8)	531				109.069	18	531			
113.010	2(4)	600				111.377	8	600			
123.010	2(4)	620				121.073	14	620			
131.345	2(4)	533				129.026	9	533			
134.440	1(2)	622				131.922	9	622			
			$2\theta_{Si}$	Int	hkl						
28.375	100	111	28.466	100	111						
47.235	30	220	47.343	55	220						
56.060	14	311	56.170	30	311						
69.120	2	400	69.194	6	400						
76.305	5	331	76.450	11	331						
87.955	6	422	88.115	12	422						
94.830	2	511	95.048	6	511						
106.595	2	440	106.839	3	440						
113.995	2	531	114.230	7	531						
127.420	2	620	127.728	8	620						
136.745	1	533	137.124	3	533						

*The relative intensities designated in parentheses are calculated based on the identified U,Th oxide angles, not including Si, to determine whether intensities are consistent with those reported for $U_{0.25}Th_{0.75}O_2$, ThO_2 , and UO_2 cubic oxides. Silicon standard measured and reported values are also shown

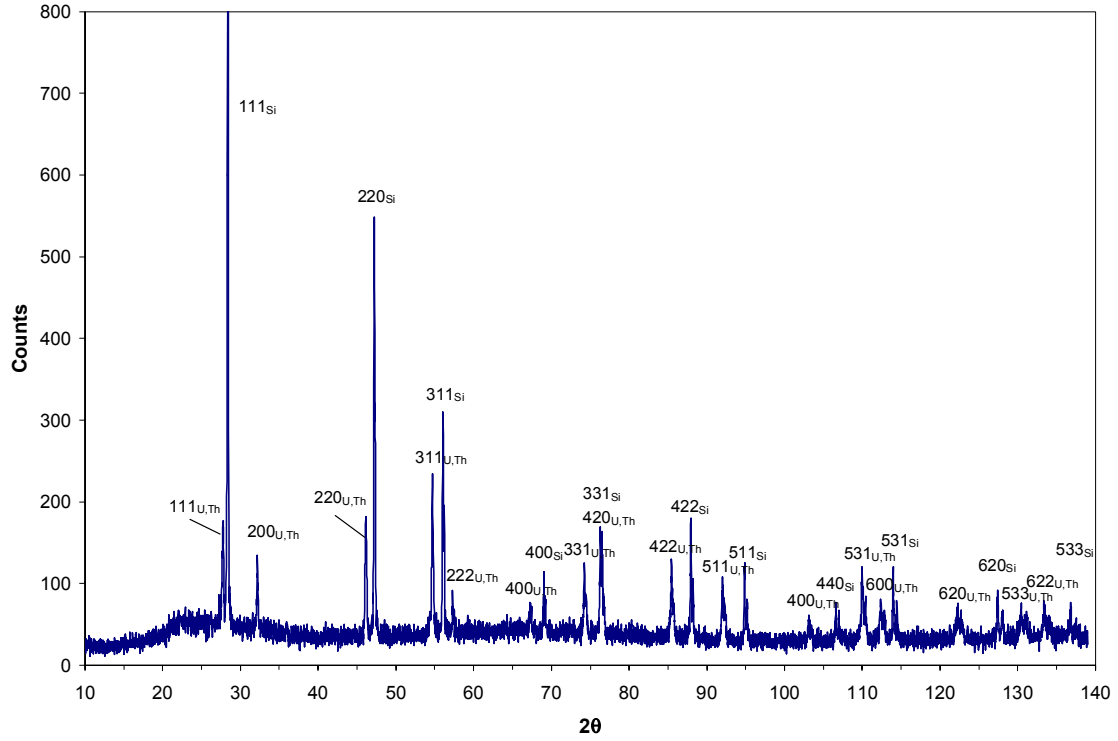


Figure B-1. XRD pattern for 450°C isotherm of co-milled 23.6% UO_2 fragments

Anode: Cu

$\lambda_{\alpha 1}, \lambda_{\alpha 2}$: 1.54056, 1.54439

Generator Voltage: 40V

Tube Current: 20

Scan Step Size: 0.020°

Scan Step Time: 0.25 sec

Table B-2. XRD peak intensities for 450°C isotherm of co-milled 23.6% UO_2 fragments

2θ	d	Int	h	k	l
130.455	0.8483	1	5	3	3
133.395	0.8387	1	6	2	2
(Si)					
28.375	3.1428	100	1	1	1
47.22	1.9233	29	2	2	0
56.05	1.6394	13	3	1	1
69.035	1.3593	3	4	0	0
76.29	1.2471	5	3	3	1
87.945	1.1094	5	4	2	2
94.85	1.046	2	5	1	1
106.575	0.9609	1	4	4	0
113.965	0.9186	2	5	3	1
127.435	0.8591	1	6	2	0
136.78	0.8285	1	5	3	3
27.76	3.211	11	1	1	1
32.17	2.7802	5	2	0	0
46.115	1.9667	8	2	2	0
54.66	1.6778	8	3	1	1
57.31	1.6063	2	2	2	2
67.255	1.3909	1	4	0	0
74.245	1.2763	3	3	3	1
76.49	1.2443	4	4	2	0
85.47	1.1351	3	4	2	2
92.015	1.0707	2	5	1	1
103.06	0.9838	1	4	4	0
109.945	0.9407	2	5	3	1
112.4	0.9269	1	6	0	0
122.235	0.8797	1	6	2	0

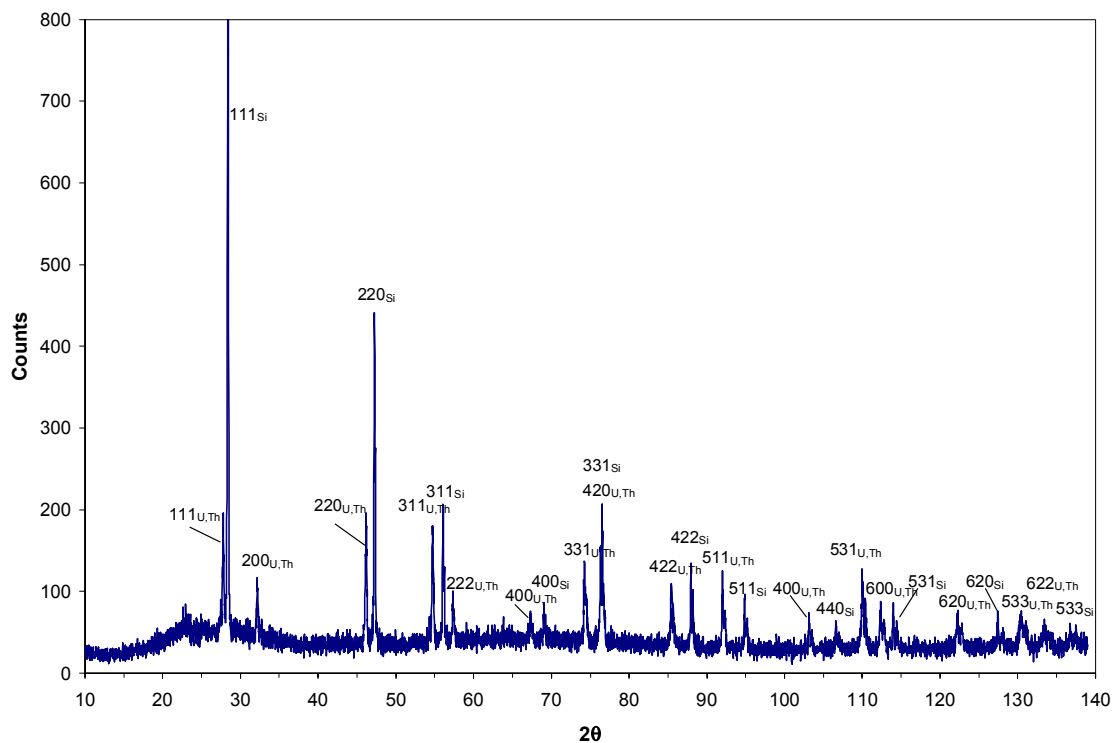


Figure B-2. XRD pattern for 500°C isotherm of co-milled 23.6% UO_2 fragments

Anode: Cu

$\lambda_{\alpha_1}, \lambda_{\alpha_2}$: 1.54056, 1.54439

Generator Voltage: 40V

Tube Current: 20

Scan Step Size: 0.020°

Scan Step Time: 0.25 sec

Table B-3. XRD peak intensities for 500°C isotherm of co-milled 23.6% UO_2 fragments

2θ	d	Int	h	k	l
27.775	3.2093	13	1	1	1
32.195	2.7781	4	2	0	0
46.155	1.9651	7	2	2	0
54.705	1.6765	6	3	1	1
57.325	1.6059	2	2	2	2
67.24	1.3912	1	4	0	0
74.27	1.2759	3	3	3	1
76.54	1.2437	4	4	2	0
85.44	1.1354	2	4	2	2
92.015	1.0707	2	5	1	1
103.11	0.9835	1	4	4	0
110.04	0.9401	2	5	3	1
112.38	0.9271	1	6	0	0
122.27	0.8796	1	6	2	0
130.41	0.8485	1	5	3	3
133.44	0.8386	1	6	2	2
Si					
28.38	3.1422	100	1	1	1
47.235	1.9227	21	2	2	0
56.045	1.6395	7	3	1	1
69.025	1.3595	1	4	0	0
76.305	1.2469	4	3	3	1
87.945	1.1094	3	4	2	2
94.86	1.0459	2	5	1	1
106.59	0.9608	1	4	4	0
113.99	0.9185	1	5	3	1
127.405	0.8592	1	6	2	0
136.76	0.8286	0	5	3	3

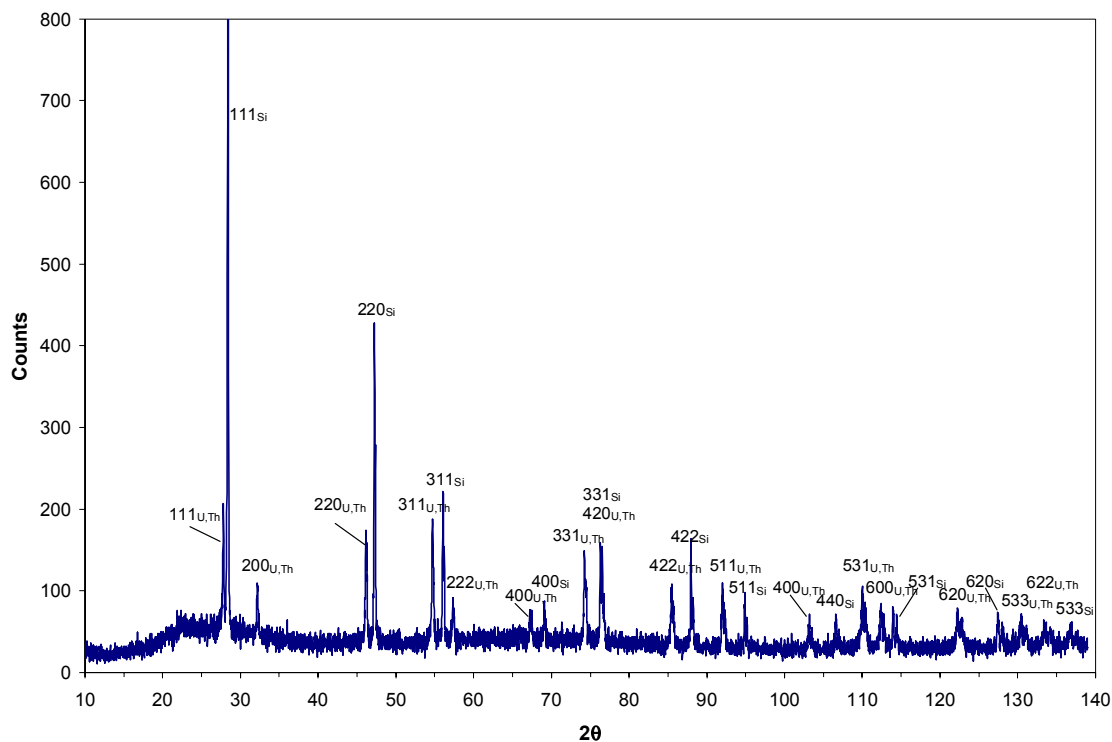


Figure B-3. XRD pattern for 550°C isotherm of co-milled 23.6% UO_2 fragments

Anode: Cu

$\lambda_{\alpha 1}, \lambda_{\alpha 2}$: 1.54056, 1.54439

Generator Voltage: 40V

Tube Current: 20

Scan Step Size: 0.020°

Scan Step Time: 0.25 sec

Table B-4. XRD peak intensities for 550°C isotherm of co-milled 23.6% UO_2 fragments

2θ	d	Int	h	k	l	(Si)
27.795	3.207	14	1	1	1	28.38 3.1422 100 1 1 1
32.215	2.7764	4	2	0	0	47.23 1.9229 21 2 2 0
46.125	1.9663	7	2	2	0	56.05 1.6394 8 3 1 1
54.69	1.6769	7	3	1	1	69.065 1.3588 2 4 0 0
57.37	1.6048	2	2	2	2	76.29 1.2471 4 3 3 1
67.25	1.391	1	4	0	0	87.955 1.1093 4 4 2 2
74.265	1.276	4	3	3	1	94.855 1.046 2 5 1 1
76.525	1.2439	4	4	2	0	106.61 0.9607 1 4 4 0
85.46	1.1352	2	4	2	2	113.995 0.9185 1 5 3 1
92.055	1.0703	2	5	1	1	127.495 0.8589 1 6 2 0
103.135	0.9833	1	4	4	0	136.79 0.8285 0 5 3 3
110.01	0.9403	2	5	3	1	
112.37	0.9271	1	6	0	0	
122.2	0.8799	1	6	2	0	
130.435	0.8484	1	5	3	3	
133.305	0.839	0	6	2	2	

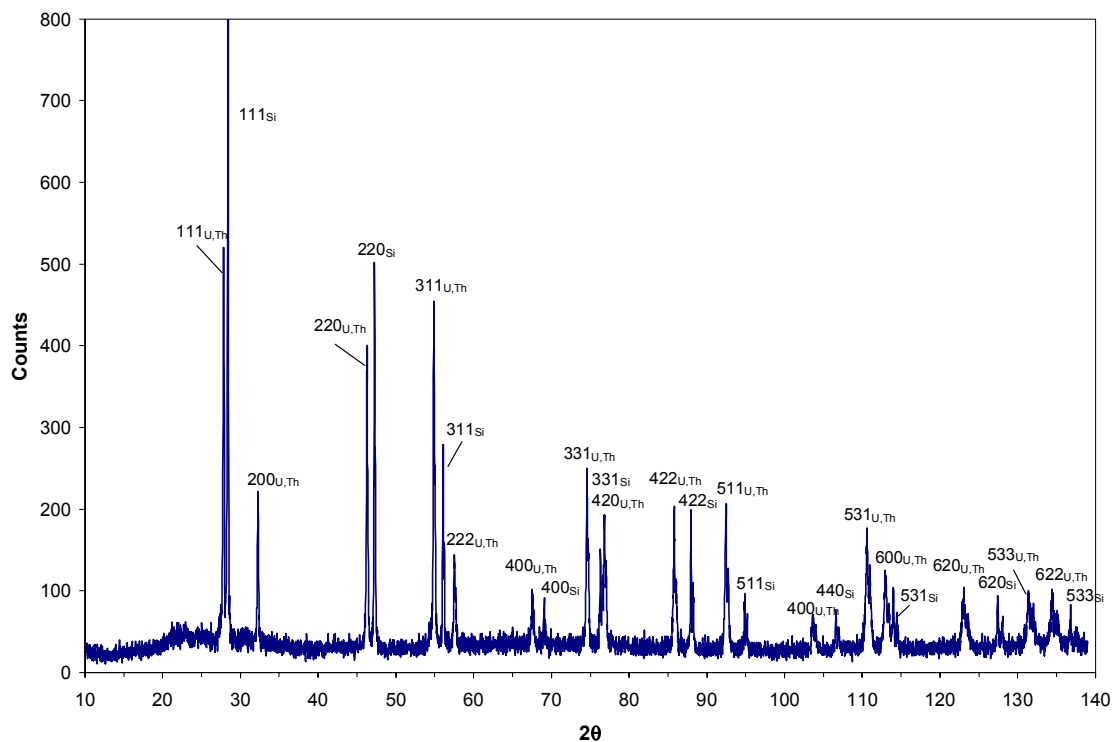


Figure B-4. XRD pattern for 400°C isotherm of co-milled 36.8% UO_2 fragments

Anode: Cu

$\lambda_{\alpha 1}, \lambda_{\alpha 2}$: 1.54056, 1.54439

Generator Voltage: 40V

Tube Current: 20

Scan Step Size: 0.020°

Scan Step Time: 0.25 sec

Table B-5. XRD peak intensities for 400°C isotherm of co-milled 36.8% UO_2 fragments

2θ	d	Int	h	k	l
27.83	3.2031	51	1	1	1
32.245	2.7739	16	2	0	0
46.27	1.9605	21	2	2	0
54.87	1.6718	23	3	1	1
57.525	1.6008	5	2	2	2
67.51	1.3863	3	4	0	0
74.555	1.2718	9	3	3	1
76.815	1.2399	6	4	2	0
85.82	1.1314	5	4	2	2
92.465	1.0666	6	5	1	1
103.65	0.9798	1	4	4	0
110.6	0.9369	4	5	3	1
113.01	0.9237	2	6	0	0
123.01	0.8765	2	6	2	0
131.345	0.8453	2	5	3	3
134.44	0.8354	1	6	2	2

Si					
28.375	3.1428	100	1	1	1
47.235	1.9227	30	2	2	0
56.06	1.6391	14	3	1	1
69.12	1.3579	2	4	0	0
76.305	1.2469	5	3	3	1
87.955	1.1093	6	4	2	2
94.83	1.0462	2	5	1	1
106.595	0.9608	1	4	4	0
113.995	0.9185	2	5	3	1
127.42	0.8591	2	6	2	0
136.745	0.8286	1	5	3	3

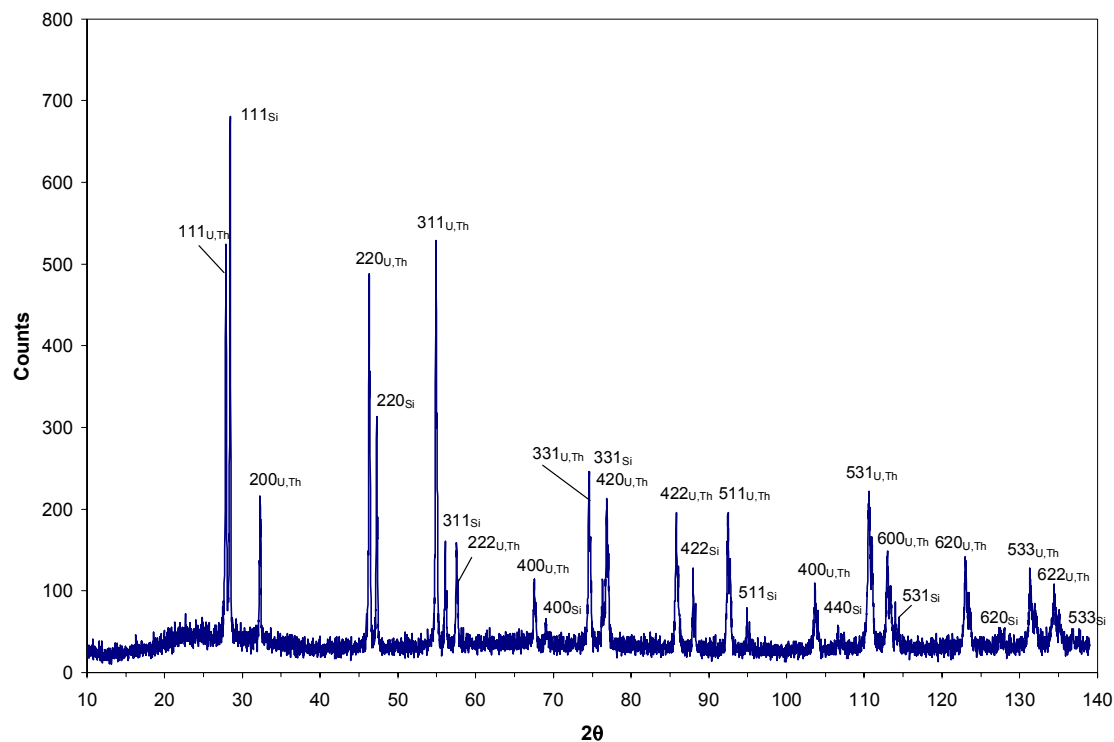


Figure B-5. XRD pattern for 450°C isotherm of co-milled 36.8% UO_2 fragments

Anode: Cu
 $\lambda_{\alpha 1}, \lambda_{\alpha 2}$: 1.54056, 1.54439
 Generator Voltage: 40V
 Tube Current: 20

Scan Step Size: 0.020°
 Scan Step Time: 0.25 sec

Table B-6. XRD peak intensities for 450°C isotherm of co-milled 36.8% UO_2 fragments

2θ	d	Int	h	k	l	Si					
27.85	3.2008	78	1	1	1	28.405	3.1395	100	1	1	1
32.27	2.7718	25	2	0	0	47.255	1.9219	25	2	2	0
46.29	1.9597	45	2	2	0	56.075	1.6387	11	3	1	1
54.88	1.6715	41	3	1	1	69.1	1.3582	1	4	0	0
57.535	1.6006	9	2	2	2	76.325	1.2466	5	3	3	1
67.52	1.3861	4	4	0	0	87.98	1.1091	5	4	2	2
74.515	1.2724	12	3	3	1	94.875	1.0458	2	5	1	1
76.905	1.2387	10	4	2	0	106.615	0.9606	1	4	4	0
85.785	1.1317	7	4	2	2	113.995	0.9185	2	5	3	1
92.45	1.0668	9	5	1	1	127.395	0.8592	1	6	2	0
103.625	0.98	3	4	4	0	136.74	0.8286	1	5	3	3
110.575	0.9371	8	5	3	1						
112.95	0.924	5	6	0	0						
123.015	0.8764	4	6	2	0						
131.25	0.8457	3	5	3	3						
134.45	0.8354	2	6	2	2						

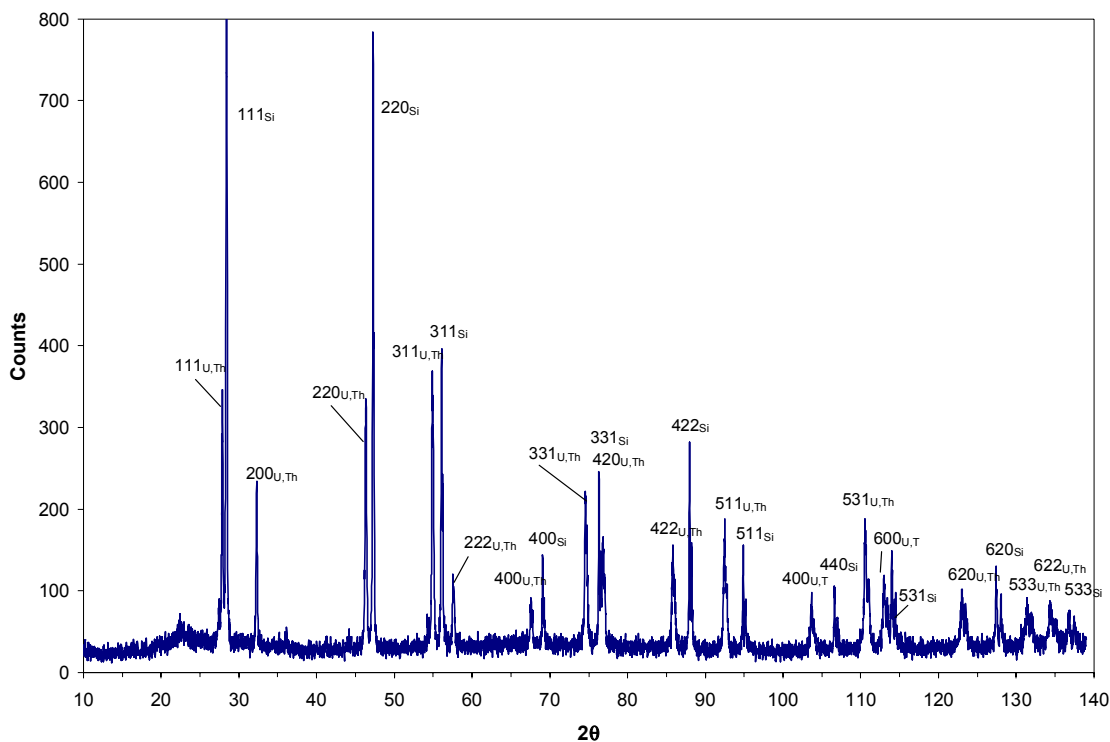


Figure B-6. XRD pattern for 500°C isotherm of co-milled 36.8% UO_2 fragments

Anode: Cu

$\lambda_{\alpha 1}, \lambda_{\alpha 2}$: 1.54056, 1.54439

Generator Voltage: 40V

Tube Current: 20

Scan Step Size: 0.020°

Scan Step Time: 0.25 sec

Table B-7. XRD peak intensities for 500°C isotherm of co-milled 36.8% UO_2 fragments

2θ	d	Int	h	k	l	Si	U,Th
27.85	3.2008	24	1	1	1	28.405	3.1395
32.285	2.7705	14	2	0	0	47.255	1.9219
46.27	1.9605	14	2	2	0	56.065	1.639
54.85	1.6724	12	3	1	1	69.085	1.3585
57.53	1.6007	3	2	2	2	76.325	1.2466
67.55	1.3856	2	4	0	0	87.95	1.1094
74.53	1.2721	6	3	3	1	94.86	1.0459
76.885	1.2389	4	4	2	0	106.59	0.9608
85.8	1.1316	3	4	2	2	113.965	0.9186
92.46	1.0667	4	5	1	1	127.395	0.8592
103.65	0.9798	1	4	4	0	136.76	0.8286
110.515	0.9374	3	5	3	1		
112.975	0.9239	2	6	0	0		
122.995	0.8765	2	6	2	0		
131.33	0.8454	1	5	3	3		
134.36	0.8357	1	6	2	2		

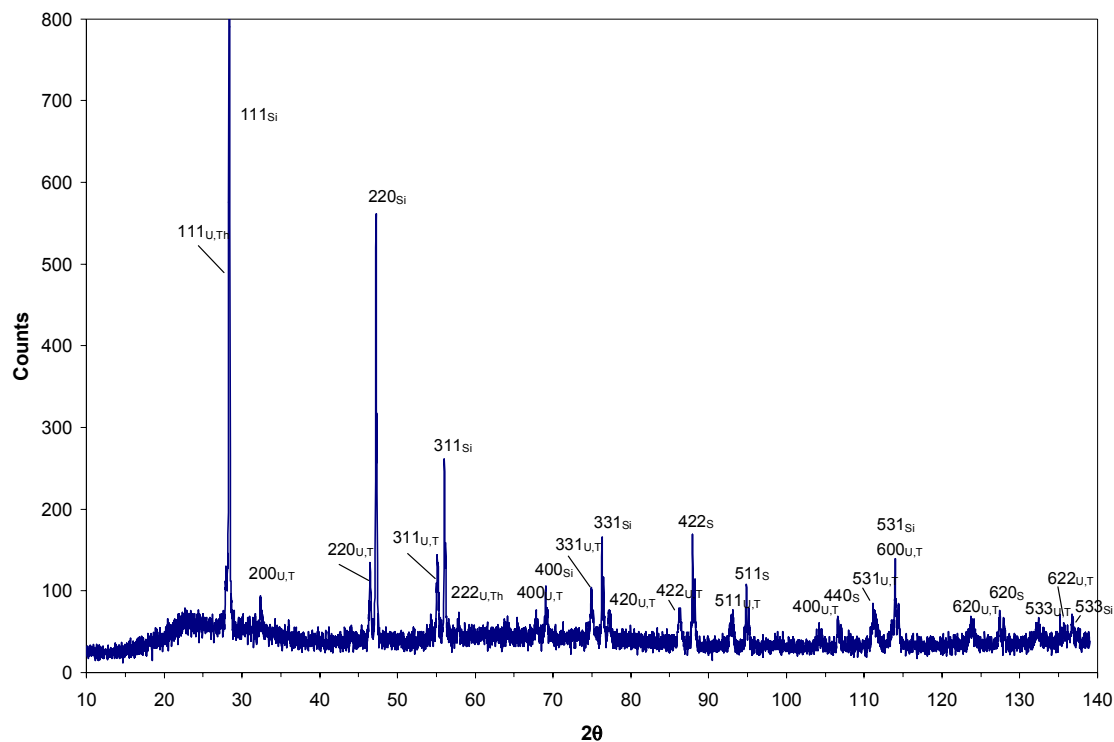


Figure B-7. XRD pattern for 375°C isotherm of co-milled 50.0% UO_2 fragments

Anode: Cu
 $\lambda_{\alpha 1}, \lambda_{\alpha 2}$: 1.54056, 1.54439
 Generator Voltage: 40V
 Tube Current: 20

Scan Step Size: 0.020°
 Scan Step Time: 0.25 sec

Table B-8. XRD peak intensities for 375°C isotherm of co-milled 50.0% UO_2 fragments

2θ	d	Int	h	k	l
27.92	3.1929	5	1	1	1
32.405	2.7605	2	2	0	0
46.47	1.9525	3	2	2	0
55.16	1.6637	4	3	1	1
56.2	1.6354	4	2	2	2
67.78	1.3814	1	4	0	0
74.915	1.2665	2	3	3	1
76.52	1.2439	2	4	2	0
86.26	1.1267	1	4	2	2
92.805	1.0636	1	5	1	1
104.37	0.9750	0	4	4	0
111.205	0.9335	1	5	3	1
113.985	0.9185	2	6	0	0
123.7	0.8736	0	6	2	0
128.005	0.8570	0	5	3	3
132.465	0.8417	0	6	2	2
(Si)					
28.37	3.1433	100	1	1	1
47.22	1.9233	26	2	2	0
56.04	1.6397	9	3	1	1
69.04	1.3593	2	4	0	0
76.3	1.2470	4	3	3	1
87.945	1.1094	4	4	2	2
94.84	1.0461	2	5	1	1
106.635	0.9605	1	4	4	0
113.985	0.9185	2	5	3	1
127.41	0.8592	1	6	2	0
136.7	0.8287	1	5	3	3

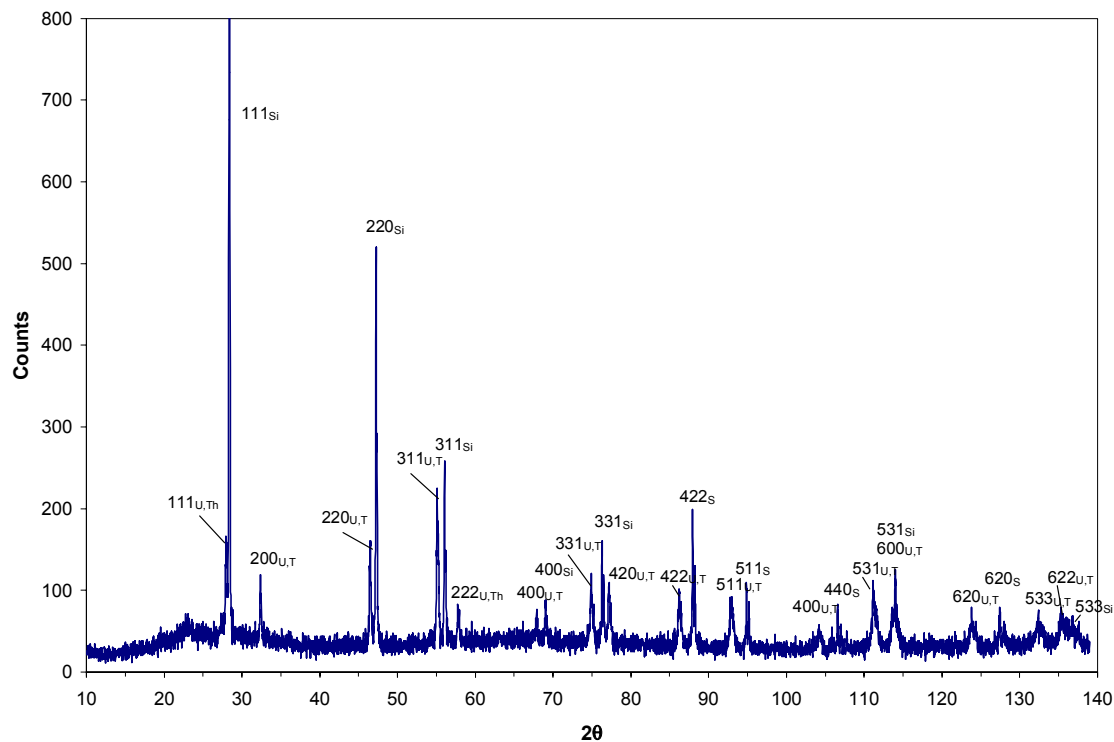


Figure B-8. XRD pattern for 400°C isotherm of co-milled 50.0% UO_2 fragments

Anode: Cu
 $\lambda_{\alpha_1}, \lambda_{\alpha_2}$: 1.54056, 1.54439
 Generator Voltage: 40V
 Tube Current: 20

Scan Step Size: 0.020°
 Scan Step Time: 0.25 sec

Table B-9. XRD peak intensities for 400°C isotherm of co-milled 50.0% UO_2 fragments

2θ	d	Int	h	k	l	(Si)
27.965	3.1879	11	1	1	1	28.38 3.1422 100 1 1 1
32.415	2.7597	5	2	0	0	47.235 1.9227 28 2 2 0
46.3525	1.9504	7	2	2	0	56.05 1.6394 11 3 1 1
55.105	1.6652	9	3	1	1	69.05 1.3591 2 4 0 0
57.845	1.5927	2	2	2	2	76.3 1.2470 5 3 3 1
67.83	1.3805	1	4	0	0	87.945 1.1094 6 4 2 2
74.865	1.2673	2	3	3	1	94.855 1.0460 3 5 1 1
77.17	1.2351	2	4	2	0	106.595 0.9607 2 4 4 0
86.235	1.1270	2	4	2	2	114.005 0.9184 2 5 3 1
92.865	1.0631	2	5	1	1	127.415 0.8592 1 6 2 0
104.265	0.9757	1	4	4	0	136.765 0.8286 1 5 3 3
111.15	0.9338	2	5	3	1	
114.005	0.9184	2	6	0	0	
123.765	0.8734	1	6	2	0	
132.31	0.8422	1	5	3	3	
135.355	0.8327	1	6	2	2	

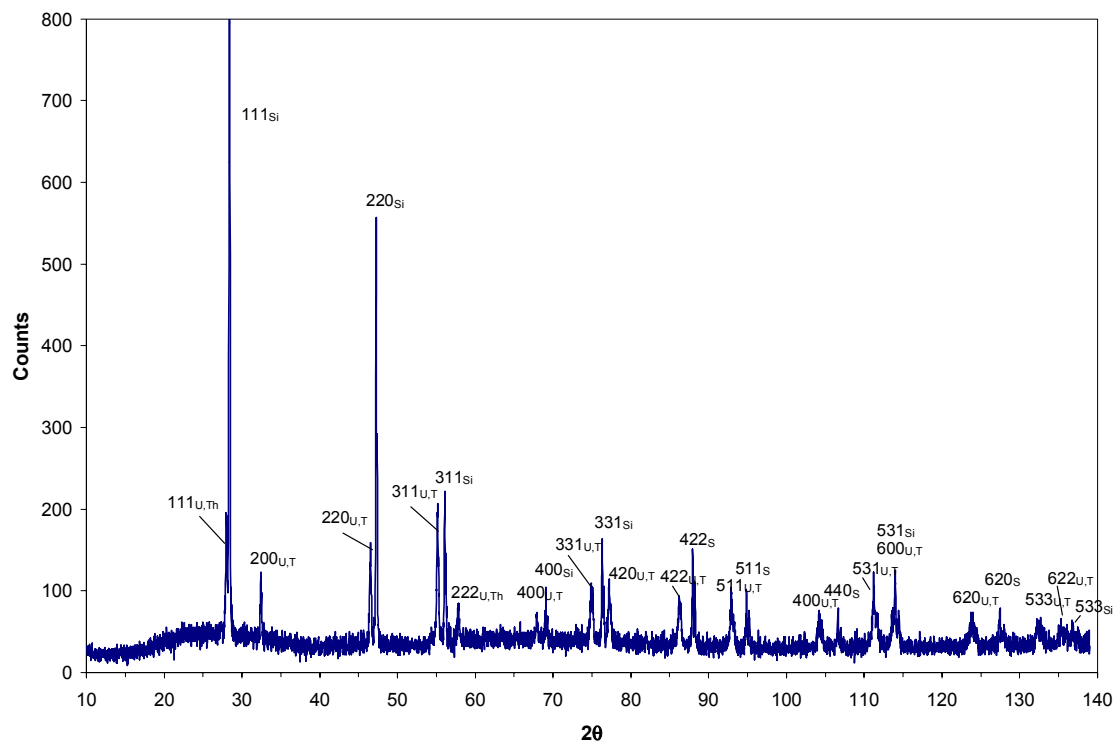


Figure B-9. XRD pattern for 425°C isotherm of co-milled 50.0% UO_2 fragments

Anode: Cu

$\lambda_{\alpha 1}, \lambda_{\alpha 2}$: 1.54056, 1.54439

Generator Voltage: 40V

Tube Current: 20

Scan Step Size: 0.020°

Scan Step Time: 0.25 sec

Table B-10. XRD peak intensities for 425°C isotherm of co-milled 50.0% UO_2 fragments

2θ	d	Int	h	k	l
132.295	0.8422	0	5	3	3
135.195	0.8332	0	6	2	2
(Si)					
28.405	3.1395	100	1	1	1
47.25	1.9221	28	2	2	0
56.07	1.6389	8	3	1	1
69.085	1.3585	2	4	0	0
76.325	1.2466	4	3	3	1
87.96	1.1093	4	4	2	2
94.87	1.0459	2	5	1	1
106.635	0.9605	1	4	4	0
113.975	0.9186	2	5	3	1
127.415	0.8592	1	6	2	0
136.79	0.8285	0	5	3	3
28.045	3.1790	13	1	1	1
32.43	2.7585	5	2	0	0
46.515	1.9507	5	2	2	0
55.165	1.6636	8	3	1	1
57.81	1.5936	2	2	2	2
67.87	1.3798	1	4	0	0
74.87	1.2672	2	3	3	1
77.18	1.2349	2	4	2	0
86.22	1.1271	2	4	2	2
92.885	1.0629	2	5	1	1
104.145	0.9765	1	4	4	0
111.2	0.9335	2	5	3	1
113.615	0.9205	1	6	0	0
123.835	0.8731	1	6	2	0

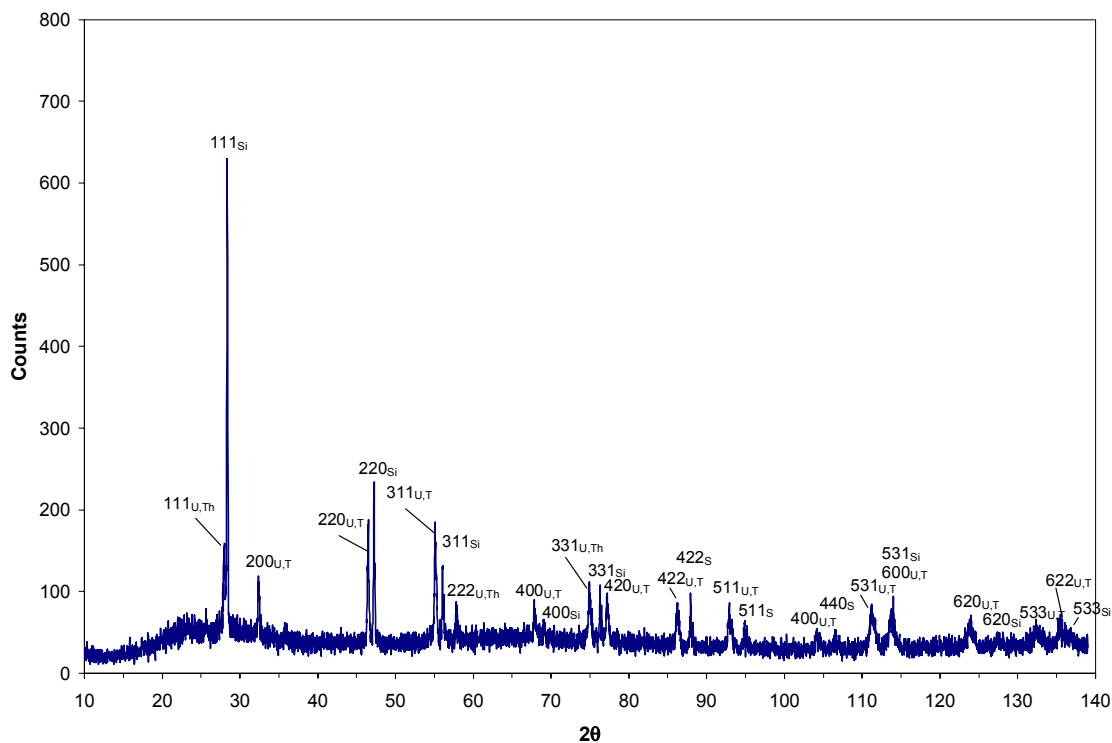


Figure B-10. XRD pattern for 450°C isotherm of co-milled 50.0% UO_2 fragments

Anode: Cu

$\lambda_{\alpha 1}, \lambda_{\alpha 2}$: 1.54056, 1.54439

Generator Voltage: 40V

Tube Current: 20

Scan Step Size: 0.020°

Scan Step Time: 0.25 sec

Table B-11. XRD peak intensities for 450°C isotherm of co-milled 50.0% UO_2 fragments

2θ	d	Int	h	k	l
27.965	3.1879	18	1	1	1
32.39	2.7618	10	2	0	0
46.49	1.9517	13	2	2	0
55.105	1.6652	12	3	1	1
57.765	1.5947	3	2	2	2
67.815	1.3808	3	4	0	0
74.885	1.2670	4	3	3	1
77.18	1.2349	3	4	2	0
86.2	1.1273	3	4	2	2
92.91	1.0627	3	5	1	1
104.16	0.9764	1	4	4	0
111.205	0.9335	2	5	3	1
113.985	0.9185	3	6	0	0
123.725	0.8735	1	6	2	0
132.14	0.8427	1	5	3	3
135.355	0.8327	1	6	2	2
(Si)					
28.37	3.1433	100	1	1	1
47.225	1.9231	21	2	2	0
56.205	1.6352	5	3	1	1
59.13	1.3577	1	4	0	0
76.3	1.2470	4	3	3	1
87.95	1.1094	4	4	2	2
94.875	1.0458	2	5	1	1
106.76	0.9597	0	4	4	0
113.985	0.9185	3	5	3	1
127.405	0.8592	1	6	2	0
			5	3	3

APPENDIX C
SECONDARY ELECTRON IMAGES OF UNIRRADIATED PELLETS

(Microscopy by James Jerden: ANL-E)

Figure C-1. Unpolished $U_{0.05}Th_{0.95}O_{2+x}$ pellet surface. Scale bar is 21 microns. Grain size generally ranges from ~4 to ~20 microns. White “dots” on surface are dust particles introduced during SEM sample prep. [PD020222-2]

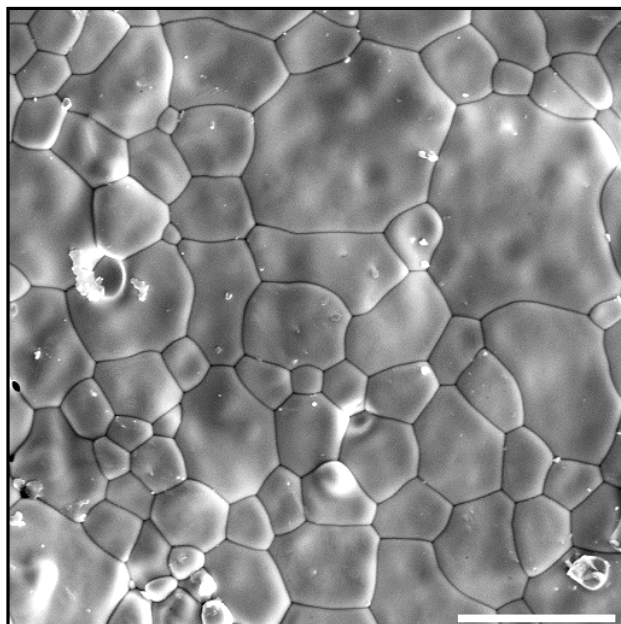


Figure C-2. Unpolished $U_{0.05}Th_{0.95}O_{2+x}$ pellet surface. Scale bar is 20 microns. Grain size generally ranges from ~4 to ~20 microns. White “dots” on surface are dust particles introduced during SEM sample prep. [PD020222-2]

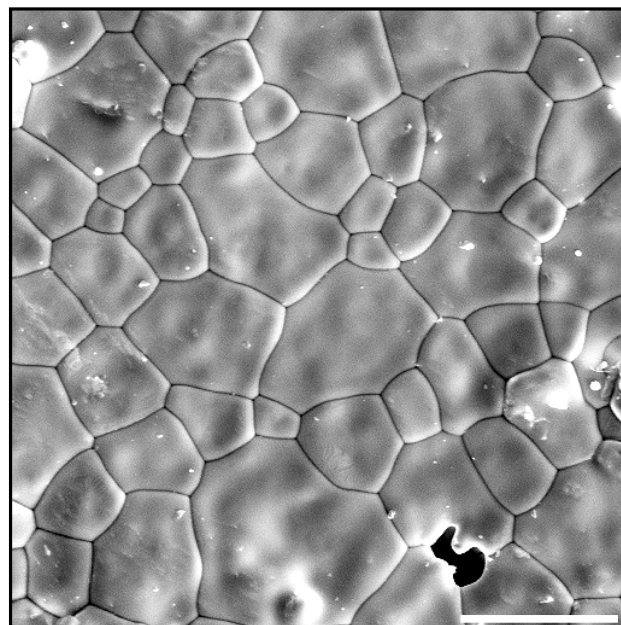
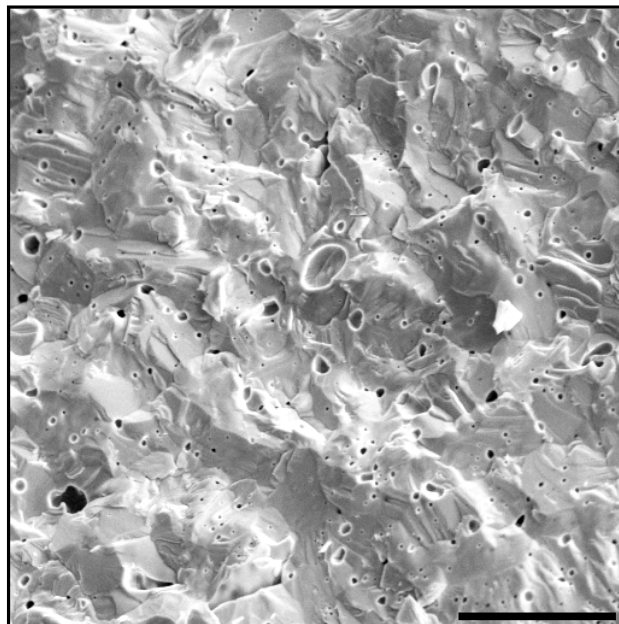


Figure C-3. Broken surface of $U_{0.2}Th_{0.8}O_{2+x}$ pellet. Splitting was accomplished by a single blow within a heavy iron mortar-pestle. Note curious “gas bubble” looking features – these are pervasive on broken surfaces of this pellet. The unbroken pellet surface of this sample looks similar to Figures 42–53. [20BL0202-4]

Scale bar is 27 microns



REFERENCES

- Abd90 A.S. Abdel-Halim, "Physico-chemical characteristics of uranium oxide microspheres produced by internal gelation," *Isotopenpraxis*, **26**, 11 (1990) 524-529.
- And54 J.S. Anderson, D.N. Edgington, L.E.J. Roberts, and E. Wait, "The oxides of uranium. Part IV. The system $\text{UO}_2\text{-ThO}_2\text{-O}$," *Journal of the Chemical Society* (1954) 3324-3331.
- And76 K. Ando, Y. Oishi, and Y. Hidaka, "Self-diffusion of oxygen in single crystal thorium oxide," *Journal of Chemical Physics*, **65**, 7 (1976) 2751-2755.
- And79 K. Ando, and Y. Oishi, "Oxygen self-diffusion and conduction mechanism of thoria," *Journal of Nuclear Science and Technology*, **16**, 3 (1979) 214-220.
- And83 K. Ando, and Y. Oishi, "Diffusion characteristics of actinide oxides – review article," *Journal of Nuclear Science and Technology*, **20**, 12 (1983) 973-982.
- And84 K. Ando, Y. Oishi, T. Tsuji, and Y. Hidaka, "Grain-boundary depressed diffusion of oxygen ions in ThO_2 ," *Journal of Nuclear Materials*, **120** (1984) 99-101.
- And85 K. Ando, Y. Ikeda, S. Morita, R. Watanabe, K. Shiba, and M. Handa, "Preferential vaporization of uranium oxide in the polycrystalline thoria-urania solid solution," *Journal of Nuclear Materials*, **136** (1985) 186-191.
- Ant97 S. Anthonyamy, K. Nagarajan, and P.R. Vasudeva Rao, "Studies on the oxygen potentials of $(\text{U}_y\text{Th}_{1-y})\text{O}_{2+x}$ solid solutions," *Journal of Nuclear Materials*, **247** (1997) 273-276.
- Ant00 S. Anthonyamy, K. Joseph, T. Gnanasekaran, and P.R. Vasudeva Rao, "Studies on the kinetics of oxidation of urania-thoria solid solutions in air," *Journal of Nuclear Materials*, **280** (2000) 25-32.
- Ari00 T. Arima, K. Kitano, K. Takemura, and H. Furuya, "Chemical diffusion of oxygen in thoria-urania solid solution," *Thermochimica Acta*, **344** (2000) 37-45.
- Aro60 S. Aronson, and J.C. Clayton, "Thermodynamic properties of nonstoichiometric urania-thoria solid solutions," *Journal of Chemical Physics*, **32**, 3 (1960) 749-754.
- Bam80 C.H. Bamford and C.F.H. Tipper (Eds.), Chemical Kinetics. Reactions in the Solid State, New York, Elsevier, (1980) pp. 68-83.
- Ban68 M.J. Bannister, "The storage behavior of uranium dioxide powders – review article," *Journal of Nuclear Materials*, **26** (1968) 174-184.

- Bla58 P.E. Blackburn, J. Weissbart, and E.A. Gulbransen, "Oxidation of uranium dioxide," *Journal of Physical Chemistry*, **62** (1958) 902-908.
- Boa77 D.G. Boase, and T.T. Vandergraaf, "The Canadian spent-fuel storage canister: some material aspects," *Nuclear Technology*, **32** (1977) 60-71.
- Cha98 V. Chandramouli, S. Anthonysamy, P.R. Vasudeva Rao, R. Divakar, and D. Sundararaman, "Microwave synthesis of solid solutions of uranium and thorium – a comparative study," *Journal of Nuclear Materials*, **254** (1998) 55-64.
- Col83 E.A. Colbourn, and W.C. Mackrodt, "The calculated defect structure of thorium," *Journal of Nuclear Materials*, **118** (1983) 50-59.
- Cul78 B.D. Cullity, *Elements of X-ray Diffraction*, 2nd edition, Massachusetts, Addison-Wesley Publishing Co. (1978).
- Dob98 B.V. Dobrov, V.V. Likhanskii, V.D. Ozrin, A.A. Solodov, M.P. Dissane, and H. Manenc, "Kinetics of UO₂ oxidation in steam atmosphere," *Journal of Nuclear Materials*, **255** (1998) 59-66.
- Fre80 R. Freer, "Bibliography self-diffusion and impurity diffusion in oxides," *Journal of Materials Science*, **15** (1980) 803-824.
- Fur68 H. Furuya, "Lattice and grain-boundary diffusion of uranium in ThO₂ and ThO₂-UO₂ solid solution," *Journal of Nuclear Materials*, **26** (1968) 123-128.
- Gab93 A. Gabbard, "Coal combustion: nuclear resource or danger," *Oak Ridge National Laboratory Review*, **26**, 3 & 4, (1993) <http://www.ornl.gov/info/ornlreview/rev26-34/text/colmain.html>. Accessed 10/2003.
- Gal02 A.K. Galwey and M.E. Brown, "Application of the Arrhenius equation to solid state kinetics: can this be justified?" *Thermochimica Acta*, **386** (2002) 91-98.
- Gan86 C. Ganguly, H. Langen, E. Zimmer, E.R. Merz, "Sol-gel microsphere pelletization process for fabrication of high-density ThO₂-2% UO₂ fuel for advanced pressurized heavy water reactors," *Nuclear Technology*, **73** (1986) 84-95.
- Har91 D.C. Harris, *Quantitative Chemical Analysis*, 3rd edition, New York, (1991).
- Haw68 R.J. Hawkins, and C.B. Alcock, "A study of cation diffusion in UO_{2+x} and ThO₂ using α -ray spectrometry," *Journal of Nuclear Materials*, **26** (1968) 112-122.
- Lvo01 B.V. L'vov, "Review. The physical approach to the interpretation of the kinetics and mechanisms of thermal decomposition of solids: the state of the art," *Thermochimica Acta*, **373** (2001) 97-124.
- Mal01 J. Malek, T. Mitsuhashi, and J.M. Criado, "Kinetic analysis of solid-state processes," *Journal of the Materials Research Society*, **16**, 6 (2001) 1862-1871.
- Mat85 T. Matsui, and K. Naito, "Oxygen potentials of UO_{2+x} and (Th_{1-y}U_y)O_{2+x}," *Journal of Nuclear Materials*, **132** (1985) 212-221.

- McE97a R.J. McEachern, "A review of kinetic data on the rate of U_3O_7 formation on UO_2 ," *Journal of Nuclear Materials*, **245** (1997) 238-247.
- McE97b R.J. McEachern, J.W. Choi, M. Kolar, W. Long, P. Taylor, and D.D. Wood, "Determination of the activation energy for the formation of U_3O_7 on UO_2 ," *Journal of Nuclear Materials*, **249**, (1997) 58-69.
- Pop73 S. Popovic, "Unit-cell dimension measurements from pairs of x-ray diffraction lines," *Journal of Applied Crystallography*, **6** (1973) 122-128.
- Pop85 S. Popovic, "Unit-cell parameter measurements of alloys by x-ray diffraction," *Crystal Research and Technology*, **20**, 4 (1985) 552-555.
- Ric92 D.W. Richerson, *Modern Ceramic Engineering*, New York, Marcel Dekker, Inc. (1992).
- Ser01 J.A. Serrano, J.P. Glatz, E.H. Toscano, J. Barrero, and D. Papaioannou, "Influence of low-temperature air oxidation on the dissolution behavior of high burn-up LWR spent-fuel," *Journal of Nuclear Materials*, **294** (2001) 339-343.
- Sho00 D.W. Shoosmith, "Fuel corrosion processes under waste disposal conditions – review," *Journal of Nuclear Materials*, **282** (2000) 1-31.
- Sun96 S. Sunder, and N.H. Miller, "Oxidation of CANDU uranium oxide fuel by air in gamma radiation at 150°C," *Journal of Nuclear Materials*, **231** (1996) 121-131.
- Tay96 P. Taylor, W.H. Hocking, L.H. Johnson, R.J. McEachern, and S. Sunder, "A comparison of $(Th,Pu)O_2$ and UO_2 fuels as waste forms for direct disposal," *Nuclear Technology*, **116** (1996) 222-230.
- Tay98 P. Taylor, R.J. McEachern, D.C. Doern, and D.D. Wood, "The influence of specimen roughness on the rate of formation of U_3O_8 on UO_2 in air at 250°C," *Journal of Nuclear Materials*, **256** (1998) 213-217.
- Tsu98 T. Tsuji, M. Iwashita, T. Yamashita, and K. Ohuchi, "Effect of cations on lattice constants of $(M_yU_{1-y})O_{2.00}$ (M=Pu, Th, La) at low doped cation concentrations," *Journal of Alloys and Compounds*, **271-273** (1998) 391-394.
- Uga82 M. Ugajin, "Oxygen potentials of $(Th,U)O_{2+x}$ solid solutions," *Journal of Nuclear Materials*, **110** (1982) 140-146.
- Vya99 S. Vyazovkin and C.A. Wight, "Model-free and model-fitting approaches to kinetic analysis of isothermal and nonisothermal data," *Thermochimica Acta*, **340/341** (1999) 53-
- Whi81 G.D. White, L.A. Bray, and P.E. Hart, "Optimization of thorium oxalate precipitation conditions relative to derived oxide sinterability," *Journal of Nuclear Materials*, **96** (1981) 305-313.

- Wil87 B.T.M. Willis, "Crystallographic studies of anion-excess uranium oxides," *Journal of Chemical Society, Faraday Transactions 2*, **83** (1987) 1073-1081.
- Win03 M. Winter, "Webelements periodic table (professional edition)," *University of Sheffield and WebElements Ltd, UK*, (2003) www.webelements.com. Accessed 10/2003.

BIOGRAPHICAL SKETCH

Lisa Argo was born in Gainesville, Florida where she attended the University of Florida. While an undergraduate student, the author was active in the American Ceramics Society student branch as Correspondence Secretary and the 1999 Engineering Fair Planning Committee as Food Coordinator. After graduating with her Bachelor of Science degree in Materials Science and Engineering in 1999, she worked as an Application Engineer at Elan Technology in Midway, Georgia. The following year, the author married and returned to Gainesville, Florida where she worked as Research Associate for James Tulenko in the UF Department of Nuclear and Radiological Engineering and co-advised by Dr. Ronald Baney in the Department of Materials Science and Engineering. Four months later, the author enrolled in the University of Florida towards completion of a Master of Science in Materials Science and Engineering under Dr. Ronald Baney.